Global characteristics of extreme precipitation and variation of climate types from Köppen-Geiger classification using different datasets

A Thesis Submitted to the College of
Graduate and Postdoctoral Studies
In Partial Fulfillment of the Requirements
For the Degree of Master of Science
In the Department of Civil, Geological and
Environmental Engineering
University of Saskatchewan
Saskatoon

By

Salma Hobbi

Permission to Use

In presenting this thesis in partial fulfillment of the requirements for a Postgraduate degree from the University of Saskatchewan, I agree that the Libraries of this University may make it freely available for inspection. I further agree that permission for copying of this thesis in any manner, in whole or in part, for scholarly purposes may be granted by Dr. Simon Michael Papalexiou who supervised my thesis work or, in their absence, by the Head of the Department or the Dean of the College in which my thesis work was done. It is understood that any copying or publication or use of this thesis or parts thereof for financial gain shall not be allowed without my written permission. It is also understood that due recognition shall be given to me and to the University of Saskatchewan in any scholarly use which may be made of any material in my thesis.

Requests for permission to copy or to make other uses of materials in this thesis/dissertation in whole or part should be addressed to:

Head of the Department of Civil, Geological and Environmental Engineering
University of Saskatchewan
57 Campus Drive
Saskatoon, Saskatchewan S7N 5A9
Canada

OR

Dean
College of Graduate and Postdoctoral Studies
University of Saskatchewan
116 Thorvaldson Building, 110 Science Place
Saskatoon, Saskatchewan S7N 5C9
Canada

Abstract

Climate change is contributing to extreme climate events such as prolonged heat waves, hurricanes, and flooding. Climate classification schemes have become critical tools in investigating these events. One of the most widely used schemes is the Köppen-Geiger (KG) classification, which groups the world's climate types using multiple variables based on precipitation and temperature data. Studies that apply the KG classification have a variety of purposes, including to present the geographical distribution of climate types, to measure shifts among climate types, to study changes in extreme events at regional scales, and to present future projections of climate types. However, several aspects of KG classification have not been thoroughly investigated in the literature: First, few studies have explored the differences among climate types at the global scale derived from multiple sources of precipitation and temperature data; second, little research has looked at changes in extreme precipitation in the KG climate classification at a global scale. This research work points out discrepancies in global climate types by analysing climate maps derived from different globally gridded datasets of precipitation and temperature from 1980 to 2017. Similarity and uncertainty among KG maps at the global and zonal scales are presented. By reducing uncertainty in maps, the research presents robust representations of KG climate types in a new map. This map was applied to assign the climate types of daily station rainfall records (1964 to 2013) to measure changes in extreme precipitation in the KG climate classification. For stations associated with different KG climate types, an analysis was carried out on the annual maxima precipitation time series to measure the trend and heaviness of the tail using the Mann-Kendall test and extreme value theory, respectively. Results from this thesis are as follows: (1) there was large uncertainty in the KG climate classification in the Middle East, northern Russia, eastern, and central Africa; (2) the highest and lowest similarity among the KG maps was observed in the North and South Temperate zones; (3) WFDEI is likely the most reliable dataset to determine KG climate types; (4) of all station records, those associated with Af, Am, Aw, and Cwa climate type showed larger variation in the magnitude of extreme precipitation trends; (5) a significant increasing trend was found in 9.7% of stations in the eastern USA, Asia, and northern Europe, while a significant decreasing trend was observed in only 2% of stations in eastern Australia and central USA; (6) a decreasing

extreme precipitation trend was seen only over the majority of stations associated with BSh, Csa, Csb, and Dsb, whereas an increasing trend was observed in the remaining climate types; and (7) large heavy-tailed extremes were observed in Dfd, ET, and Am, while only light-tailed extremes were observed in Cfc. These results will be useful for scientists studying KG climate classification and the relationship between extreme precipitation changes and climate types.

Acknowledgments

First and foremost, I would like to express my deepest gratitude and thanks to my supervisor, Professor Simon Michael Papalexiou for his continuous motivation and support during the whole study and research period. Second, I would like to thank my advisory committee members Professors Martyn Clark, Christopher Hawkes, for their critical guidance and valuable advice.

I would like to thank Dr. Chandra Rupa Rajulapati for her valuable advice and guidance in my research work. I should also thank the staff at Global Institute at Water Security (GIWS) for providing great environment to do research work.

I also highly appreciate the financial support from the University of Saskatchewan and Global Water Futures program (GWF).

Finally, I would like to give my deepest thanks to my parents and my brother for their love and support.

Dedication

My beloved parents

Forouz Peiravian and Mohammad Hossein Hobbi

And my dear brother

Mohammad Hobbi

Table of contents

Permission to Use i
Abstract ii
Acknowledgments iv
Dedication v
Table of contents vi
List of figures viii
List of tables ix
1. Chapter 1: Introduction 1
1.1 Research Motivation 1
1.2 Research Objectives 2
1.3 Research Contributions 2
1.4 Thesis organizations 4
2. Chapter 2: Discrepancies in Köppen-Geiger Climate Classification Using Ten Global Gridded Products 5
Abstract 5
2.1 Introduction 6
2.2 Data 9
2.3 Köppen-Geiger climate classification 13
2.4 Results 16
2.4.1 Overview 16
2.4.2 Detailed Comparison of the KG maps 17
2.4.3 Merging the different KG maps 26
2.5 Summary and Conclusions 29
2.6 Supplementary material 31
2.7 Annex 34
3. Chapter 3: Extreme precipitation changes in the Köppen-Geiger climate classification 49
Abstract 49
3.1 Introduction 50
3.2 Data 54
3.3 Köppen-Geiger climate classification 55
3.4 Methodology 57
3.4.1 Trend analysis methods 58

3.4.2 Sen's slope estimator 58
3.4.3 Mann-Kendall test 58
3.4.4 Extreme value theory 59
3.5 Results and discussion 61
3.5.1 Extreme precipitation trends 61
3.5.2 Heaviness of tail 63
3.6 Summary and Conclusions 64
4. Chapter 4: Summary and conclusion 67
5. Chapter 5: Recommendations for future work 70
6. Appendix 71
Package development 71
Acquire data: Global Historical Climate Network Daily (GHCN-D) 72
COPYRIGHT PERMISSION 74
7. Chapter 7: List of References 75

List of figures

Figure 2.1 Köppen-Geiger world maps at 0.5° resolution for the 1980-2017 period, derived by using different precipitation and temperature products: (a) UDEL, (b) CRU, (c) CPC-CRU, (d) GPCC-CRU, (e) NCEP/CFSR, (f) JRA-55, (g) ERA5, (h) MERRA2, (i) MS-CRU, (j)WFDEI15
Figure 2.2. Percentage of grid points showing similar climate type in each pair of KG world maps (from 1980 to 2017) derived from ten different gridded products. 17
Figure 2.3. Percentage of grid points having the same climate types in pairs of KG maps (from 1980 to 2017) in geographical zones. In the left panel, the upper triangular matrix refers to the polar zone, and the lower triangular matrix to the north temperate zone. In the right panel, the upper triangular matrix refers to the tropics, and the lower triangular matrix to the south temperate zone. 19
Figure 2.4. Average similarity (%) of: (a) a KG map with the rest of the maps in geographical zones (each box plot is constructed by 4 values; rows in Table 3); (b) KG maps per zone (each box plot is constructed by ten values; columns in Table 3). The blue crosses show the average similarity in each boxplot, while the red crosses show the outliers. The whiskers denote maximum and minimum similarity. 20
Figure 2.5. Percentage of land area covered by Köppen-Geiger climate subtypes. Panels (a-e) show subtypes of climate types A, B, C, D and E, and panel (f) shows total percentage of land area covered by the major climate types. 21
Figure 2.6. Number of distinct Köppen-Geiger (a) major climate types, (b) climate subtypes in grid points among the ten KG maps derived for the 1980-2017 period. 25
Figure 2.7. Master KG maps for the 1980-2017 period constructed by (a) depicting the most frequent climate subtype among all KG maps, and (b) merging temperature and precipitation data from all gridded products into a single dataset and using it to assess the climate subtypes. 28
Figure 2.8. Similarity of individual KG maps shown in Figure 2.1 with the two master KG maps shown in . The dashed line shows the average similarity (88%) between all individual maps and the master maps 1 and 2. 29
Figure 2.9. Köppen-Geiger (KG) world maps at 0.5° resolution for 1980–2017, developed by using precipitation (P) and temperature (T) products: (a) UDEL, (b) CRU, (c) CPC-CRU, (d) GPCC-CRU, (e) NCEP/CFSR, (f) JRA-55, (g) ERA5, (h) MERRA2, (i) MS-CRU, (j) WFDEI. 39
Figure 2.10. *T*cold maps derived from the following datasets: (a) CRU, (b) NCEP/CFSR, (c) JRA-55, (d) ERA5, (e) MERRA2. Each map shows regions with $T\text{cold} < -38$ ℃ depicting climate subtypes with "d" as the third letter. *T*cold denotes the air temperature (°C) of the coldest month. Borders of Yakutia (Sakha) are depicted in north-eastern Russia. The study period is from 1980 to 2017. 41
Figure 2.11. *T*hot maps derived from the following datasets: (a) CRU, (b) NCEP/CFSR, (c) JRA-55, (d) ERA5, (e) MERRA2. Each map shows spatial patterns of *T*hot within following ranges: [0, 10, 18, 22] or ($T\text{hot} \leq 0, T\text{hot} \geq 0, T\text{hot} \leq 10, T\text{hot} \geq 10, T\text{hot} \geq 22$). *T*hot denotes the air temperature of the warmest month (°C). The borders of Yakutia (Sakha) are depicted in north-eastern Russia. The study period is from 1980 to 2017. 44
Figure 2.12. *P*wdry maps derived from following datasets: (a) CRU, (b) NCEP/CFSR, (c) JRA-55, (d) ERA5, (e) MERRA2. Each map show regions covering $P\text{wdry} < P\text{swet}/10$, meeting the precipitation criteria for presenting the Dw climate type. *P*wdry/*P*swetdenotes the precipitation of the driest/wettest month in winter/summer (mm/month), respectively. The

borders of Yakutia (Sakha) is depicted in north-eastern Russia. The study period is from 1980 to 2017. 46
Figure 2.13. *P*sdry maps derived from following datasets: (a) CRU, (b) NCEP/CFSR, (c) JRA-55, (d) ERA5, (e) MERRA2. Each map show regions covering *P*sdry < 40 & *P*sdry < *P*wwet/3, meeting the precipitation criteria for presenting the Ds climate type. *P*sdry/*P*wwetdenotes the precipitation of the driest/wettest month in summer/winter (mm/month), respectively. The borders of Yakutia (Sakha) are depicted in north-eastern Russia. The study period is from 1980 to 2017. 48
Figure 2.14. Topographic map of terrestrial regions at 0.5° resolution. 48
Figure 2.15. Average number of precipitation stations per month from GPCC dataset for 1980–2017. 48
Figure 3.1. KG climate classification: (a) Robust KG classification map presented in Section 2.4.3, (b) the available stations and their climate type from 1964 to 2013. 57
Figure 3.2. Trends of AMP time series for station time series associated with each climate sub-type from 1964 to 2013: (a) variation of trends, (b) percentage of time series showing positive/negative trends and significant positive/negative trends. 62
Figure 3.3. Location of Sen's slope estimator trend analyses for 8582 station AMP time series from 1964 to 2013. Light blue open dots indicate non-significant increasing trends, and light red open dots mark non-significant decreasing trends. Dark blue and red-filled dots indicate statistically significant trends, as determined by Mann-Kendall test at 5% level of significance. 63
Figure 3.4. Variation of shape parameter (γ) of the fitted $\mathcal{GEV}$ distribution of AMP time series for stations associated with each major climate type (left panel) and climate subtype (right panel) from 1964 to 2013. $\gamma > 0$ indicates heavy-tailed extremes and $\gamma < 0$ light-tailed extremes. 64
Figure 6.1. Graphical User Interface of CoSMoS-MATLAB package. 72

List of tables

Table 2.1. Basic information on the global datasets of precipitation and near-surface temperature used to derive Köppen-Geiger maps (where T: air temperature, P: precipitation, R: reanalysis datasets, and G: gauged-based datasets, S: satellite-based datasets). 11
Table 2.2. Main characteristics of the KG major climate groups, including the defining criteria. 14
Table 2.3. Average similarity (%) of a KG map with the rest of the maps in geographical zones; green and red colours highlight the maximum and minimum, respectively, in each zone... 19
Table 2.4. Variation in land coverage of major climate type in KG maps;green and red colours highlight the maximum and minimum, respectively. 22
Table 2.5. Percentage of land represented by major KG climate types in the master and merged KG maps. 29
Table 3.1. Main characteristics of the Köppen-Geiger climate classification 56

1. Chapter 1: Introduction

1.1 Research Motivation

The world's climate is characterized by patterns and large-scale changes in atmospheric and oceanic circulation, in the global distribution of solar radiation, and in the frequency and intensity of extreme precipitation. To determine the world's regions most likely to be impacted by climate change, researchers study these patterns and changes (Donat et al., 2016a; Karl, 2003; Trenberth et al., 2007). To analyse precipitation and temperature trends, climate variation, and the characteristics of extreme events, researchers use global precipitation and temperature datasets (Gleckler et al., 2008; Kidston et al., 2010; Kravtsov et al., 2014; MacKellar et al., 2007; New et al., 2000). Several scientists have investigated changes in extreme precipitation and temperature by analysing the trends of annual maximum daily indices, using station-based and climate model outputs (e.g., Papalexiou & Montanari, 2019; Westra et al., 2013). Precipitation and temperature data have also been used to determine a region's climate based on the Köppen-Geiger (KG) climate classification. Accounting for monthly precipitation and near-surface temperature, this classification system places each region's climate on a world map (Köppen & Geiger, 1928). Since it was published in 1900, this classification has been updated and modified using different gridded and station-based precipitation and temperature datasets (e.g., Peel et al., 2007). Researchers have applied the KG classification in several ways: to depict the geographical distribution of climate types, to detect changes in the climate, and to project future climate types.

Despite the large number of climate-related studies, several gaps in the literature remain. First, although numerous studies have used KG classification based on individual global products, few have investigated how the climate varies when different precipitation and temperature products are used. Second, several studies have examined extreme precipitation trends at a global and regional scale, but little is known about how extreme precipitation trends vary among KG climate types. Studies on changes in extreme precipitation among KG climate types have used different precipitation and temperature data, resulting in dissimilar evaluations of KG climate types. In other words, in these studies variations in extreme precipitation and their interpretation in connection with KG climate

types are only valid for the particular KG climate types under study. These variations therefore cannot be connected with other studies that use different sources of precipitation and temperature to develop KG maps.

Chapter 2 discusses discrepancies in KG classification world maps derived from different global gridded products of precipitation and temperature. The result of this research is the development of two robust KG maps from 1980 to 2017. The first robust KG map was created by combining data from different sources of precipitation and temperature, and the second map was developed through combining the most frequent climate types observed in all KG world maps. Chapter 3 uses the second map to assign climate type to daily rainfall records from station data. This chapter analyses changes in the extreme precipitation trends for each of the KG climate types from 1964 to 2013.

1.2 Research Objectives

The general goals of this research work is to study discrepancies in KG maps derived from different precipitation and temperature datasets, to create a robust KG world map showing reliable climate types, to analyse changes in extreme precipitation trends among KG climate types, to explore climate types having the most frequent and largest magnitude of extreme precipitation. The specific objectives of this research are as follows: to develop KG classification maps using global datasets of precipitation and temperature from different sources, to assess the uncertainty in evaluating KG climate types, to create a robust KG world map by reducing uncertainty among other KG maps, to offer the first global analysis and comparison of degrees of change in extreme precipitation for different climate types, to provide new insights into differences in precipitation trends in areas with the same and distinct climate types across the globe.

1.3 Research Contributions

This study makes an important contribution to the literature because it is the first to compare KG climate maps derived from 10 different precipitation and temperature datasets. Overall, the research shows which datasets are more reliable in presenting KG climate types and which regions show more uncertainty when KG climate types derived from these datasets are mapped. As well, this research offers the first global analysis and comparison of

degrees of change in extreme precipitation by looking at climate types. Additional contributions are listed below.

1) There is high uncertainty among KG climate types based on precipitation and temperature data in the Middle East, northeastern Russia, central Africa, and western America when these regions are classified according to KG climate types.
2) Reanalysis temperature products show warmer minimum annual temperature compared to gauge-based and multi-source products.
3) Among ten products tested, WFDEI is the most reliable product from which to develop KG maps at global and zonal scales.
4) Two robust KG maps from 1980 to 2017 are presented by combining ten different sources of precipitation and temperature data. These reliable maps reduce the uncertainty in evaluating KG climate types.
5) Variation of extreme precipitation trends among the robust KG climate types were measured at the global scale.
6) Heavy-tailed extremes were over 1964 to 2013 were shown.
7) Climate types experienced most frequent and largest magnitudes of extreme precipitation were determined.

This research has several applications. First, it will apply to scientists seeking to understand the variations in developing KG maps using different data sources and the effects of climate type on extreme precipitation patterns. Second, it will help researchers to better evaluate the historical (past) climate, also,measure future climate shifts, as well as relationship between historical vs future climate. Third, it — particularly the link between climate type and extreme events such as floods — will help engineers to better design infrastructure and climate change mitigation plans. Fourth, it will provide policymakers developing policies to mitigate and adapt to climate change with a more robust presentation of climate types than is currently available. Fifth, it will help the providers of precipitation and temperature data to improve their estimations in regions showing more uncertainty in the presentation of KG climate types

1.4 Thesis organizations

This thesis is organized into five chapters. Chapter 1 includes a brief introduction, research motivation, and research objectives along with major contributions of this MSc thesis. Chapter 2, which has been submitted to a peer review journal, shows results from presenting discrepancies in KG maps using different products. Chapter 3 reveals the results of changes in extreme precipitation among KG climate types. This chapter will be submitted to a peer reviewed journal. Chapters 4 and 5 summarize the thesis and provide conclusions, and recommendations for future works. The thesis concludes with an appendix, which is dedicated to the development of the CoSMoS package (published in October 2019) and indicates copyright permission.

2. Chapter 2: Discrepancies in Köppen-Geiger Climate Classification Using Ten Global Gridded Products

In Chapter 2, Köppen-Geiger Climate Classification maps are derived from ten different precipitation and temperature datasets at 0.5° resolution for the time period 1980 to 2017. The similarity between maps and the uncertainty in determining climate types are presented. At the end, robust climate maps were presented by combining precipitation and temperature from all data sources. This chapter has been submitted to "Journal of Climate" and it is under review. The authors of this chapter are Salma Hobbi, Simon Michael Papalexiou, Chandra Rupa Rajulapati, Martyn Clark, and Guoqiang Tang. Salma Hobbi contributions to this paper are as follows: reviewing the relevant literature, gathering and analyzing the data, analyzing the results, and writing the manuscript under the supervision of Dr. Simon Michael Papalexiou. The manuscript was reviewed and revised by Dr. Simon Micheal Papalexiou before submission to the journal for publication.

Abstract

Köppen-Geiger (KG) climate classification has been widely used to determine the climate at global and regional scales using precipitation and temperature data. KG maps are typically developed using a single product; however, uncertainties in KG climate types resulting from different precipitation and temperature datasets have not been explored in detail. Here, we assess how ten different global datasets affect the KG classification during the 1980–2017 period. Using a pairwise comparison at global and zonal scales, we quantified the similarity among the ten KG maps. Gauge-based and reanalysis KG maps have a relatively low similarity, while the highest and lowest similarity is observed for the North and South Temperate zones, respectively. Notably, 17.9% of grids points among the ten maps show variations even in the major KG climate types, while 37.2% of grids points are described by more than one KG climate subtype. Strong uncertainty is observed in regions of south Asia, central and south Africa, western America, and northeastern Australia. We combined

information from all datasets and created two KG master maps at the 0.5° resolution. These master maps are more robust than the individual ones showing coherent spatial patterns. Our work reveals the large uncertainty in climate classification and offers two robust KG maps that may help to better evaluate historical climate and quantify future climate shifts.

2.1 Introduction

Climate determines the distribution of major ecosystems (including forests, deserts, tundra, etc.) on earth. Regional climate is mainly affected by the global distribution of solar radiation and the large-scale atmospheric and oceanic circulation patterns. This leads to many different climate types and the need to classify them. Climate classifications identifies regions that have similar climate characteristics. These classifications help to evaluate regional climate changes or shifts (Domroes, 2003; Fraedrich et al., 2001; Gao & Giorgi, 2008; Rohli et al., 2015), effects of climate change on agriculture and vegetation (Cramer & Leemans, 1993; Maracchi et al., 2005; Taylor & Philp, 2016), determine suitable local or regional crops (Araya et al., 2010; Meybeck et al., 2012), develop agro-climatic zones (Bouma, 2005), and improve infrastructure design (e.g., dams, roads, etc.) (Hossain et al., 2012; Taylor & Philp, 2015). Several climate classifications exist representing regional characteristics such as (1) precipitation and temperature, (2) biome, and (3) geographical location, altitude, and humidity (Holdridge, 1947; Köppen & Geiger, 1928; Olson et al., 2001; Thornthwaite, 1948). However, the most popular climate classification is the Köppen-Geiger (KG). Based on empirical relationships between vegetation and climate, this classification uses simple calculations of temperature and precipitation data (Köppen and Geiger, 1928). Over the last decades the interest on climate classification has been intensified. The main reason is the many readily available gridded precipitation and temperature products that were used to update and explore the KG classification all over the globe. Yet literature lacks information on how the KG classification varies if based on different global products.

In 1900, Wladimir Köppen established the first quantitative climate classification and produced the first climate map. A revised climate classification map was published in 1918 (Köppen, 1918). In 1923, he used the classification to investigate the boundaries of climate

in the globe (Köppen, 1923). Köppen and Geiger presented the first world map of climate classification in 1928 (Köppen and Geiger, 1928) creating thus the well-known Köppen-Geiger (KG) classification. The classification was refined by Köppen (1936) and improved by Geiger (1954). A modification was proposed by Köppen and Trewartha (Trewartha & Horn, 1980; Trewartha, 1968) as well as by Peel et al. (2007) who amended some criteria.

The global KG maps have been updated many times over the last decades and gained popularity not only for linking climate and vegetation (Bailey, 2009) but also for their simplicity (Wilcock, 1968). In the early 1990s, used station data (for the first time) from northern hemisphere to identify the KG climate types. Some studies investigated climate changes by creating KG maps from the outputs of climate models and compared them with the Köppen's 1923 map and maps created from gridded products (Gnanadesikan & Stouffer, 2006; Kalvová et al., 2003; Kleidon et al., 2000; Lohmann et al., 1993; Wang & Overland, 2004). Kottek et al. (2006) adopted gridded data to update the world KG-classification map between 1951 and 2000, while Chen & Chen (2013) and Peel et al. (2007) adopted station-based datasets with more than 30 years of data for each record. A recent fine resolution of KG classification was derived by using model ensemble datasets and observations by Beck et al. (2018). Here we apply the KG classification, as modified by Peel et al.(2007), by using many global temperature and precipitation products in order to quantify the uncertainty in climate types.

Global precipitation and temperature datasets have been widely used for different purposes including ecological and hydrological modelling, validating climate models, analyzing climate variation, synthesizing extreme events characteristics, and calibrating forecast models (Gleckler et al., 2008; Kidston et al., 2010; Kravtsov et al., 2014; MacKellar et al., 2007; New et al., 2000). These datasets were derived from combining different sources (gauge-based observations, radar, satellite, reanalysis, or combinations of them) at various spatial (from 0.5° to 5°) and temporal resolutions (from sub-daily to monthly). Most of the global gridded products provide estimates of both precipitation and temperature at different spatial and temporal resolutions (see e.g., the gauge-based University of Delaware (UDEL); the Japanese 55-year Reanalysis (JRA-55), the Multi-Source Weighted-Ensemble Precipitation (MSWEP), etc.). Other products such as the Global Precipitation Climatology Center (GPCC), the Climate Prediction Center (CPC) unified, and the NCEP/NCAR focus only

on precipitation. Given that these products use raw data from different sources and different processing methods it is anticipated their precipitation or temperature estimates to differ. Indeed, several studies show notable differences (Costa & Foley, 1998; Dore, 2005; Folland et al., 2001; Hawkins et al., 2017; Rajulapati et al., 2020; Sun et al., 2018; Wong et al., 2017). Thus, the climate type identified in a region, since the KG classification uses temperature and precipitation measurements, might differ depending on the dataset used. Literature lacks information on how KG climate types vary given that different global precipitation and temperature products are used.

A main application of the KG climate classification is to identify the geographical distribution of climate types. KG climate maps have been constructed by using gridded (1) station-based data (Chen & Chen, 2013; de Oliveira Aparecido et al., 2020; Kottek et al., 2006; Peel et al., 2007; Rubel & Kottek, 2010; Triantafyllou & Tsonis, 1994), (2) climate models outputs (Fraedrich et al., 2001; Gnanadesikan & Stouffer, 2006; Guetter & Kutzbach, 1990; Kalvová et al., 2003; H.-J. Kim et al., 2008; Lohmann et al., 1993), and (3) ensembles of station-based and climate models data (Beck et al., 2018). A second application aims to detect changes and shifts in KG climate types over time. Climate change and long-term climate variations can affect the regional climate and the distribution of plants, and thus the KG climate types (Elmendorf et al., 2012). Specifically, changes in climate type have been investigated by comparing regions identified by KG climate subtypes (Chen & Chen, 2013; Diaz & Eischeid, 2007; Wang & Overland, 2004). Kim et al (2008) showed that between 1951-1970 and 1981-2000, Northern China experienced shifts to dryer conditions. Fraedrich et al. (2001) showed substantial changes in the modified Köppen climate zones in the late 20th century, and statistically significant shifts over the deserts of southern Africa and the tropics. In east Asia, regional climate changes were investigated by calculating the frequency of occurrence of KG subtypes (Yoshino & Kazuko, 1981).

The KG classification has also been used to show projected KG world maps and future changes in climate types. Yun et al. (2012) investigated the sub-tropical area of the future climate in Korea and showed increase of 21% and 35% based on the Trewartha and KG classifications, respectively. According to Kalvová et al. (2003) and Lohmann et al. (1993) regions with tropical and dry climate types will expand in the future while regions described by the rest of climate types will shrink. Projected global KG maps were derived using

different climate models and methods. Rubel and Kottek (2010) presented the future global KG map (resolution 0.5°) from 2076 to 2100 using temperature and precipitation data from ensemble of global climate model projections provided by Tyndall Centre for Climate Change Research (TYN) (Mitchell et al., 2004) for four IPCC emission scenarios. Beck et al. (2018) used an ensemble of climate projections (32 models; RCP8.5 scenario) from the Coupled Model Intercomparison Project Phase 5 (CIMIP5) (Taylor et al., 2012) to derive a fine resolution (resolution 0.0083°) global KG map for the 2071-2100 period. They depicted the present-day (1980-2016) and future (2071-2100) confidence maps of KG subtypes by calculating the fraction of most common climate subtype and the ensemble size. Although KG climate maps have been updated and used many times, Beck et al. (2018) is one of the few studies that compared the similarity of KG climate subtypes between climate models and observations; yet they did not show the uncertainty among the data products they used.

In this study, we assess how different global datasets affect the evaluation of climate subtypes in the KG classification. We use ten gridded products of precipitation and temperature, including reanalysis, gauge-based and satellite datasets, covering the 1980-2016 period. Our objectives are to (1) develop KG classification maps using many global datasets, (2) assess the uncertainty in evaluating KG climate types, and (3) create a KG world map by combining all datasets.

2.2 Data

In this study, we used monthly near-surface (2-meter) temperature and total precipitation data from gauged-based and reanalysis products, and from products combining various sources of information (e.g., satellites, reanalysis, gauges, etc.). Particularly, we used:

- four gauge-based products (land-based datasets, more detailed in section 2.7): the University of Delaware Air Temperature & Precipitation (UDEL, version 5.01); the Climate Research Unit, University of East Anglia, (CRU TS, version 4.04); the Climate Prediction Center Unified (CPC Unified, version 1); and the Global Precipitation Climatology Centre GPCC (GPCC, version 8);
- four reanalysis products (combination of historical data and current weather models, more detailed in section 2.7): the National Centers for Environmental Prediction

(NCEP)/Climate Forecast System Reanalysis, (NCEP/CFSR, versions 1 and 2); the Japanese 55-year Reanalysis (JRA-55); the 5-th generation of the European Centre for Medium-Range Weather Forecasts (ERA5); and the Modern-Era Retrospective analysis for Research and Applications (MERRA, version 2);

- and two widely used multi-source products (combining data from gauge-based, reanalysis, and satellite-based products, more details in Section 2.7): the Multi-Source Weighted-Ensemble Precipitation (MSWEP) data which combines information from satellites, reanalysis and gauges; and the WFDEI Meteorological Forcing Data (WFDEI) which combines the satellite and reanalysis data.

Table 2.1 summarizes basic information on these datasets such as their temporal and spatial resolution, covering period, variables included, and so forth.

More specifically, UDEL was derived from station data such as the Global Historical Climatology Network (GHCN2) and the Global Surface Summary of Day (GSOD) (Willmott & Matsuura, 1995). CRU TS offers high resolution land-based data (excluding Antarctica) by interpolating monthly climate anomalies from an extensive weather station network (Harris et al., 2014). CPC Unified combines several gauge-based precipitation products by applying optimal interpolation to data sources from the NOAA Climate Prediction Center (Chen et al., 2008). GPCC is formed by spatially interpolating the anomalies from the climatological normal values of precipitation at stations (Rudolf et al., 2010).

Reanalysis datasets are used in this study as they provide a complete overview of climatic conditions through the process of data assimilation during a period of about 30 years and more. Specifically, the NCEP/CFSR is a high resolution reanalysis product which couples ocean, atmospheric, sea ice, and land surface data sources (Saha et al., 2014); JRA-55 is a comprehensive reanalysis climate dataset covering more than half a century by applying the four-dimensional variational analysis (4D-Var) assimilation system (Kobayashi et al., 2015); ERA5 is a reanalysis global dataset including records of land surface, atmosphere, and ocean waves (Hersbach et al., 2020); and MERRA2 is a reanalysis atmospheric product using satellite data generated by NASA's Global Modeling and Assimilation Office (GMAO) (Gelaro et al., 2017). Note that although reanalysis estimates are based on observations and model forecasts, these estimates are not "real" observations (e.g., Bosilovich et al., 2013). In practice, reanalysis precipitation estimates are bias and/or gauge

corrected using different gauge/satellite-based datasets (see supplementary material Table S1, section 2.6).

Finally, the MSWEP dataset is formed by merging various sources including gauge-based datasets (e.g., GHCN-D, GSOD, and others), reanalysis datasets (e.g., JRA-55), and satellite-based datasets (e.g., Tropical Rainfall Measuring Mission (TRMM)) (Beck et al., 2019). WFDEI is created by applying the WATCH Forcing Data methodology and making use of the ERA-Interim reanalysis data (Weedon et al., 2014).

There are more datasets in the literature than those used in this research, yet datasets with resolution close to 0.5° resolution were considered to keep consistency between the datasets. Note that each datasets is regridded to 0.5°, by using the bilinear interpolation method, the few datasets (see Table 2.1) with resolution not equal to 0.5°. Also, to have a common temporal coverage in all datasets, a common period is chosen, that is, from 1980 to 2017 (exception is the GPCC dataset spanning from 1980 to 2016). Then, monthly precipitation and temperature data were extracted from datasets with daily and subdaily temporal coverage. In terms of precipitation, the accumulation of total precipitation data within subdaily intervals (6-hourly) were calculated as the total daily precipitation. Thus, the accumulation of daily total precipitation within a month represents the total monthly precipitation data. In terms of temperature, average daily data were extracted from subdaily temperature data. As a result, the average of daily data within a month represents the average monthly temperature. Finally, the KG climate types were assessed (1) by using the monthly precipitation and temperature data of the CRU, UDEL, MERRA 2, JRA-55, WFDEI, NCEP/CFSR, and ERA5 products, and (2) by coupling the monthly precipitation estimates from the CPC, GPCC, and MSWEP with the monthly CRU TS temperature.

Table 2.1. Basic information on the global datasets of precipitation and near-surface temperature used to derive Köppen-Geiger maps (where T: air temperature, P: precipitation, R: reanalysis datasets, and G: gauged-based datasets, S: satellite-based datasets).

Dataset	Full name and details	Data source	Variable (s)	Resolution	Temporal resolution	Temporal coverage	Reference
UDEL	University of Delaware Air Temperature & Precipitation version 5.01 (https://psl.noaa.gov/data/gridded)	G	T, P	0.5°	Monthly	1900-2017	(Willmott & Matsuura, 1995)

CRU	Climate Research Unit, University of East Anglia version 4.04 (http://www.cru.uea.ac.uk/data)	G	T, P	0.5°	Monthly	1901-2019	(Harris et al., 2014)
CPC Unified (CPC)	Climate Prediction Center (CPC) Unified version 1 (https://www.esrl.noaa.gov/psd/data/gridded/)	G	P	0.5°	Daily	1979- present	(Chen et al., 2008)
GPCC	Global Precipitation Climatology Centre version 8 (http://gpcc.dwd.de/)	G	P	0.5°	Monthly	1891-2016	(Rudolf et al., 2010)
NCEP/ CFSR	National Centers for Environmental Prediction (NCEP) Climate Forecast versions 1 and 2 (http://cfs.ncep.noaa.gov/cfsr/)	R	T, P	0.5°	6-hourly	1979- present	(Saha et al., 2014)
JRA-55	Japanese 55-year Reanalysis (https://jra.kishou.go.jp/JRA-55/)	R	T, P	0.56°	6-hourly	1957- present	(Kobayashi et al., 2015)
ERA5	5th generation of European Centre for Medium-Range Weather Forecasts (ECMWF) (https://cds.climate.copernicus.eu/)	R	T, P	0.5°	Monthly	1979- present	(Hersbach et al., 2020)
MERRA 2	Modern-Era Retrospective analysis for Research and Applications, version 2 (https://gmao.gsfc.nasa.gov/reanalysis/MERRA-2/)	R	T, P	0.5° × 0.667°	Monthly	1980-2019	(Gelaro et al., 2017)
MSWEP (MS)	Multi-Source Weighted-Ensemble Precipitation (MSWEP) version 2.2 (https://gloh2o.org)	S, G, R	P	0.5°	Monthly	1979-present	(Beck et al., 2019)
WFDEI	WATCH Forcing Data methodology applied to ERA-Interim data version 2018 (http://www.eu-watch.org/)	R	T, P	0.5°	Daily	1979-2018	(Weedon et al., 2014)

2.3 Köppen-Geiger climate classification

The Köppen-Geiger (KG) climate classification uses monthly and annual total precipitation and monthly near-surface temperature to identify the climate type of a region. The scheme groups terrestrial climates into five main types: tropical (A), dry (B), temperate (C), snow (D), and polar (E). These major types are refined into subtypes based on precipitation (represented by the second letter, except for the E type) and temperature criteria (third letter). The criteria used in the KG classification were initially defined by Köppen (1936) and modified by Peel et al (2007) . Peel et al. (2007) altered the temperate (C) and cold (D) climate types by replacing the threshold of 3 °C with 0 °C as suggested by Russell (1931). Additionally, they changed the criteria for the (s) and (w) subtypes within the (C) and (D) types considering whether more precipitation falls in summer (w) or in winter (s). The climate types (BS) and (BW) were modified by considering that 70% of precipitation falls in summer and winter, respectively. Here, we use the datasets in Table 2.1 to construct global KG maps following the modification of Peel et al. (2007) similarly to other studies (see e.g., Beck et al., 2018, Kriticos et al., 2012). The detailed criteria that identify a KG climate subtype as summarized in Table 2.2 which used the following variables:

- MAP = mean annual precipitation (mm/year)
- MAT = mean annual temperature (°C)
- T_{cold} = the air temperature of the coldest month (°C)
- T_{hot}= the air temperature of the warmest month (°C)
- T_{mon10} = the number of months with air temperature > 10 °C (no unit)
- P_{dry} = precipitation of the driest month (mm/month)
- P_{sdry} = precipitation of the driest month in summer (mm/month)
- P_{wdry} = precipitation of the driest month in winter (mm/month)
- P_{swet} = precipitation of the wettest month in winter (mm/month)
- $P_{\text{th}} = 2 \times \text{MAT} + 28$ if more than 70% of precipitation falls in summer, otherwise $P_{\text{th}} = 2 \times \text{MAT} + 1$

Table 2.2. Main characteristics of the KG major climate groups, including the defining criteria.

1st	2nd	3rd	Description	Criterion
A			Tropical	Not (B) & $T_{\text{cold}} \geq 18$
	f		Rainforest	$P_{\text{dry}} \geq 60$ mm
	m		Monsoon	Not (Af) & $P_{\text{dry}} \geq 100 - \text{MAP}/25$
	w		Savannah	Not (Af) & $P_{\text{dry}} < 100 - \text{MAP}/25$
B			Arid	$\text{MAP} < 10 \times P_{\text{th}}$
	W		Desert	$\text{MAP} < 5 \times P_{\text{th}}$
	S		Steppe	$\text{MAP} \geq 5 \times P_{\text{th}}$
		h	Hot	$\text{MAT} \geq 18$
		k	Cold	$\text{MAT} < 18$
C			Temperate	Not (B) & $T_{\text{hot}} \geq 10$ & $0 < T_{\text{cold}} < 18$
	s		Dry summer	$P_{\text{sdry}} < 40$ & $P_{\text{sdry}} < P_{\text{wwet}}/25$
	w		Dry winter	$P_{\text{wdry}} < P_{\text{swet}}/10$
	f		Without dry season	Neither (Cs) or (Cw)
		a	Hot summer	$T_{\text{hot}} \geq 22$
		b	Warm summer	Not (a) & $T_{\text{mon10}} \geq 4$
		c	Cold summer	Not (a or b) & $1 \leq T_{\text{mon10}} < 4$
D			Cold	Not (B) & $T_{\text{hot}} \geq 10$ & $T_{\text{cold}} \leq 0$
	s		Dry summer	$P_{\text{sdry}} < 40$ & $P_{\text{sdry}} < P_{\text{wwet}}/3$
	w		Dry winter	$P_{\text{wdry}} < P_{\text{swet}}/10$
	f		Without dry season	Not (Ds) or (Dw)
		a	Hot summer	$T_{\text{hot}} \geq 22$
		b	Warm summer	Not (a) & $T_{\text{mon10}} \geq 4$
		c	Cold summer	Not (a, b, or d)
		d	Very cold winter	Not (a or b) & $T_{\text{cold}} < -38$
E			Polar	Not (B) & $T_{\text{hot}} \leq 10$
	T		Tundra	$T_{\text{hot}} > 0$
	F		Frost	$T_{\text{hot}} \leq 0$

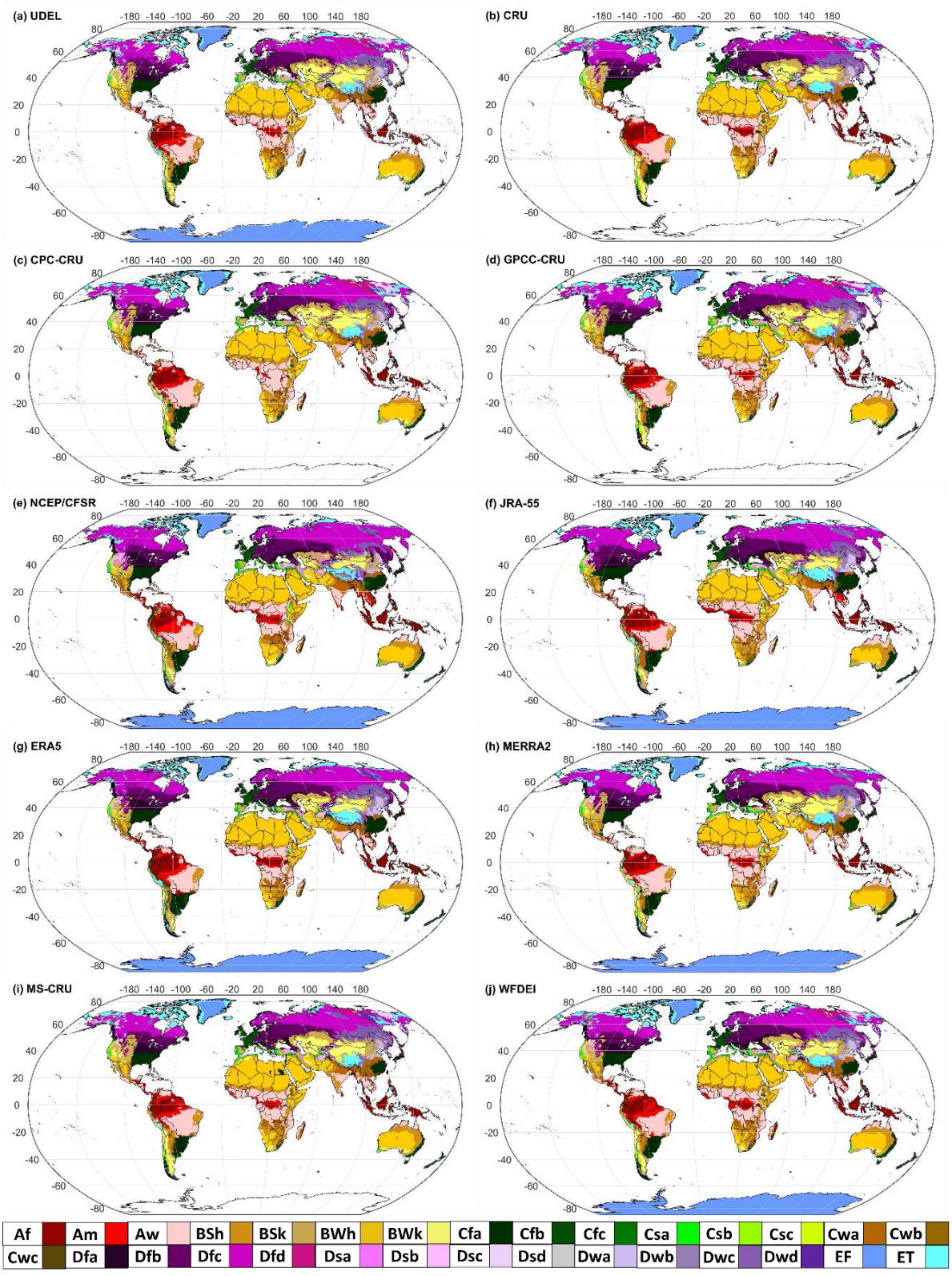

Figure 2.1 Köppen-Geiger world maps at 0.5° resolution for the 1980-2017 period, derived by using different precipitation and temperature products: (a) UDEL, (b) CRU, (c) CPC-CRU, (d) GPCC-CRU, (e) NCEP/CFSR, (f) JRA-55, (g) ERA5, (h) MERRA2, (i) MS-CRU, (j)WFDEI

2.4 Results

2.4.1 Overview

We used monthly temperature and precipitation from ten gridded products to derive global KG climate maps over the 1980-2017 period (Figure 2.1). Visual inspection of the KG maps (Figure 2.1) reveals differences in climate subtypes over regions such as the Alaska, the northern and western Canada, the northeastern Russia (known as Russian Far East), the Middle East and, the central-eastern and the southeast Asia, the northeastern and central Africa, and both the western and eastern of United States.

In Greenland, boundaries of polar frost (EF) and tundra (ET) are similar among observation datasets (Figure 2.1b,c,d) except for UDEL (Figure 2.1a); ET in reanalysis products (Figure 2.1e,f,g,h) is less extended compared to observation datasets, while the boundaries in the multi-source datasets MS-CRU and WFDEI (Figure 2.1i,j) resemble those of observation products. In three maps, the cold climate subtype Dfc dominates in most regions of Alaska, the northern and western Canada, and the northeastern Russia (Figure 2.1a,f,g); however, maps derived from observation datasets (Figure 2.1a,b,c,d) depict in these regions both polar tundra and Dfc. Notable differences among the KG maps are spotted in central Africa for regions described by the tropical climate subtypes Af and Am. These subtypes in observation-based KG maps (Figure 2.1a,b,c,d) cover, in general, a smaller area compared to reanalysis-based KG maps (Figure 2.1e,f,g,h). In the northwestern part of south America and southeast Asia the tropical climate subtypes Am, Af, and Aw, show also different spatial patterns among the maps. Regions described by the dry climate subtypes BSk, BSh, and BWk differ in the western United States, Middle East, Australia, and central Asia. Most regions described by temperate climate subtypes coincide in Europe and the eastern United States; yet there is a distinct region in southern Egypt (and a smaller one in Libya) characterized by the Cfb climate subtype that is only observed in the MS-CRU dataset (Figure 2.1i).

Polar climate subtypes are defined solely on temperature criteria (Table 2.2), thus, the different spatial patterns observed in the KG maps are explained by differences in temperature values among the datasets. However, both temperature and precipitation patterns should be analyzed to understand discrepancies in other climate subtypes. Next, we provide a detailed comparison of the ten KG maps and investigate how differences in

temperature and precipitation values among the products result in different KG climate subtypes.

2.4.2 Detailed Comparison of the KG maps

First, we performed a pairwise comparison of the ten KG maps (shown in Figure 2.1) by assessing the similarity of each pair. Here, similarity is defined as the percentage of grid points in a pair of maps that have the same climate type; the results for the 45 different pairs are presented in the Figure 2.2 heat map.

The lowest level of similarity (67.4%) is observed between the gauge-based CPC–CRU and the reanalysis-based NCEP/CFSR maps; the highest level of similarity (90.4%) is shown between the gauge-based *vs*. multi-source products maps CRU and WFDEI. In general, the percentage of similarity between pairs of reanalysis KG maps is high [82-86.5%] with an average of 84.5%. Pairs of gauge-based KG maps show high variation in similarity [78-89.5%], with an average of 84%. The similarity between gauge-based and reanalysis maps is from 67 to 85 %, with an average of 75%. The KG maps from the two multi-source products are highly similar (84%), yet the WFDEI map hows in general a higher similarity to the other maps than is the MS-CRU map. Only the WFDEI KG map is at least more than 79% similar to the other maps. Compared with the other maps, NCEP/CFSR and WFDEI KG maps show the lowest and highest number of grid points with similar climate types, at an average of 75.4% and 84%, respectively.

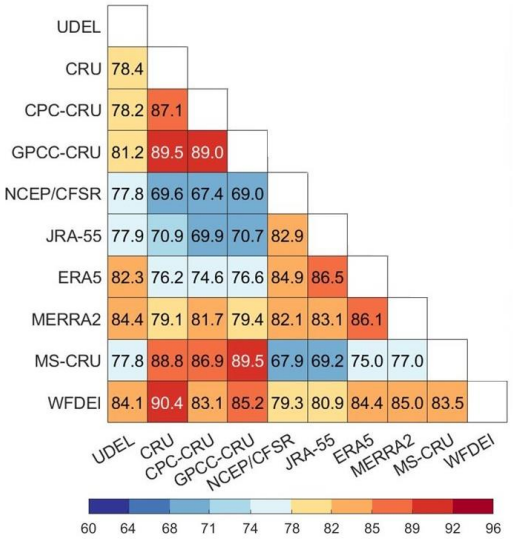

Figure 2.2. Percentage of grid points showing similar climate type in each pair of KG world maps (from 1980 to 2017) derived from ten different gridded products.

These calculations indicate that there are terrestrial regions in the KG maps displaying different climate subtypes. To determine the source of variation we analyzed grid points of each map in geographical zones based on specific latitudes (north polar: $66.5° <$ latitude$\leq 90°$; north temperate: $23.5° <$ latitude $\leq 66.5°$; tropics: $-23.5° <$ latitude $\leq 23.5°$, south temperate: $-66.5° <$ latitude$\leq -23.5°$; south polar: $-90° <$ latitude$\leq -66.5°$). Similarity between all pairs of KG maps within geographical zones (except for the south polar zone) is presented in the heat maps of Figure 2.3. Over the north polar zone (hereafter referred to as the polar zone), we observed 10 distinct climate subtypes from the major KG groups of B, C, D, and E, including BSk, Cfc, Dfc, and EF. The similarity between gauge-based and multi-source KG maps is larger than 90%. (exception is the UDEL KG maps). In addition, 65 to 80% similarity is observed among gauge-based *vs*. reanalysis KG maps; however, the lowest level similarity ($\sim$63%) is observed in MS-CRU *vs*. NCEP/CFSR KG maps.

As latitudes decrease to north temperate zones the diversity of detected climate subtypes increases (28 distinct KG climate subtypes including Af, Am, BSk, BWh, Cfc, Cfb, Dfb, Dfc, and EF). In this zone, we observe a higher similarity in most pairs of KG maps. For instance, 68-84% similarity is shown in maps derived from reanalysis and gauge-based products and in maps derived from UDEL and other gauge-based products. Compared to polar-zone maps, fewer maps show more than 90% similarity, including maps derived from CPC-CRU vs GPCC-CRU. Notably, we see a substantial increase from 73.2 % to more than 83.2% among maps derived from GPCC-CRU vs MERRA2 in polar zones compared to north temperate zones.

Over the tropics, 17 different climate subtypes (including Af, Am, BSk, Cfc, Ef, and ET) are detected from all KG maps. Only KG maps derived from the WFDEI and CRU show more than 90% similarity (Figure 2.3). In general, the highly similar maps show less similarity in the tropics than in the north temperate and polar zones. Over the south temperate zone 24 KG subtypes are detected in all KG maps. In this zone, we observe the lowest level of similarity (78% on average) compared to other zones. The highest similarity (89.4 %) is observed between GPCC-CRU and CRU KG maps.

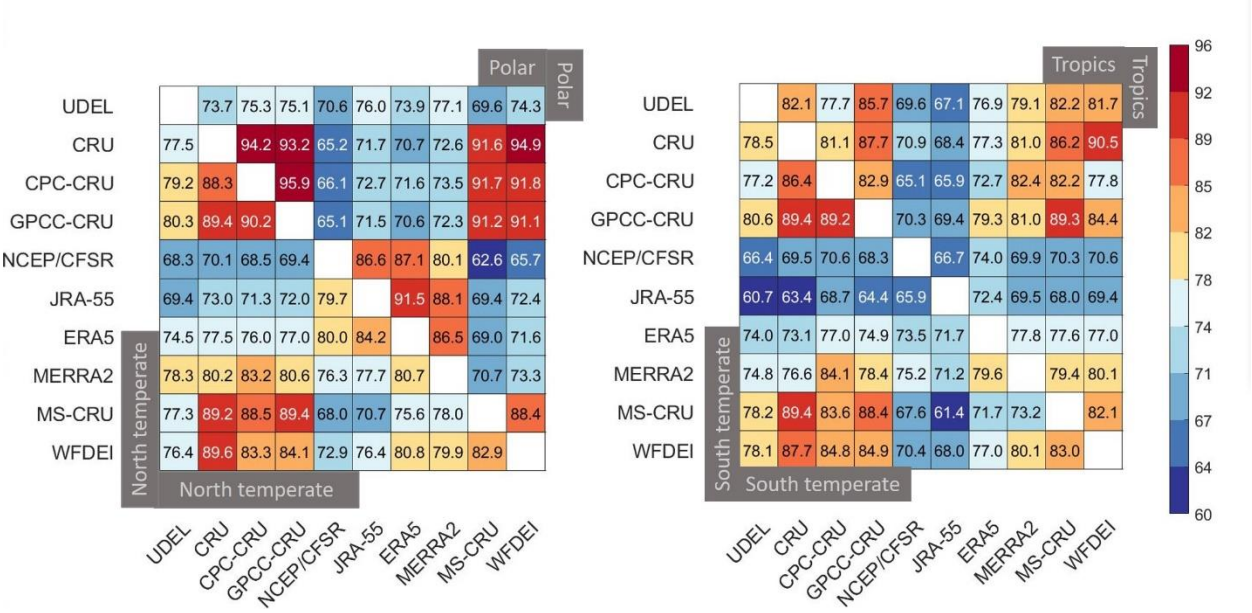

Figure 2.3. Percentage of grid points having the same climate types in pairs of KG maps (from 1980 to 2017) in geographical zones. In the left panel, the upper triangular matrix refers to the polar zone, and the lower triangular matrix to the north temperate zone. In the right panel, the upper triangular matrix refers to the tropics, and the lower triangular matrix to the south temperate zone.

Table 2.3. Average similarity (%) of a KG map with the rest of the maps in geographical zones; green and red colours highlight the maximum and minimum, respectively, in each zone.

KG maps derived from different datasets	South Temperate	Tropics	North Temperate	Polar
UDEL	76.9	80.2	78.1	76.6
CRU	81.4	82.5	83.5	82.8
CPC-CRU	82.2	78.8	82.8	83.3
GPCC-CRU	81.8	83.0	83.3	82.6
NCEP/CFSR	72.7	72.8	75.3	74.9
JRA-55	69.5	71.7	77.4	80.0
ERA5	77.3	78.5	80.6	79.2
MERRA2	79.3	80.0	81.5	79.4
MS-CRU	79.7	81.7	82.0	80.4
WFDEI	81.4	81.4	82.6	82.4

We estimated the average similarity of a KG map with all the rest of maps in different zones (Table 2.3 and marks (×) in Figure 2.4). For example, for the polar zone the MERRA2 map shows 79.4% average similarity. Reanalysis maps show the lowest similarity, whereas gauge-based maps the highest (Table 2.3). More specifically, the NCEP/CFSR map has the lowest average similarity in the north temperate and polar zones (Table 2.3). The highest variation of average similarity in the four zones, as assessed by the range, is observed for the

JRA-55 map with range observed in [69-80%]; in general, the variation in the four zones is much smaller for the other KG maps (see box plots in Figure 2.4 a; rows in Table 2.3). If we focus on the average similarity of all maps within each zone (Figure 2.4 b; columns in Table 2.3) it seems that KG maps agree more for the North temperate zone.

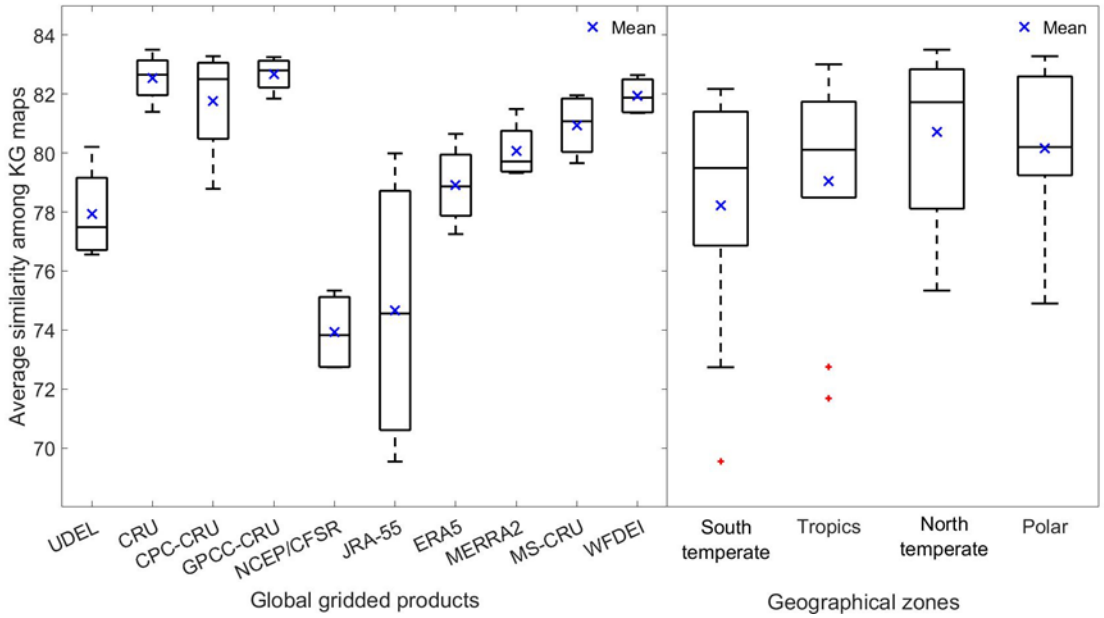

Figure 2.4. Average similarity (%) of: (a) a KG map with the rest of the maps in geographical zones (each box plot is constructed by 4 values; rows in Table 3); (b) KG maps per zone (each box plot is constructed by ten values; columns in Table 3). The blue crosses show the average similarity in each boxplot, while the red crosses show the outliers. The whiskers denote maximum and minimum similarity.

Several KG maps displayed some unexpected climate subtypes. Although we expected to observe the polar subtypes in high latitudes, ERA5 and UDEL KG maps depicted EF regions over the tropics and south temperate zones. Additionally, UDEL, CRU, CPC-CRU, and WFDEI KG maps show regions with a semi-arid cold climate (BSk) in northern/western Canada, which is not realistic as these regions have a cold climate and there are major differences among precipitation and temperature patterns in regions with arid vs cold climates. To investigate these surprising findings and the low similarity among maps, we established which climate subtypes account for these anomalies by assessing the variations in spatial patterns, land coverage and density, of each climate subtype (Figure 2.5 and Table S2). Note that the percentage of land coved by a specific climate type is estimated as the ratio of actual area described by this climate type over the global land area, and not as number of grids over

total number of grids. Also, in cases where products have missing grid points the total land cover (see Figure 2.5 f) will not add to 100%.

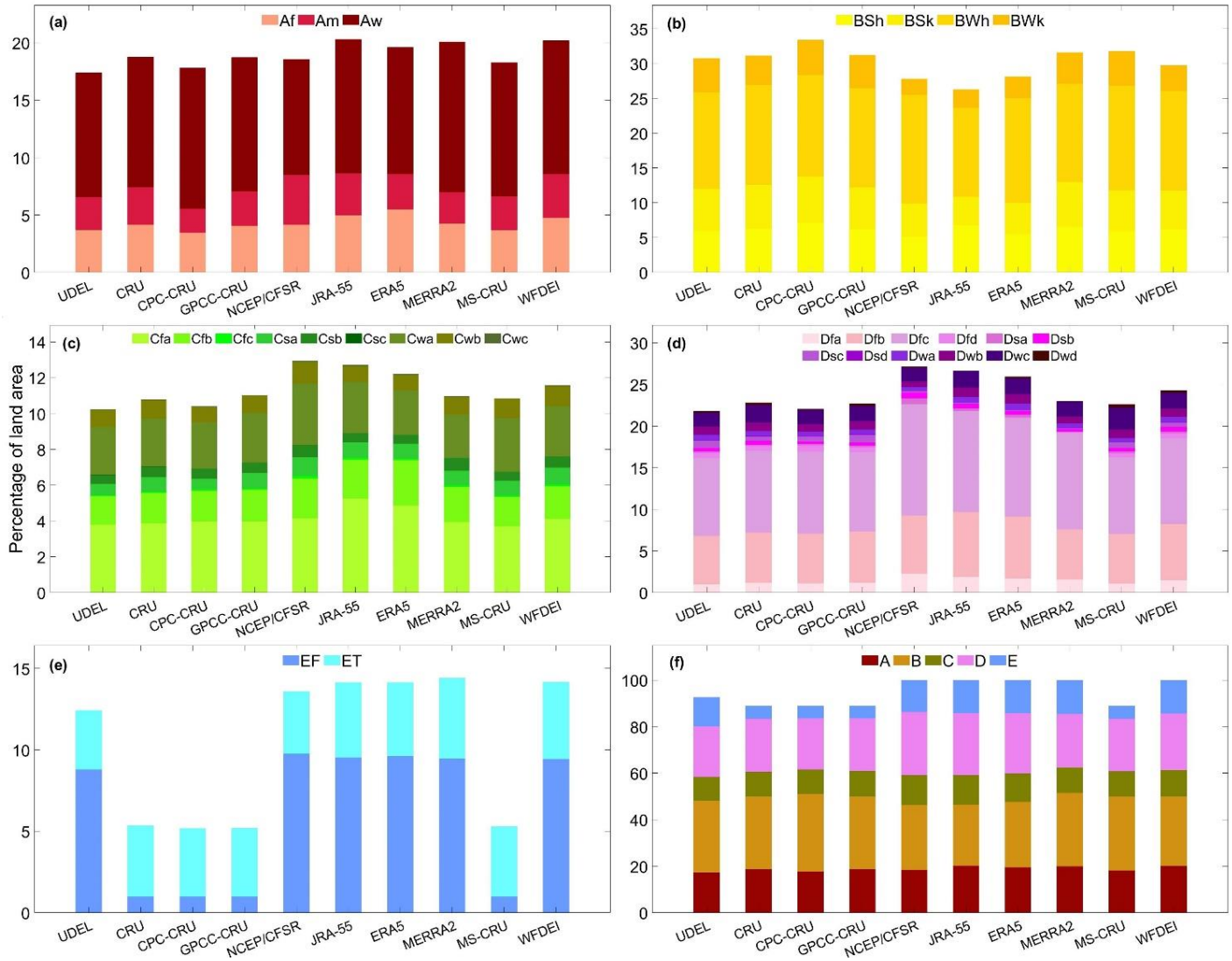

Figure 2.5. Percentage of land area covered by Köppen-Geiger climate subtypes. Panels (a-e) show subtypes of climate types A, B, C, D and E, and panel (f) shows total percentage of land area covered by the major climate types.

Table 2.4. Variation in land coverage of major climate type in KG maps;green and red colours highlight the maximum and minimum, respectively.

	Global gridded products									
Major Climates	UDEL	CRU	CPC-CRU	GPCC-CRU	NCEP/CFSR	JRA-55	ERA5	MERRA2	MS-CRU	WFDEI
A	17.39	18.76	17.81	18.72	18.55	20.29	19.61	20.07	18.27	20.18
B	30.76	31.13	33.41	31.22	27.78	26.25	28.11	31.58	31.79	29.75
C	10.24	10.78	10.39	11.03	12.94	12.71	12.21	10.95	10.85	11.58
D	21.77	22.82	22.06	22.65	27.14	26.61	25.94	22.98	22.64	24.25
E	12.41	5.36	5.17	5.20	13.58	14.14	14.14	14.42	5.30	14.15

As shown in Figure 2.5 and Table 2.4, the arid climate (B) regions with the highest and lowest land coverage are depicted by the CPC-CRU and JRA-55 maps, respectively. For the other major climates (A, C, and D), reanalysis products maps (JRA-55, MERRA2, and NCEP/CFSR) show the highest land coverage, while the UDEL map shows the lowest. For the major climate E, gauge-based maps did not represent the subtypes in Antarctica due to lack of data in this region. This resulted in lower land coverage percentages of EF and ET in these maps (Figure 2.5 e). Clearly, the total land percentage in these maps do not meet the required coverage of 100% (as shown in Figure 2.5 f). Although the NCEP/CFSR map shows the largest area covered by the C climate (~13%), no regions are described by the climate subtype Csc. However, the Csc type exists in all the other maps, covering small regions. The largest variation in land coverage percentage in all ten maps is observed in the Dfc subtype, which in most maps represents the largest portion ($> 9\%$) of the D climate type. The second largest variation is observed in the BWk type, representing major B climate type's lowest land coverage (Figure 2.5).

In 60% of climate subtypes gauge-based product maps show lower land coverage than the others. However, some climate subtypes are missing in the reanalysis maps, for example, Dsd is missing from MERRA2, JRA-55, NCEP/CFSR, and ERA5; Dwd from JRA-55 and MERRA2; and Dfd from JRA-55 (Table S2). To investigate the missing climate subtypes, we focused on their KG climate classification criteria of temperature (T_{cold} and T_{hot}), and precipitation (P_{sdry} and P_{wwet}). According to KG climate classification (Table 2.2), regions with $T_{\mathrm{cold}}<-38$ °C lead to climate subtypes that have "d" as the third letter, including Dwd, Dfd, and Dsd. No regions show $T_{\mathrm{cold}}<-38$ °C in the JRA-55 map, as noted also in Donat et al. (2016b) and Pitman and Perkins (2009). This explains why the JRA-55 KG map does not

include the Dwd, Dfd, and Dsd types. Notably the reanalysis maps show warmer T_{cold} than gauge-based maps as highlighted by Wang and Zeng (2013) and Kharyutkina et al. (2012). One of the coldest places on earth is Yakutia (Sakha) located in north-eastern Russia (55.29 N to 76.46 N and 105.32 E to 162.55 E). Studies show that the average and minimum temperature in the coldest month is below -40°C and -60°C, respectively (Nazarova et al., 2011; Petrov et al., 2011). However, neither the MERRA2 nor the JRA-55 T_{cold} maps showed regions with $T_{\text{cold}} < -40$°C. However, over Yakutia, the range of T_{cold} CRU map is $[-54.1, -38$ °C]. Our findings indicate that reanalysis products (in particular JRA-55) do not represent well minimum temperature patterns in this region. Although regions having $T_{\text{cold}}<-38$ °C are spotted in the MERRA2, NCEP/CFSR, and ERA5 T_{cold} maps, the rest of the criteria defining the Dsd climate subtype ($P_{\text{sdry}} < 40$ mm and $P_{\text{sdry}} < P_{\text{wwet}}/3$) are not fulfilled. None of the regions in the MERRA2 P_{wdry} map depicts $T_{\text{cold}}<-38$°C, thus, MERRA2 KG map does not include the Dwd type. Notably, the other KG maps depict Dfd, Dsd, and Dwd but in less that 2% of grid points for each subtype.

Cleary, the temperature and precipitation products we use, differ with each other since they use different sources and methods to estimate their values. This can lead to different climate type assessment for the same grid point. To measure the climate-type uncertainty in the constructed KG maps we counted the number of different climate types observed in each grid among the ten KG maps. The uncertainty in major climate types and subtypes is depicted in a,b. Globally, 82.1% of grid points show the same major climate type, yet 16.4% of grid points are described by two different major types, or more generally, 17.9% of grid points are described by more than one (up to four) major climate type (Figure 2.6a).

The variability of climate subtypes at grid points, as anticipated, is even larger and results in coherent spatial patterns (Figure 2.6b). Specifically, only 62.8% of grid points show the same climate subtype (Figure 2.6 b) with agreement observed in Antarctica, Central Russia, Greenland, the northern part of Africa, and some regions in the eastern United States and Brazil. Approximately, 27% and 8% of the grid points are described by two and three different subtypes, respectively; these grid points are located, for example, in large regions of Australia, central and southern Africa, and the western United States. Regions

having four climate subtypes (almost 2% of grid points) are spotted in southern Africa, western parts of South America, north-eastern Russia, and in the mountainous regions north of India. Five climate subtypes (0.5%) are spotted in western America, eastern and southern Africa, eastern Asia, and eastern Australia; six climate subtypes (0.03%) are observed in small regions of America, Asia, and Africa, and seven climate subtypes (0.008%) in a few grid points in Iran, Mexico, China, Peru, Bolivia, and Madagascar.

The variability of climate subtypes in specific regions differs also in each product. For example, the subtypes of EF and ET in Greenland are uncertain due to the lack of gauge-based data in that region. Over the tropics, western America, Mexico, central and southern parts of Africa, central Asia, and China, the reanalysis products show more climate subtypes than the gauge-based products. However, over the polar zone (e.g., Alaska, western Canada), and the central Africa, gauge-based KG maps show more climate subtypes than the reanalysis maps. Overall, compared with other regions, uncertainty among climate subtypes in the Middle East, western America, China, and north-eastern Russia is high. In these regions, the low density of stations and the topographic complexity (high elevations and mountainous regions) may be the reason for higher uncertainty among climate subtypes. This agrees with the findings of Beck et al. (2018).

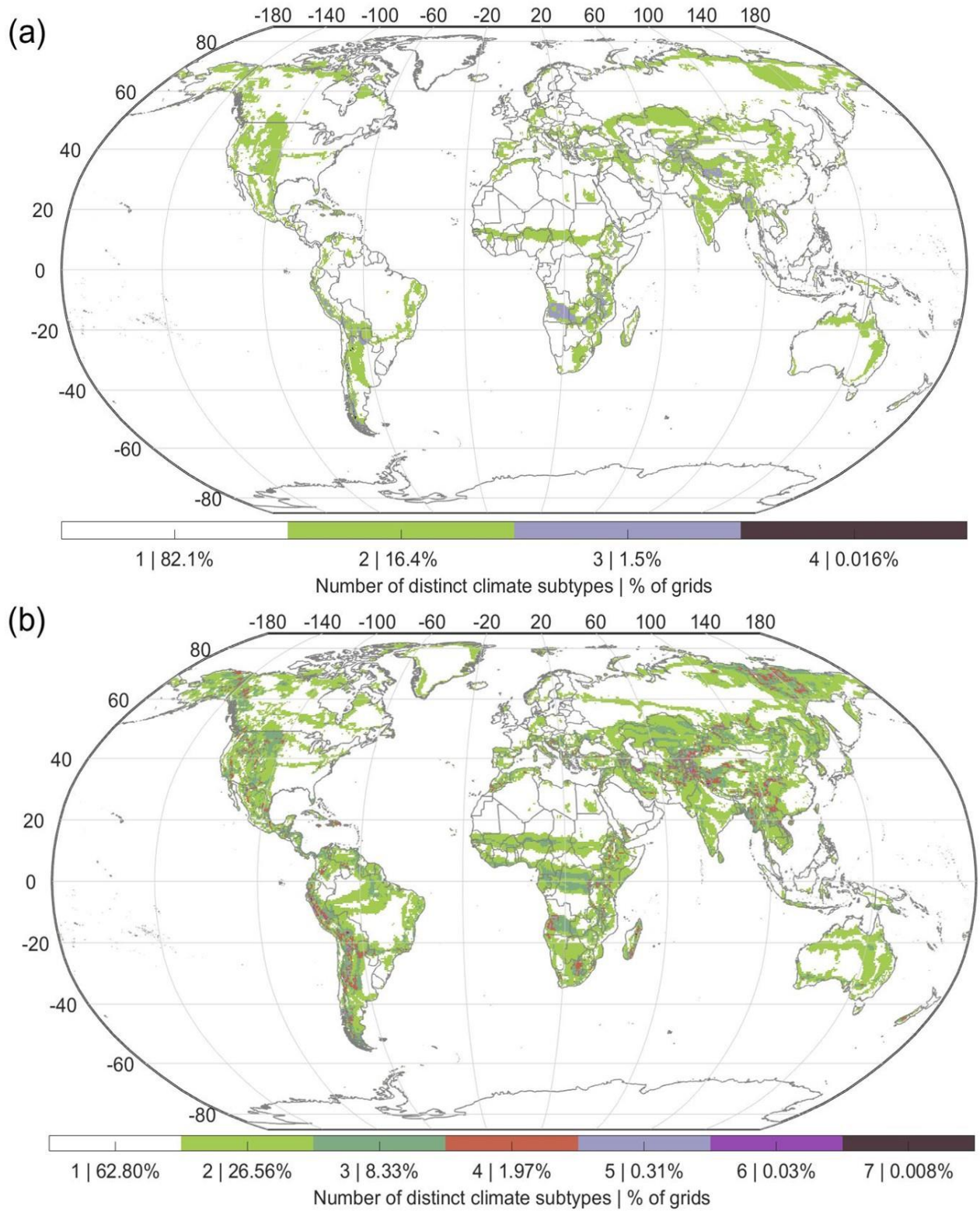

Figure 2.6. Number of distinct Köppen-Geiger (a) major climate types, (b) climate subtypes in grid points among the ten KG maps derived for the 1980-2017 period.

2.4.3 Merging the different KG maps

The previous analysis showed that the ten KG maps have similarities and differences. To merge these results and determine the most robust climate subtype at each grid point we constructed a KG master map where the climate subtype at each grid point is the most frequently observed in the ten KG maps (Figure 2.7a). However, approximately 2% grid points do not have a single most frequent climate subtype; for example, in 0.03% of grid points the BSk and BWk types are observed in five different KG maps each. In such cases we performed a regional analysis to assess which one of the two equally frequent subtypes is more frequent in the region. Particularly, we studied 80 surrounding grid points in order to determine the climate subtype of each ambiguous grid point.

To assess which single product produces the most reliable KG map we compared the similarity of each of the ten KG maps with the KG master map (Figure 2.8). For example, the JRA-55 map shows a low 80% similarity with the KG master map whereas the WFDEI map has a high similarity$>$ 90%. Reanalysis KG maps have in general less than 88% similarity with the KG master map, while gauge-based and multi-source KG maps show more than 88% similarity. Notably, the lowest similarity ($<$ 80%) is observed for the NCEP/CFSR map. Based on our assumption that the master map is more reliable than all individual maps, the gauge-based and WFDEI KG maps might offer more reliable KG maps than the rest. However, WFDEI is also good option as gauge-based KG maps do not define climate subtypes at many grid points because of lack of station data (Table S2).

In addition to the master map, we developed another map that combines temperature and precipitation data from the ten gridded products (Figure 2.7b). Because some regions have few stations, merging gauge-based and reanalysis products is not always reliable. This difficulty must be considered when choosing methods to merge temperature and precipitation data from different gridded product into one dataset. Options include, weighting methods, objective analysis, and statistical methods. Weighting methods such as Bayesian Moving Average (BMA) (Triantafyllopoulos and Nason, 2007) are not applicable because there are no independent station data to evaluate the weight from the many stations used in gauge-based products (e.g., CPC and GPCC). In terms of the objective analysis methods, the Triple collocation method (Stoffelen, 1998) is also not applicable for two reasons: first, it only accepts three input datasets, while we use ten global products, and

second, its input datasets must be independent, whereas our gauge-based products have many overlapping data.

A statistical approach was more appropriate as the products depend on observations. Some products use the observation data (gauge-based products) and others (including reanalysis and multi-source products) are bias corrected using observations. Since we did not use climate model outputs, statistical methods work well, enabling us to compile a single dataset of precipitation and temperature. After calculating the time series of median values of monthly temperature and precipitation data at each grid point in all products (discarding 2017 data records as they are not covered by the GPCC dataset), we used this initial dataset to develop the second master KG map (Figure 2.7b). The two master KG maps are 95% similar, with most climate types showing less than one percent difference in land coverage (except for the B climate, which shows a difference of more than 1.4%; see Table 2.5). This land coverage percentage agrees with the finding of Chen and Chen (2013) and Rubel and Kottek (2010) (Table S2). Although KG maps derived from several products do not include the climate subtypes of Dsd, Dwd, Dfb, and Csc, these types are present in the two master KG maps (Table S3).

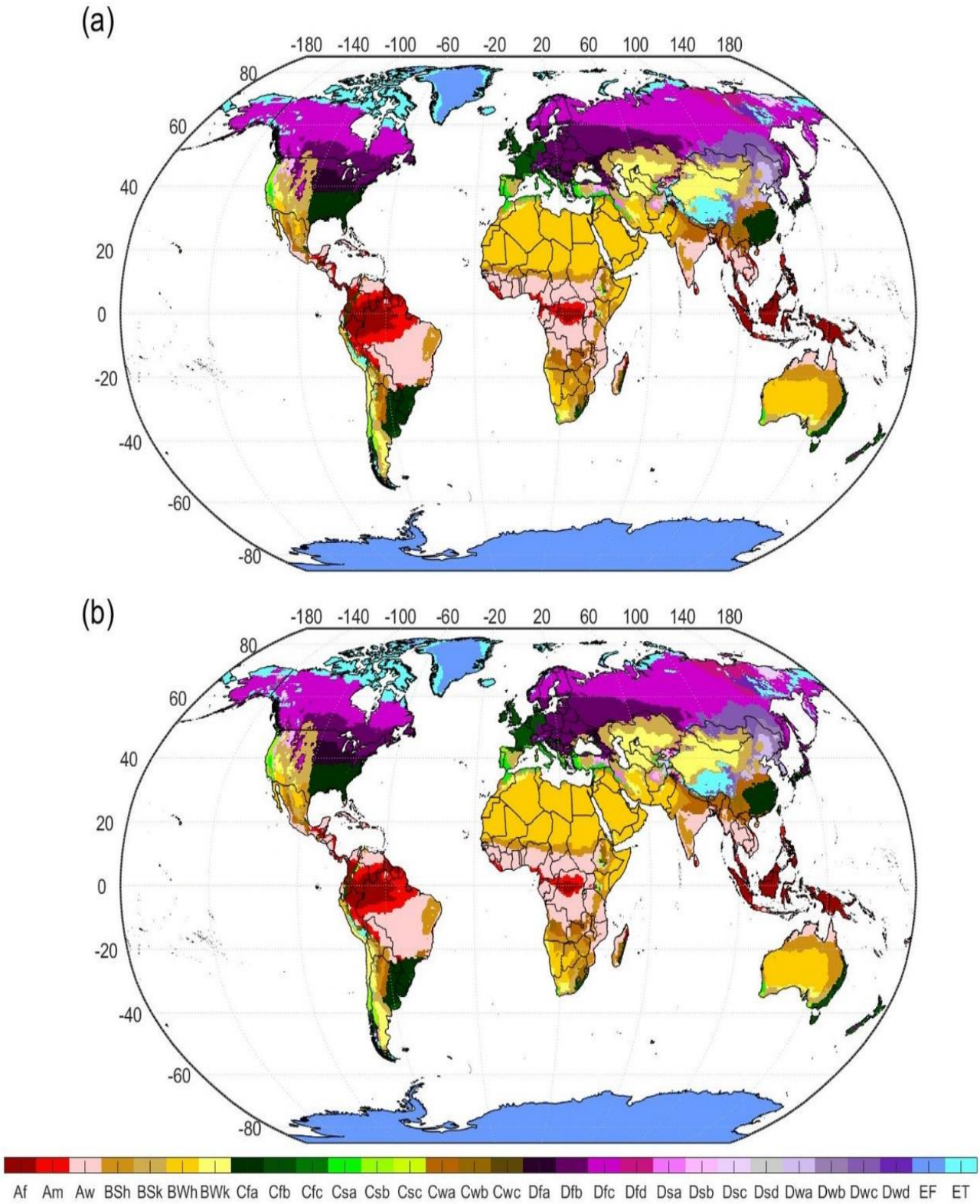

Figure 2.7. Master KG maps for the 1980-2017 period constructed by (a) depicting the most frequent climate subtype among all KG maps, and (b) merging temperature and precipitation data from all gridded products into a single dataset and using it to assess the climate subtypes.

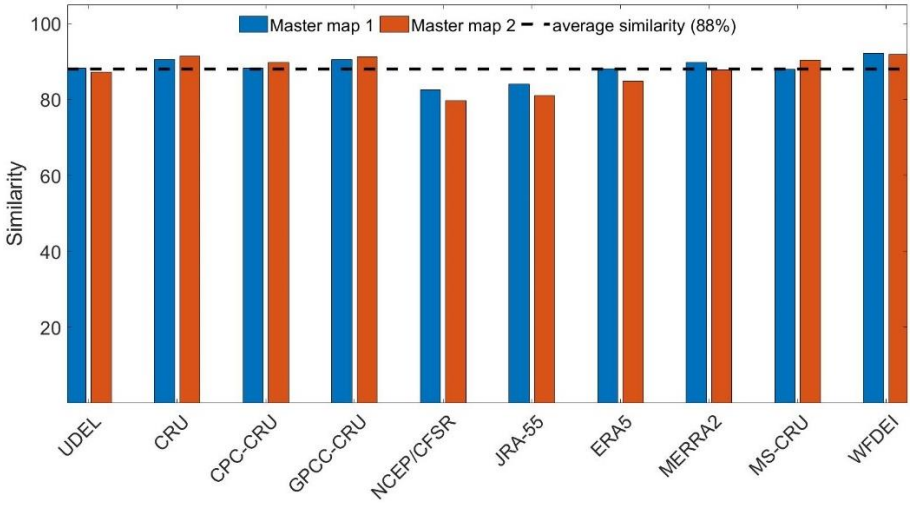

Figure 2.8. Similarity of individual KG maps shown in Figure 2.1 with the two master KG maps shown in . The dashed line shows the average similarity (88%) between all individual maps and the master maps 1 and 2.

Table 2.5. Percentage of land represented by major KG climate types in the master and merged KG maps.

Major climate type	Master KG map 1 (more frequent climate subtype)	Master KG map 2 (merging precipitation and temperature products)
A	19.90%	19.32%
B	31.25%	32.60%
C	11.31%	11.02%
D	23.50%	23.16%
E	14.04%	13.91%
Total	100.00%	100.00%

2.5 Summary and Conclusions

Here, we derived KG climate classification maps using ten gridded precipitation and temperature datasets including four gauge-based, four reanalysis, and two multi-source global products. First, we assessed the similarity of the ten KG maps through a pairwise comparison at global and zonal scales; similarity between two maps is defined here as the percentage of grid points having the same KG climate subtype. In general, there are notable differences among the maps with similarity between gauge-based and reanalysis KG maps being lower than in other pairs (e.g., between gauge-based and multi-source maps). Focusing on different geographical zones (South Temperate, Tropics, North Temperate, and Polar), the analysis shows that, in general, the highest and lowest similarity among the maps is

observed in the North and South Temperate zones, respectively. In all KG maps, the North temperate zone displayed the largest number of climate subtypes.

In a large percentage of grid points there is notable variability (or uncertainty) even in major climate types among the ten maps. Specifically, the analysis shows that 82.1% of grid points among the ten maps have the same major climate type, however, 17.9% of grid points are described by more than one major climate type. The analysis also reveals coherent spatial patterns of grid points described with more than one major climate type. Investigation of the climate subtypes shows a stronger uncertainty with only 62.8% of grid points having the same subtype. Some notable regions where the maps agree are spotted in Antarctica, Central Russia, Greenland, the northern part of Africa, and some regions in the eastern United States and Brazil. The 37.2% of the grid points are described by more than one climate subtype (up to seven subtypes in some cases) and very large regions all over the globe (e.g., in south Asia, central and south Africa, west North and South America, etc.) are marked as ambiguous in term of their climate subtype.

To exploit the information from these ten global datasets and reduce the uncertainty in characterizing the climate in different regions we implicitly and explicitly combined the datasets to create two robust KG maps. The first KG master map assigns in each grid the most frequently observed climate subtype among the ten KG maps. The second KG master map combines temperature and precipitation data from the ten gridded products and creates a unique set of temperature and precipitation which is then used to construct the KG map. The two master maps show more robust spatial patterns than the individual ones and the similarity between them is 95%. Also, specific climate subtypes that were not found in some individual maps (e.g., in some reanalysis maps) are observed in the two master maps. We also used the first master map benchmark to test which one of the individual maps is the most reliable. If the focus is only on similarity then the GPCC-CRU is the most reliable product, yet since there are climate subtypes missing and the WFDEI shows similar performance we deed the latter is a better choice.

As a future direction, it worth exploring different climate classifications and their variation in different products and potential effects of downscaling methods for finer spatial resolution maps. Also, the true variability of the climate subtypes in each grid cannot be revealed by the datasets used here or from any other set. Instead, large ensemble datasets

based on stochastic methods could quantify more robustly the true uncertainty. Although this research could be further refined, we believe we revealed the large uncertainty in climate classification and offered robust KG maps that will help researchers to better evaluate future climate shifts.

2.6 Supplementary material

Table S1. Precipitation gauge data used in reanalysis datasets.

Dataset name	Region	Observations
NCEP/CFSR	All grids	CPC Merged Analysis of Precipitation (CMAP)
WFDEI	All grids	CRU TS3.101 gauge data (TS3.21 for 2010-2012) (daily/0.5°)
JRA-55	All grids	Global Precipitation Climatology Centre (GPCC), Global Precipitation Climatology Project (GPCP)
MERRA 2	High latitude land (lat > 62.5)	None
	Mid to high latitude land (42.5 < lat<62.5)	CPCU[1] gauge data (daily/0.5°)
	Low to mid-latitude land except Africa (lat<42.5)	
	Africa and oceans	GPCO2.1/CMAP[2] satellite and gauge data
ERA5	All grids	Global precipitation monitoring mission Microwave Imager (GMI), Global Precipitation Climatology Centre (GPCC), Global Precipitation Climatology Project (GPCP)

[1]CPC Unified gauged-Based Analysis of Global Daily Precipitation (Xie et al., 2010)
[2] NOAA Climate Prediction Center (CPC) Merged Analysis of Prediction/Global Precipitation Climatology Project version 2.1 (Adler et al., 2003; Xie et al., 2007)

Table S2. Number of grid points with KG climate subtypes in the ten KG maps.

Climate Type	UDEL	CRU	CPC-CRU	GPCC-CRU	NCEP/CFSR	JRA-55	ERA5	MERRA2	MS-CRU	WFDEI	Average
Af	1770	1993	1645	1951	1988	2380	2628	2039	1756	2279	2043
Am	1374	1559	1014	1428	2087	1761	1488	1311	1420	1838	1528
Aw	5268	5526	5956	5680	4891	5682	5373	6370	5662	5655	5606
BSh	3047	3200	3626	3163	2623	3466	2834	3313	3015	3145	3143
BSk	3879	4031	4253	3831	2969	2533	2771	4072	3763	3526	3563
BWh	7204	7494	7623	7430	8105	6642	7832	7379	7815	7461	7499
BWk	3038	2588	3097	2947	1372	1589	1907	2759	3069	2280	2465
Cfa	2132	2170	2226	2223	2299	2923	2711	2203	2076	2316	2328
Cfb	977	1121	1119	1161	1401	1405	1588	1241	1091	1209	1231
Cfc	33	46	52	45	105	86	56	62	51	76	61
Csa	378	488	358	518	623	511	512	481	496	556	492
Csb	293	350	349	336	397	298	285	419	303	368	340
Csc	2	6	2	3	0	3	0	9	3	1	4
Cwa	1380	1404	1352	1453	1765	1495	1282	1255	1562	1472	1442
Cwb	491	527	437	498	610	462	444	512	553	573	511
Cwc	9	5	10	9	22	20	23	5	5	14	12
Dfa	666	770	742	802	1519	1269	1116	1020	716	996	962
Dfb	4430	4645	4566	4689	5253	5823	5651	4582	4550	5164	4935
Dfc	9353	9903	10006	9688	13473	12388	12160	11751	9301	10328	10835
Dfd	761	763	983	792	74	0	77	63	659	814	554
Dsa	96	88	89	118	428	161	172	51	132	121	146
Dsb	276	301	209	224	441	360	306	218	265	351	295
Dsc	891	547	644	940	95	77	50	24	706	546	452
Dsd	62	93	61	126	0	0	0	0	22	76	73
Dwa	398	376	340	372	314	456	481	394	321	395	385
Dwb	639	699	610	656	425	765	801	525	697	669	649
Dwc	1278	1660	1281	1419	1296	1627	1526	1521	2201	1525	1533
Dwd	168	302	114	240	90	0	199	0	477	236	228
EF	2108	1878	1878	1878	2455	2015	2123	1821	1878	1907	1994
ET	3886	5142	5033	5048	4391	5321	5123	6111	5110	5571	5074
Antarctica cells	22795	0	0	0	24288	24281	24280	24288	0	24257	24032
Total NA land cells	6717	26124	26124	26131	0	0	0	0	26124	74	18549
Total # land cells	85799	85799	85799	85799	85799	85799	85799	85799	85799	85799	85799

Table S3. Total number of grids and percentage of land area representing grids covered by climate subtypes from KG major climate types among the two master KG maps.

KG climate subtypes	Master KG map 2 (merging precipitation and temperature products)		Master KG map 1 (more frequent climate subtype)		Difference (Land coverage)	Difference (Number of cells)
	Land area covered by climate subtypes	Number of cells covered by climate subtypes	Land area covered by climate subtypes	Number of cells covered by climate subtypes		
Af	4.07%	1939	4.70%	2245	-0.64%	306
Am	2.98%	1433	3.16%	1522	-0.18%	89
Aw	12.27%	5977	12.04%	5868	0.23%	109
BSh	6.32%	3201	6.40%	3249	-0.08%	48
BSk	6.14%	3903	6.18%	3925	-0.04%	22
BWh	15.29%	7963	14.53%	7579	0.76%	384
BWk	4.85%	3002	4.13%	2564	0.72%	438
Cfa	3.94%	2200	4.12%	2299	-0.18%	99
Cfb	1.84%	1221	1.96%	1287	-0.12%	66
Cfc	0.09%	69	0.09%	65	0.01%	4
Csa	0.79%	475	0.84%	505	-0.05%	30
Csb	0.64%	383	0.57%	343	0.07%	40
Csc	0.00%	2	0.00%	0	0.00%	2
Cwa	2.68%	1394	2.74%	1427	-0.06%	33
Cwb	1.01%	520	0.99%	506	0.03%	14
Cwc	0.02%	10	0.01%	6	0.01%	4
Dfa	1.21%	781	1.28%	832	-0.07%	51
Dfb	6.23%	4769	6.44%	4923	-0.21%	154
Dfc	10.62%	10738	11.10%	11330	-0.48%	592
Dfd	0.62%	837	0.44%	582	0.18%	255
Dsa	0.18%	107	0.17%	101	0.01%	6
Dsb	0.41%	261	0.44%	279	-0.03%	18
Dsc	0.38%	401	0.20%	213	0.18%	188
Dsd	0.01%	12	0.00%	1	0.01%	11
Dwa	0.55%	345	0.59%	370	-0.04%	25
Dwb	0.92%	614	0.94%	628	-0.02%	14
Dwc	1.80%	1381	1.74%	1338	0.06%	43
Dwd	0.22%	248	0.16%	180	0.06%	68
EF (Antarctica excluded)	1.01%	1907	1.06%	1990	-0.05%	83
ET	4.44%	5418	4.52%	5354	-0.08%	64
Antarctica	8.46%	24288	8.46%	24288	0.00%	0
nans	0.00%	0	0.00%	0	0.00%	0
total land area	100.00%	85799	100.00%	85799	0.00%	3260

2.7 Annex

This section of Chapter 2 provides a detailed explanation of gauge-based, reanalysis, and multisource products, all of which were used to develop KG maps. Gauge-based or land-based observation products are usually grided at a 0.5° resolution using extensive sparsely distributed, mostly homogenized station records. Reanalysis products provide a consistent and complete representation of past weather observations at different gridded resolutions by combining the historical data—observation data made in the past—and today's weather models. Multi-source products combine data from gauge-based, reanalysis, and satellite-based products at different resolutions to provide a better estimation of weather data. To provide a consistent grid system for each product, their grid systems are changed to a specific grid system of 0.5° resolution (360×720) by using the bilinear interpolation method, Also, this section presents figures and maps that are not referred to in the manuscript but that can help in interpreting the results. Figure 2.9 presents a KG map derived from each of the ten distinct global products of either precipitation, temperature, or both. Most of the precipitation and temperature data used to produce each KG map were from similar products, except for GPCC, CPC, and MSWEP, which only provide precipitation data. These precipitation data sets were used along with temperature data from CRU TS (CRU) to produce KG maps. As an example, Figure 2.9a shows the KG map derived using temperature and precipitation from UDEL, while Figure 2.9c and Figure 2.9d show KG maps using precipitation data from GPCC and CPC and CRU temperature data, respectively. Figure 2.1 in chapter 2 also shows each KG map but in a smaller size. To show which regions meet the required criteria for each missing climate subtypes — Dsd, Dwd, and Dfd— $T_{\text{cold}}, T_{\text{hot}}, P_{\text{wdry}}, P_{\text{sdry}}$maps were derived from all reanalysis products (NCEP/CFSR, JRA-55, ERA5, MERRA2) and gauge-based-product of CRU shown in Figure 2.10 to Figure 2.13, respectively. Figure 2.10 shows that regions with $T_{\text{cold}} < -38$ ℃ have climate subtypes with "d" as the third letter. According to KG classification criteria (see Table 2.2), Figure 2.11 shows the spatial patterns of T_{hot}: ($T_{\text{hot}} \leq 0, T_{\text{hot}} \geq 0, T_{\text{hot}} \leq 10, T_{\text{hot}} \geq 10, T_{\text{hot}} \geq 22$). Figure 2.12 shows regions meeting the required criteria of precipitation to be defined as Dw climate type ($P_{\text{wdry}} < P_{\text{swet}}/10$). Figure 2.13 shows regions meeting the required criteria for precipitation to be defined as Ds climate type ($P_{\text{sdry}} < 40$ & $P_{\text{sdry}} < P_{\text{wwet}}/3$).

Notably, Figure 2.9 to Figure 2.13 show how each map varies over Yakutia (Sakha). Notably, large uncertainty among KG maps and variations in temperature and precipitation indices were observed in this region, whose average minimum annual temperature is less than−40°C. Additionally, Figure 2.14 shows the topographic map on each of grid points in the terrestrial regions presented at 0.5 resolution. Figure 2.15 shows average number of precipitation station data per month over the study period, adopted from GPCC dataset.

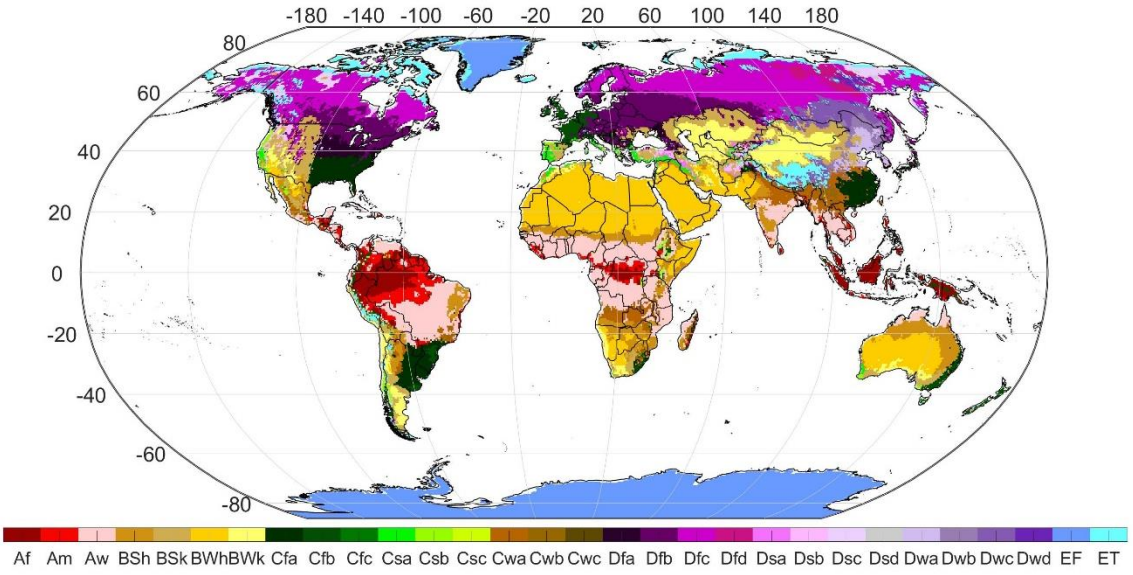

(a) UDEL (T and P)

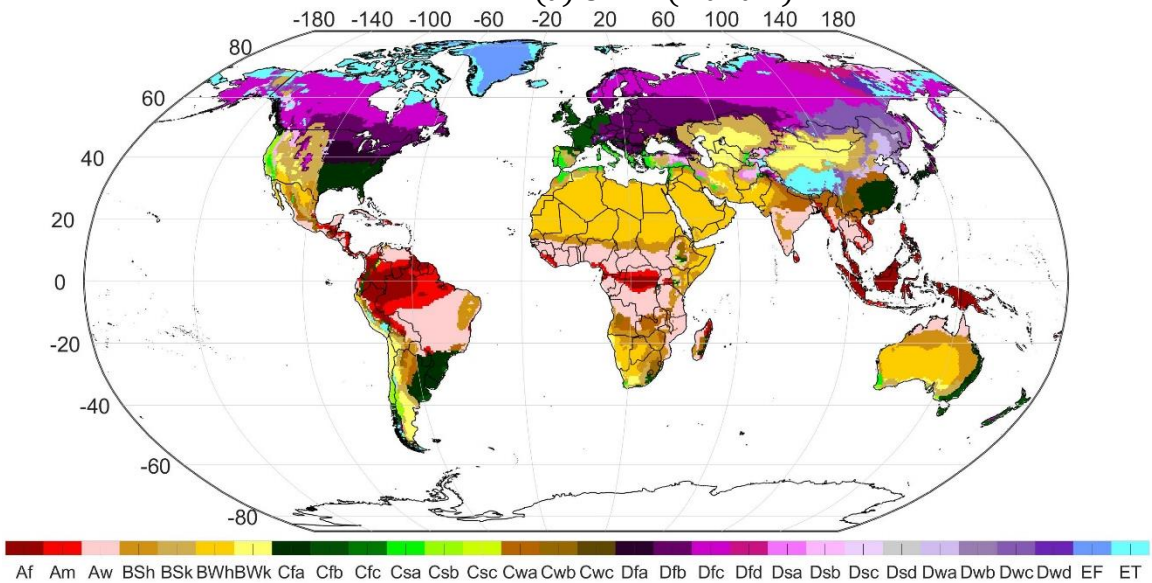

(b) CRU (T and P)

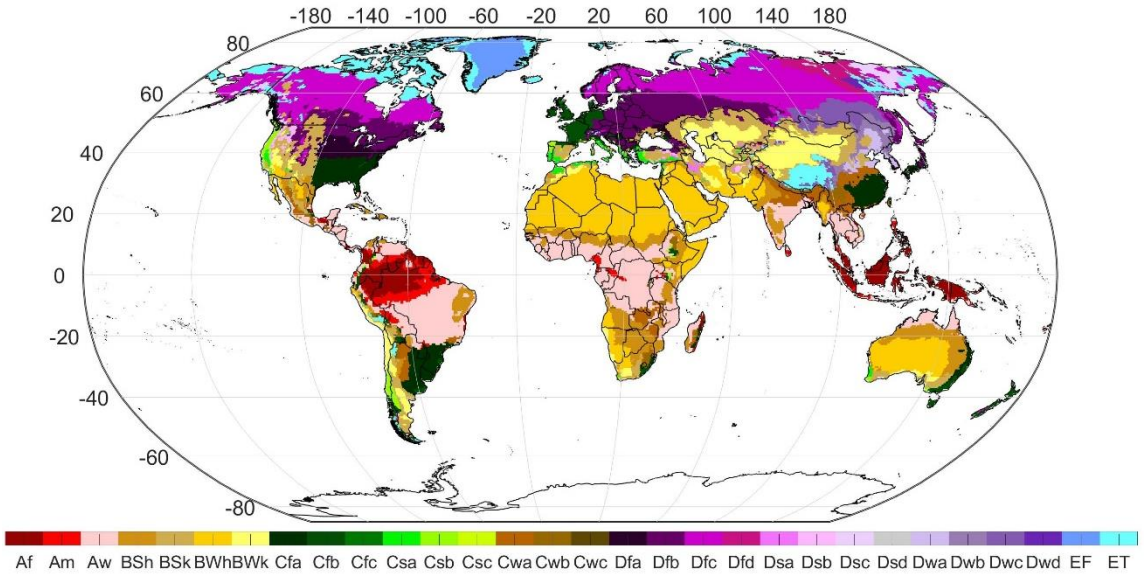

(c) CPC (P)-CRU (T)

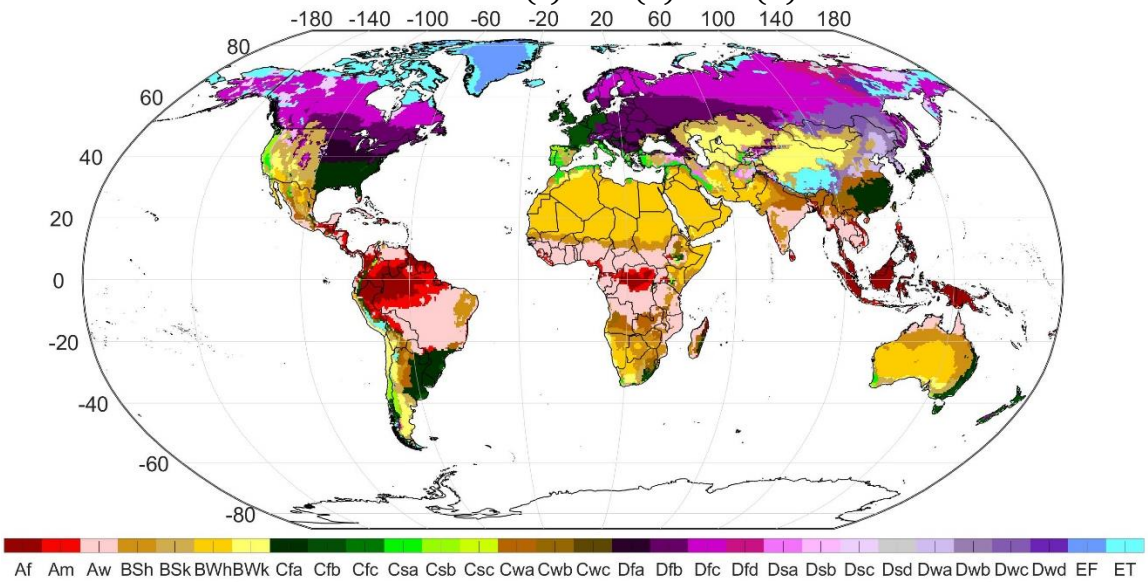

(d) GPCC (P)-CRU (T)

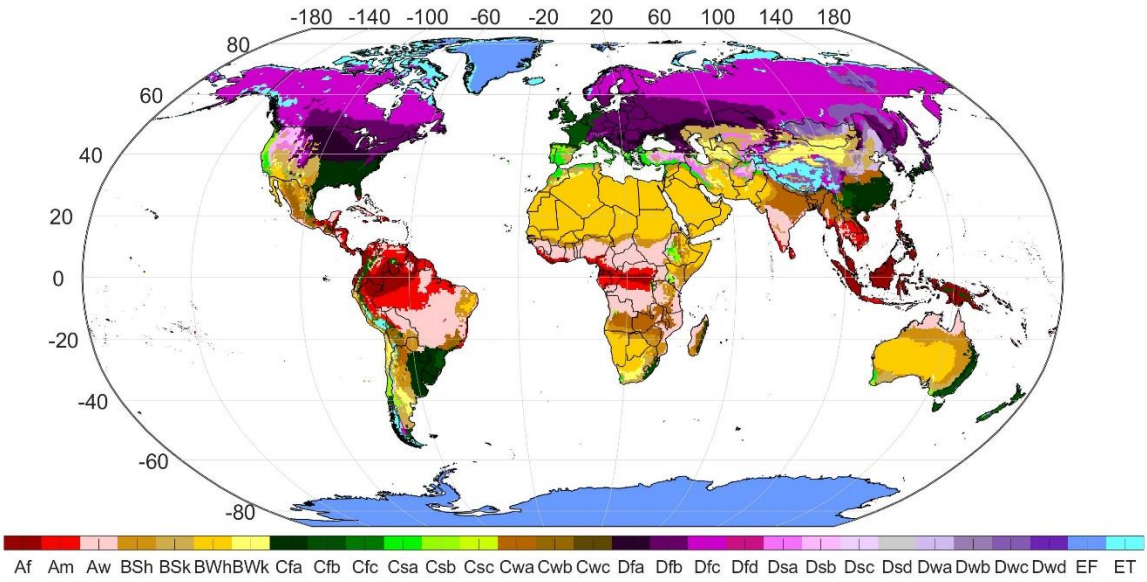

(e) NCEP/CFSR (T and P)

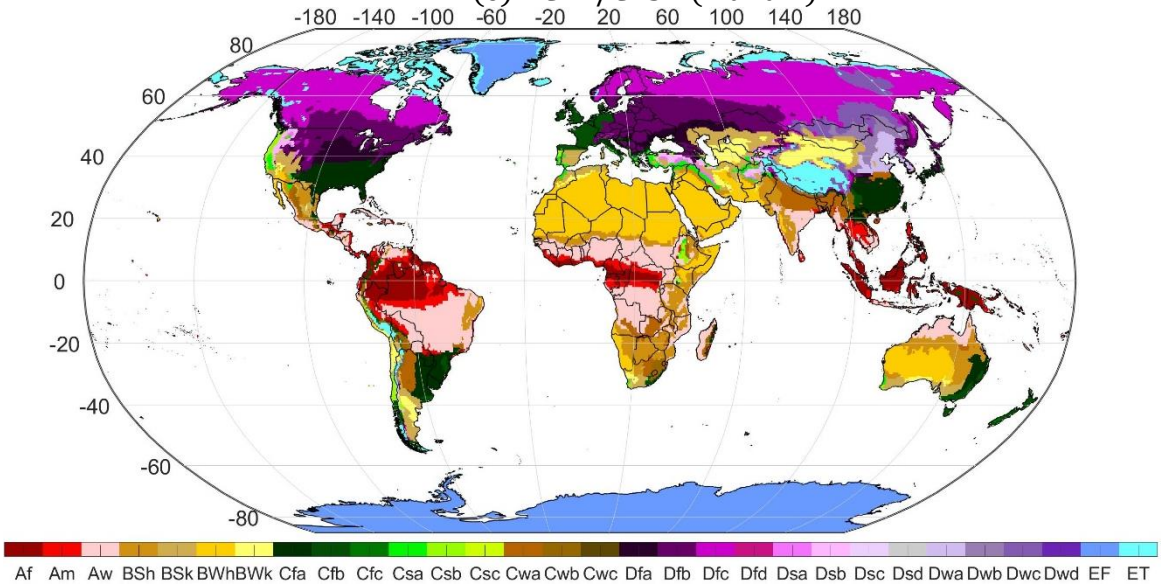

(f) JRA-55 (T and P)

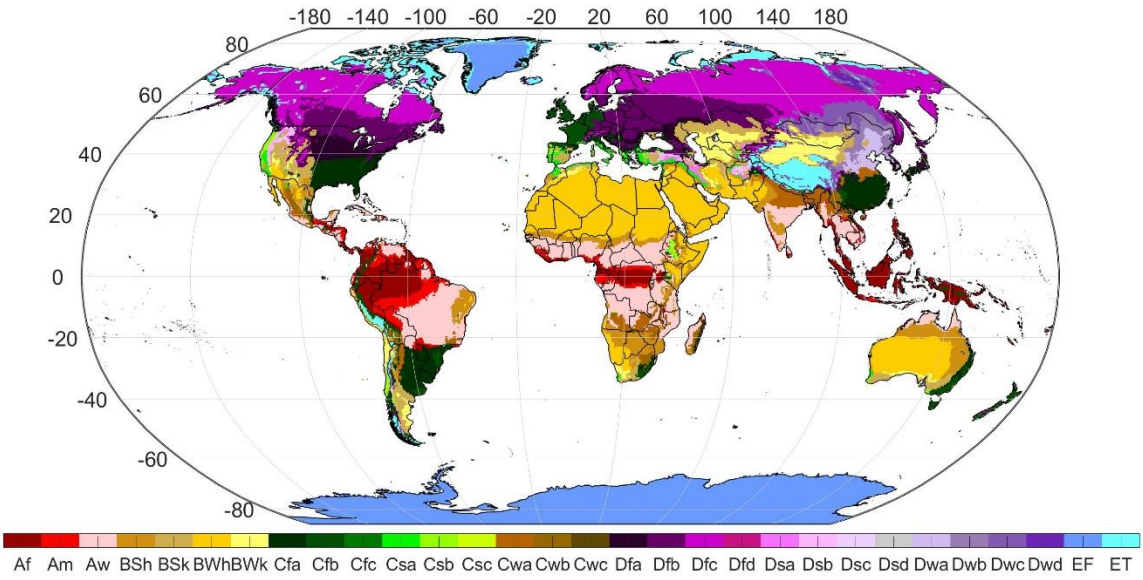

(g) ERA5

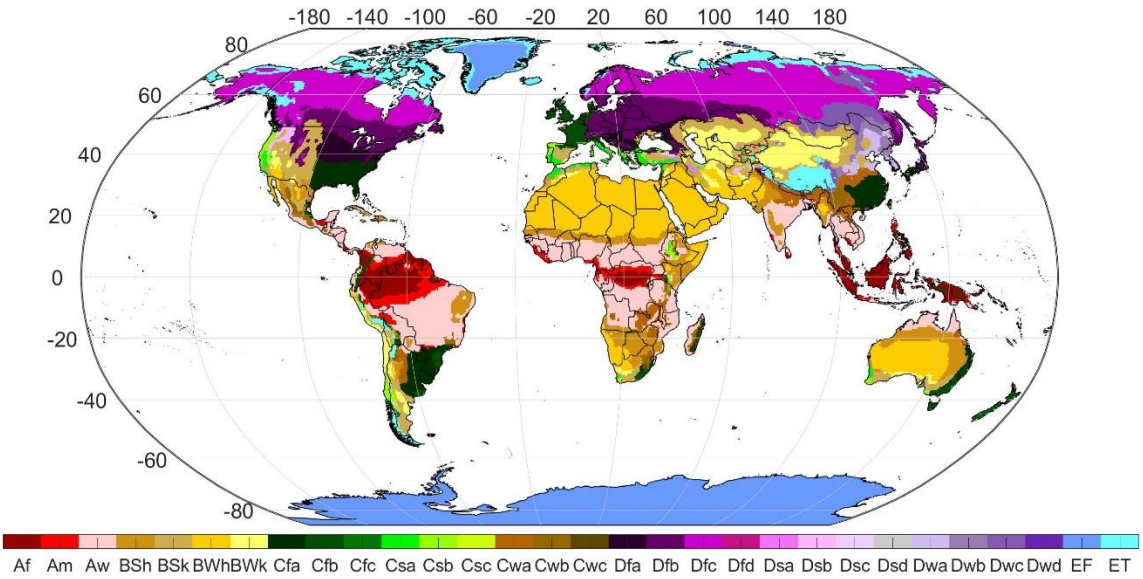

(h) MERRA2 (T and P)

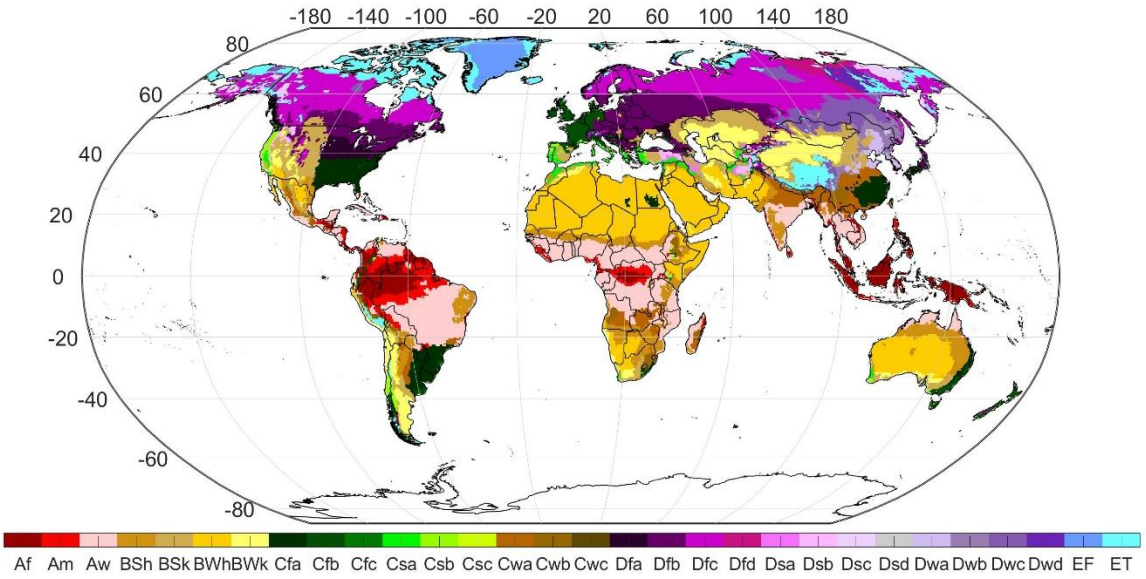

(i) MS(P)-CRU(T)

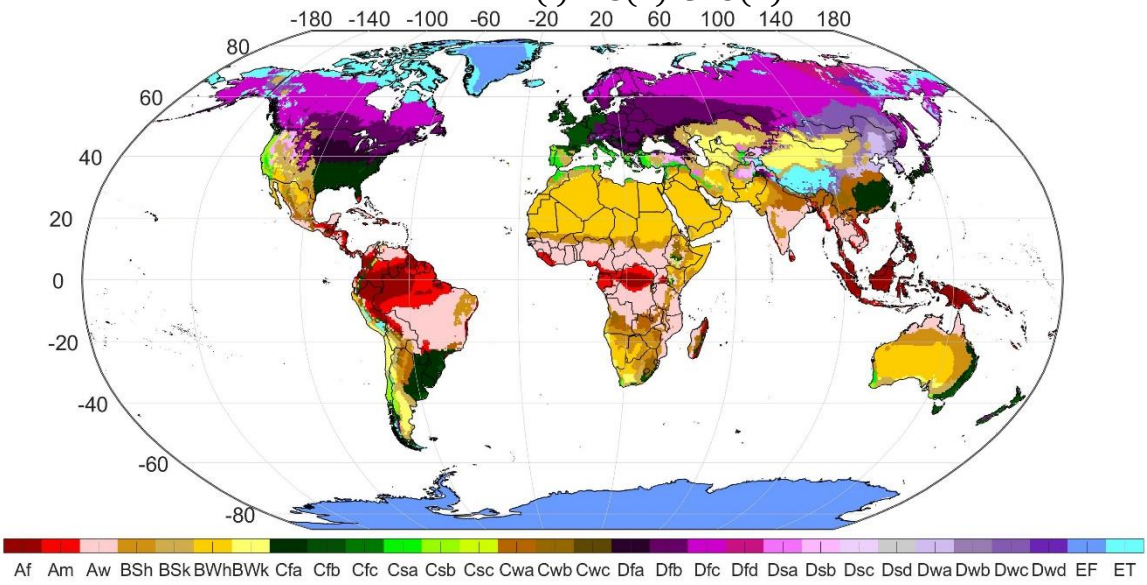

(j) WFDEI (T and P)

Figure 2.9. Köppen-Geiger (KG) world maps at 0.5° resolution for 1980–2017, developed by using precipitation (P) and temperature (T) products: (a) UDEL, (b) CRU, (c) CPC-CRU, (d) GPCC-CRU, (e) NCEP/CFSR, (f) JRA-55, (g) ERA5, (h) MERRA2, (i) MS-CRU, (j) WFDEI.

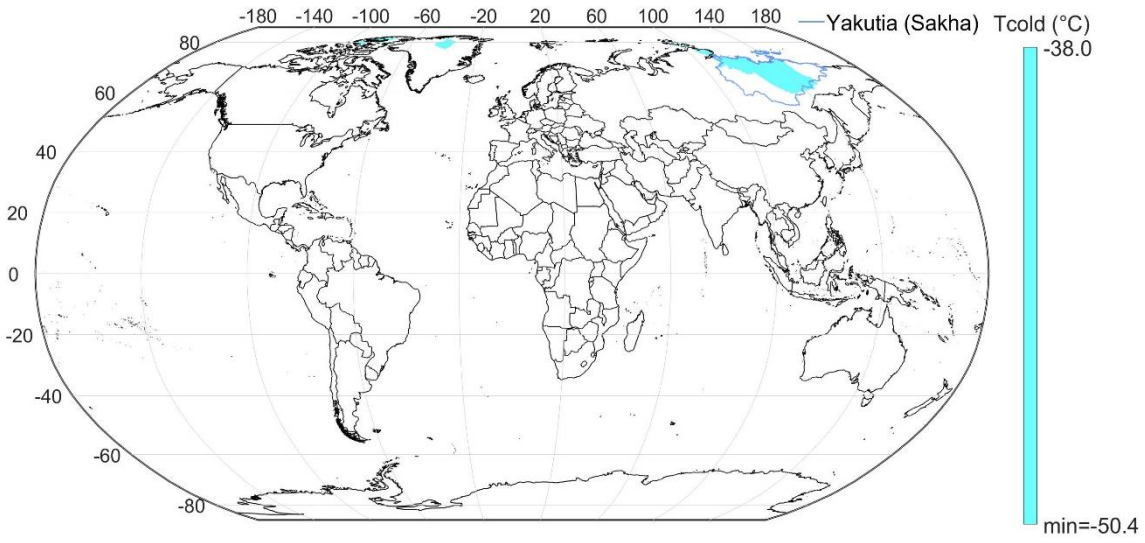

(a) CRU

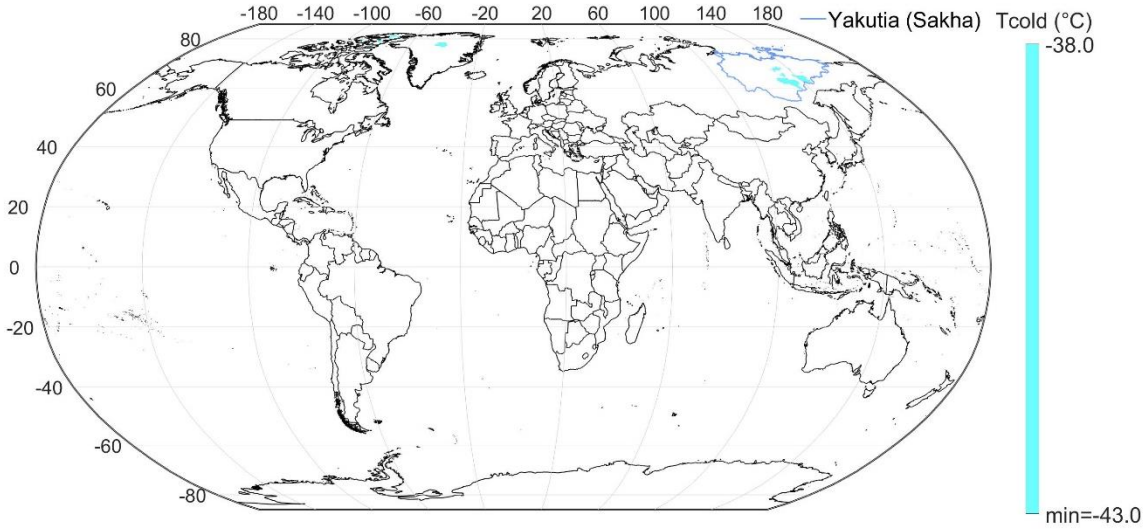

(b) NCEP/CFSR

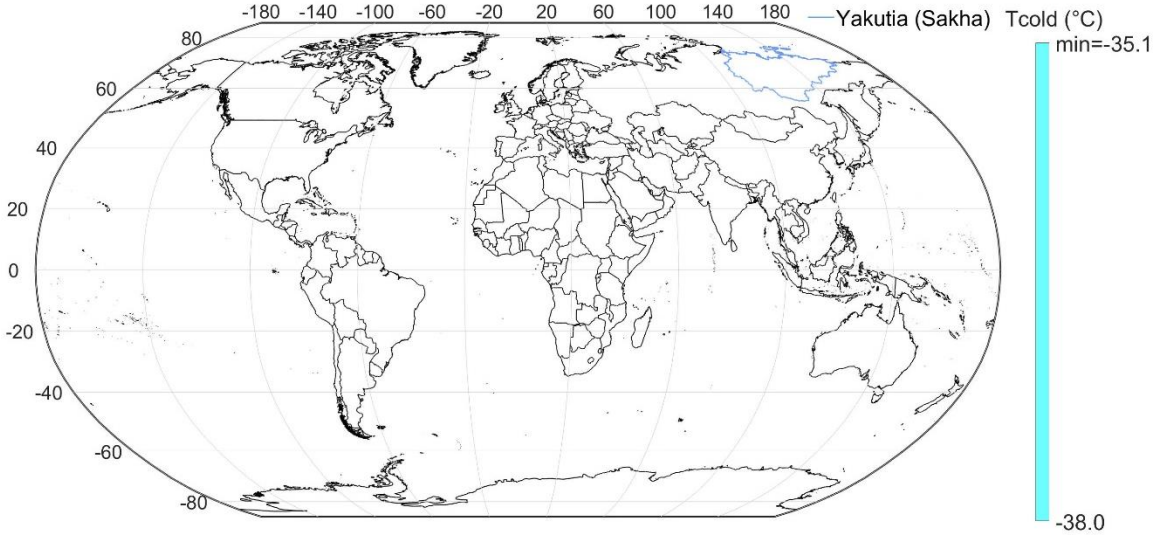

(c) JRA-55

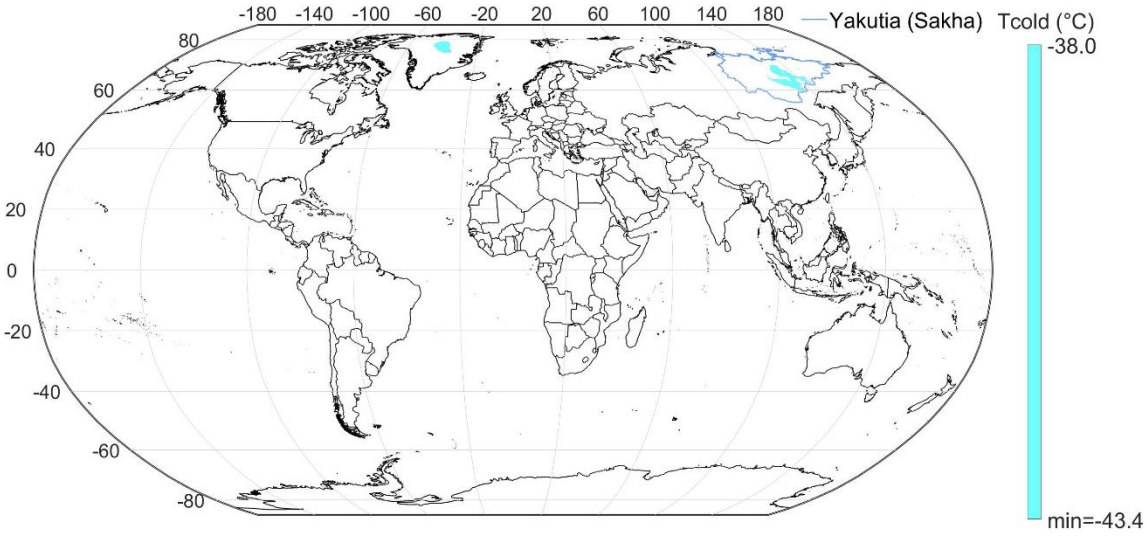

(d) ERA5

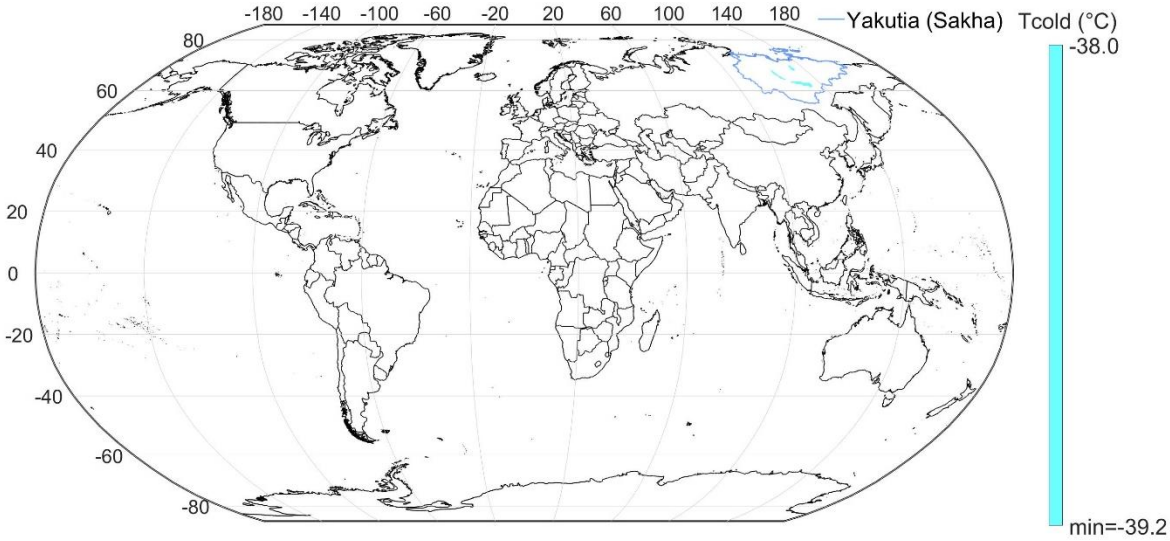

(e) MERRA2

Figure 2.10. T_{cold} maps derived from the following datasets: (a) CRU, (b) NCEP/CFSR, (c) JRA-55, (d) ERA5, (e) MERRA2. Each map shows regions with $T_{\mathrm{cold}}<-38$ ℃ depicting climate subtypes with "d" as the third letter. T_{cold} denotes the air temperature (°C) of the coldest month. Borders of Yakutia (Sakha) are depicted in north-eastern Russia. The study period is from 1980 to 2017.

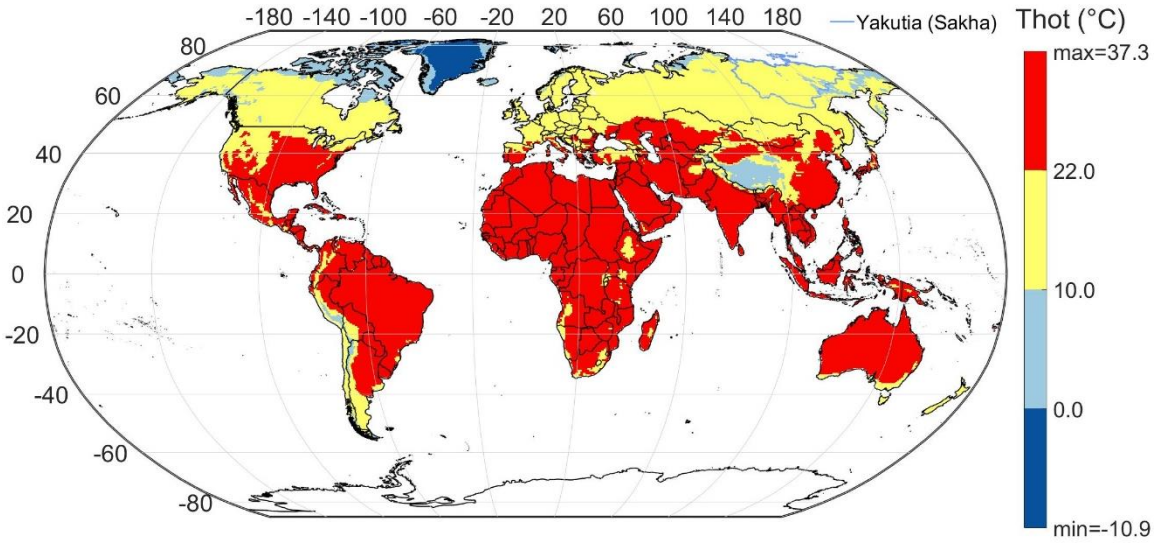

(a) CRU

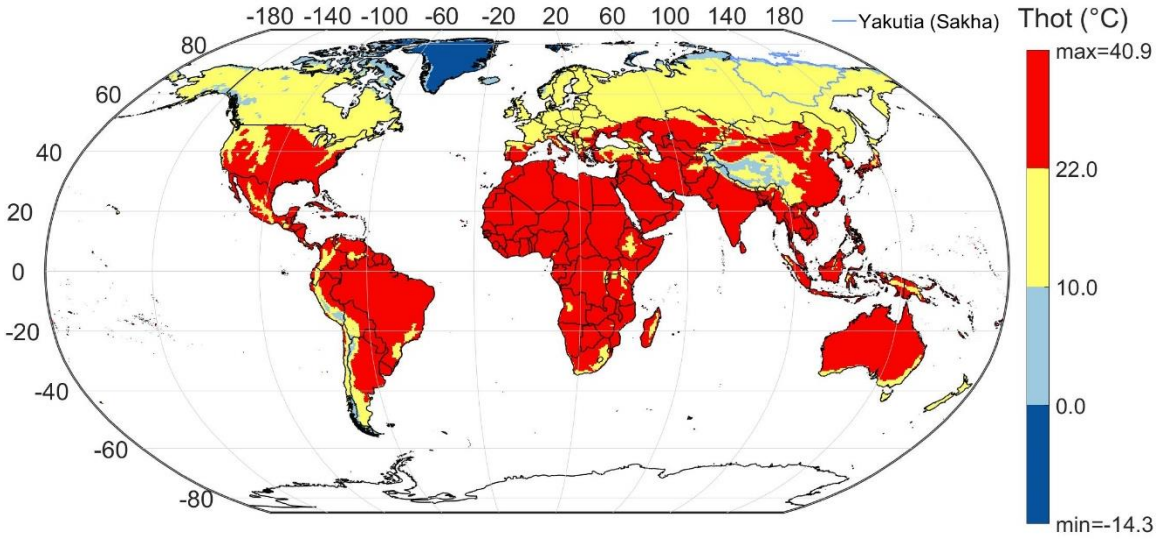

(b) NCEP/CFSR

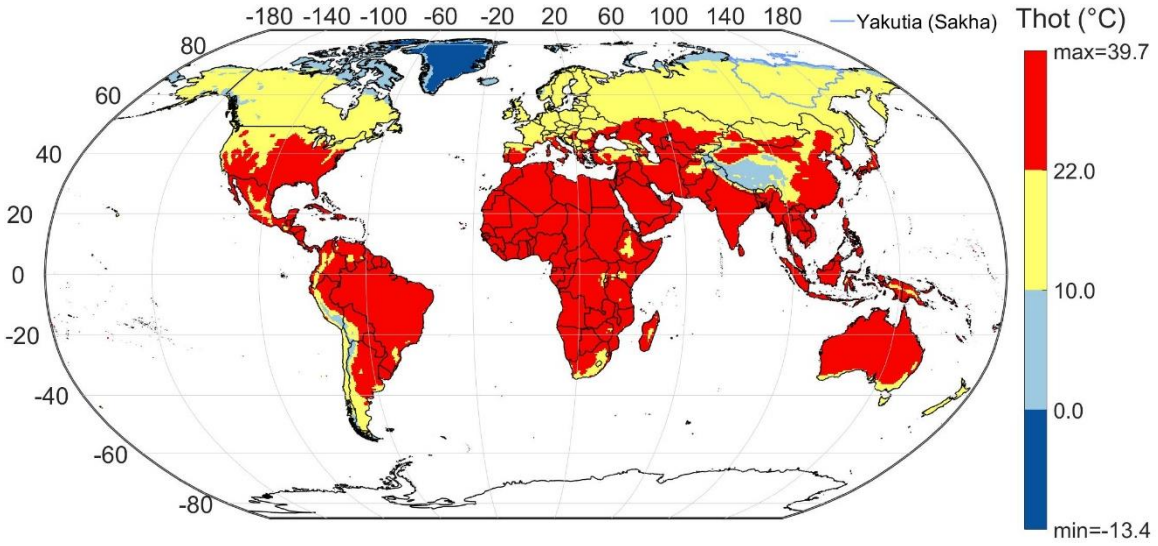

(c) JRA-55

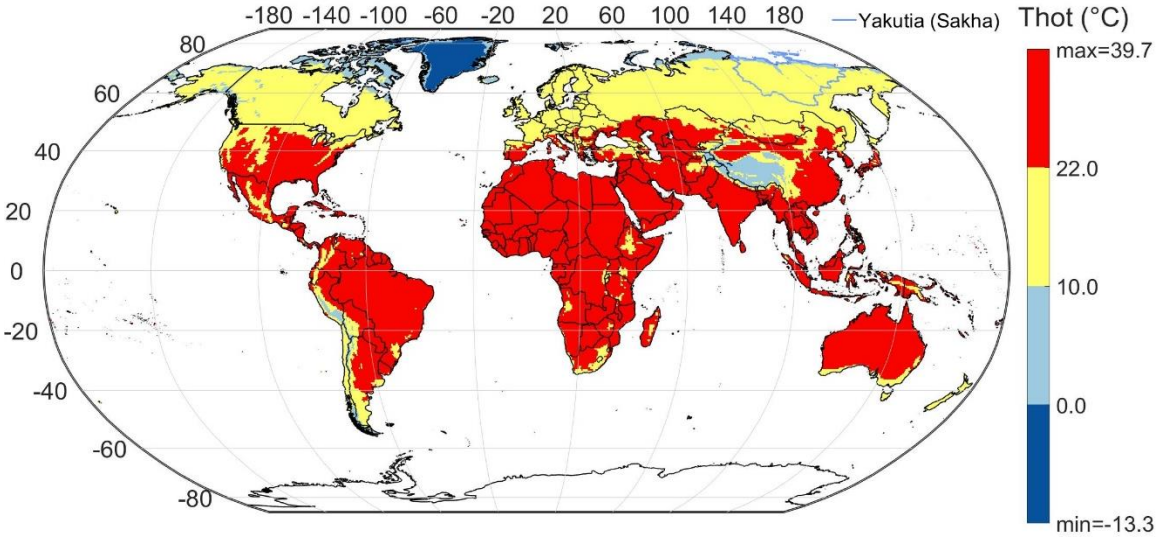

(d) ERA5

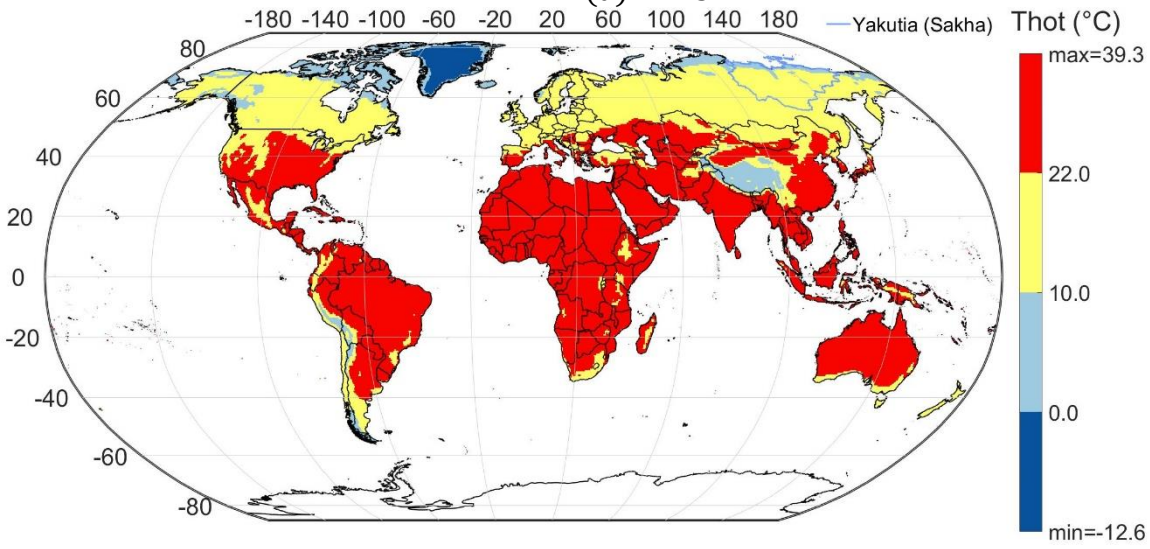

(e) MERRA2

Figure 2.11. T_{hot} maps derived from the following datasets: (a) CRU, (b) NCEP/CFSR, (c) JRA-55, (d) ERA5, (e) MERRA2. Each map shows spatial patterns of T_{hot} within following ranges: [0, 10, 18, 22] or ($T_{\mathrm{hot}} \leq 0, T_{\mathrm{hot}} \geq 0, T_{\mathrm{hot}} \leq 10, T_{\mathrm{hot}} \geq 10, T_{\mathrm{hot}} \geq 22$). T_{hot} denotes the air temperature of the warmest month (°C). The borders of Yakutia (Sakha) are depicted in north-eastern Russia. The study period is from 1980 to 2017.

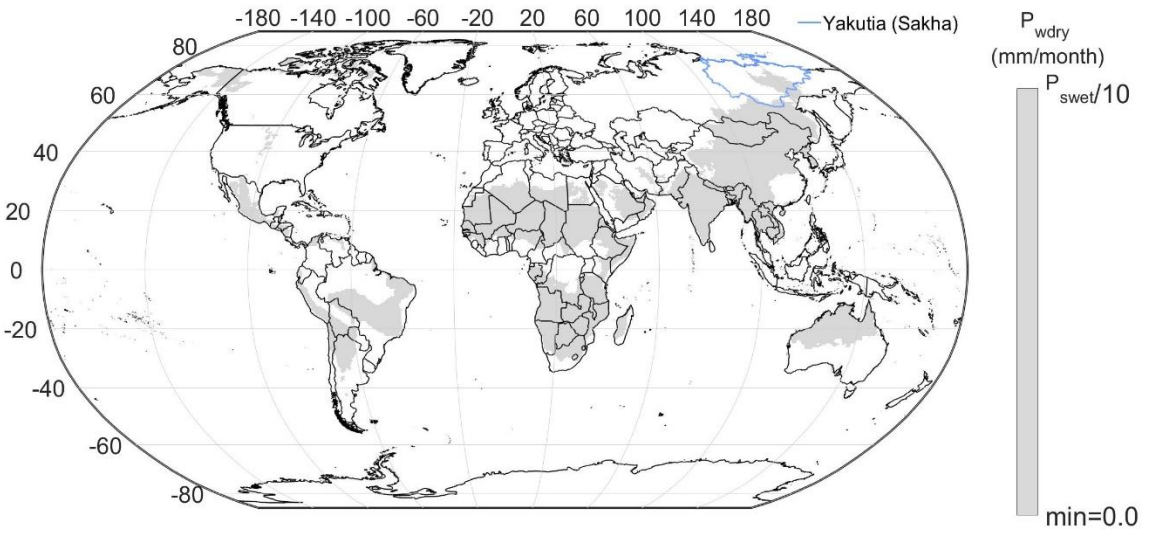

(a) CRU

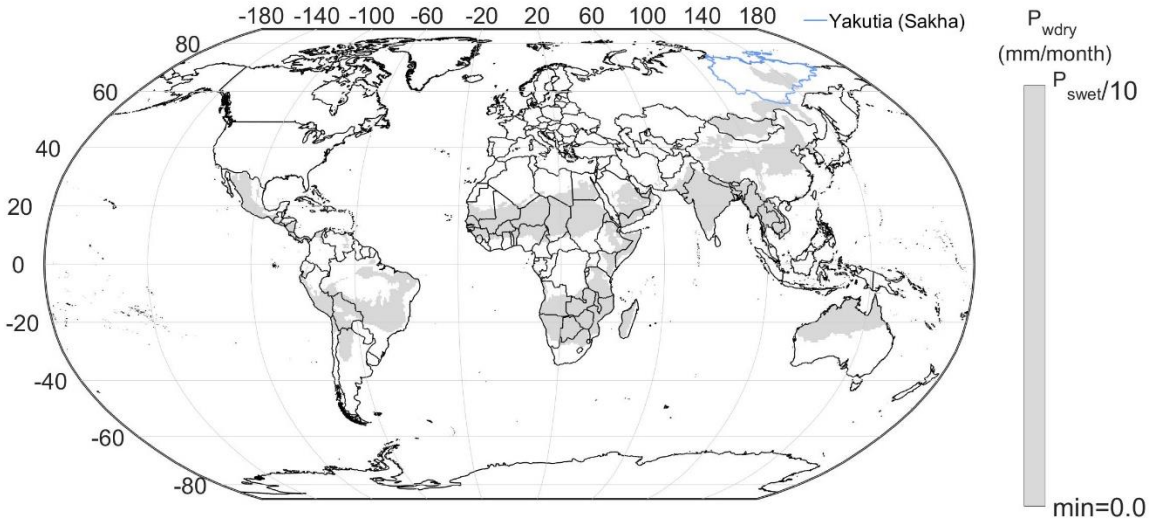

(b) NCEP/CFSR

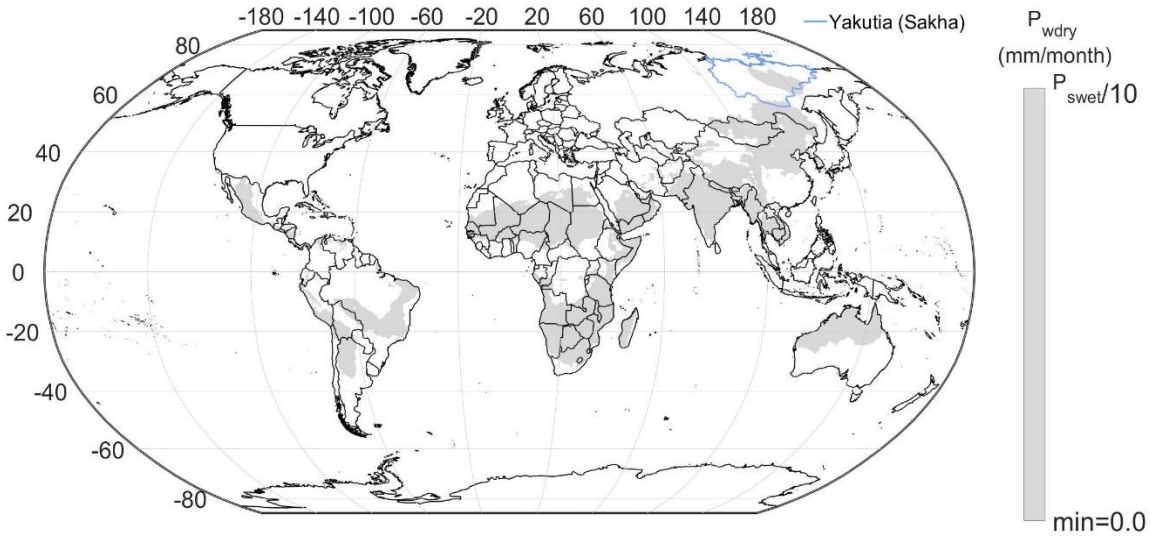

(c) JRA-55

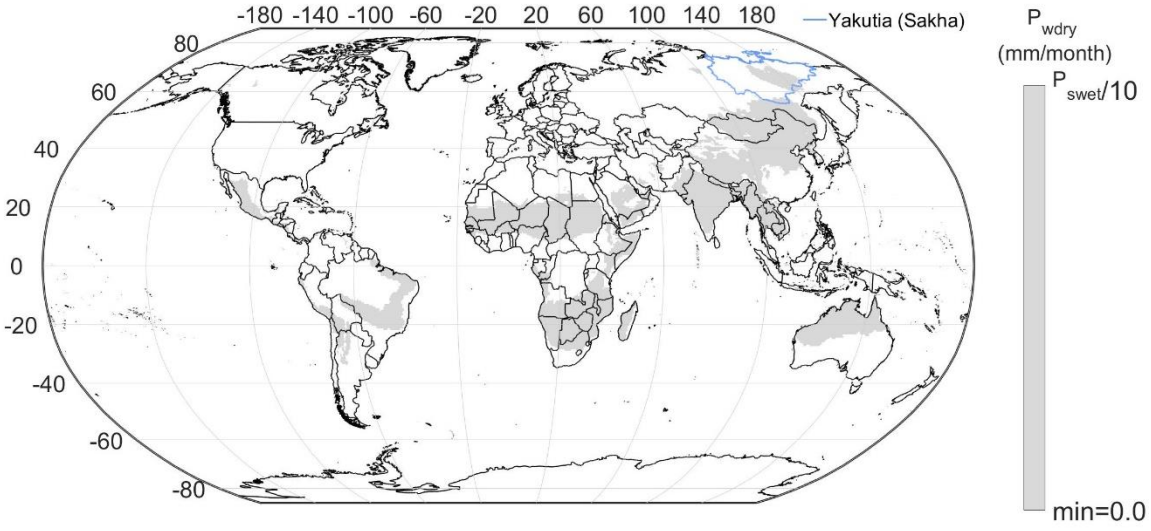

(d) ERA5

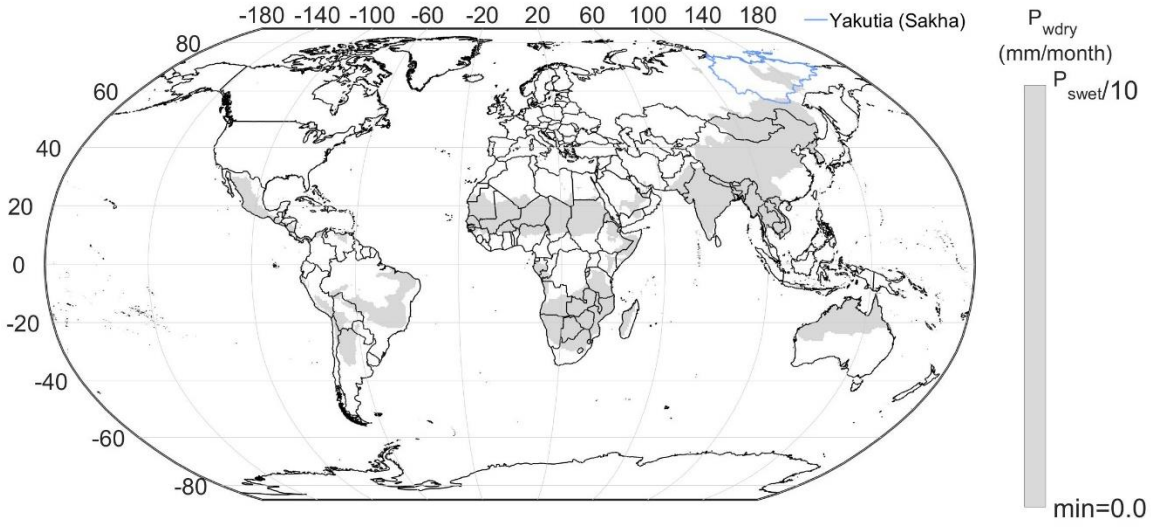

(e) MERRA2

Figure 2.12. P_{wdry} maps derived from following datasets: (a) CRU, (b) NCEP/CFSR, (c) JRA-55, (d) ERA5, (e) MERRA2. Each map show regions covering $P_{\mathrm{wdry}} < P_{\mathrm{swet}}/10$, meeting the precipitation criteria for presenting the Dw climate type. $P_{\mathrm{wdry}}/P_{\mathrm{swet}}$denotes the precipitation of the driest/wettest month in winter/summer (mm/month), respectively. The borders of Yakutia (Sakha) is depicted in north-eastern Russia. The study period is from 1980 to 2017.

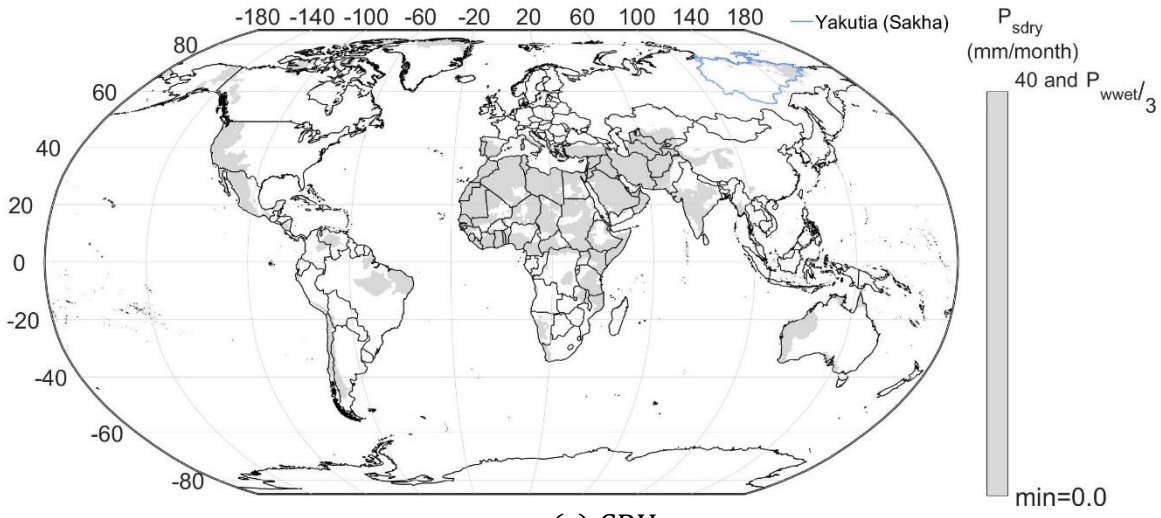

(c) CRU

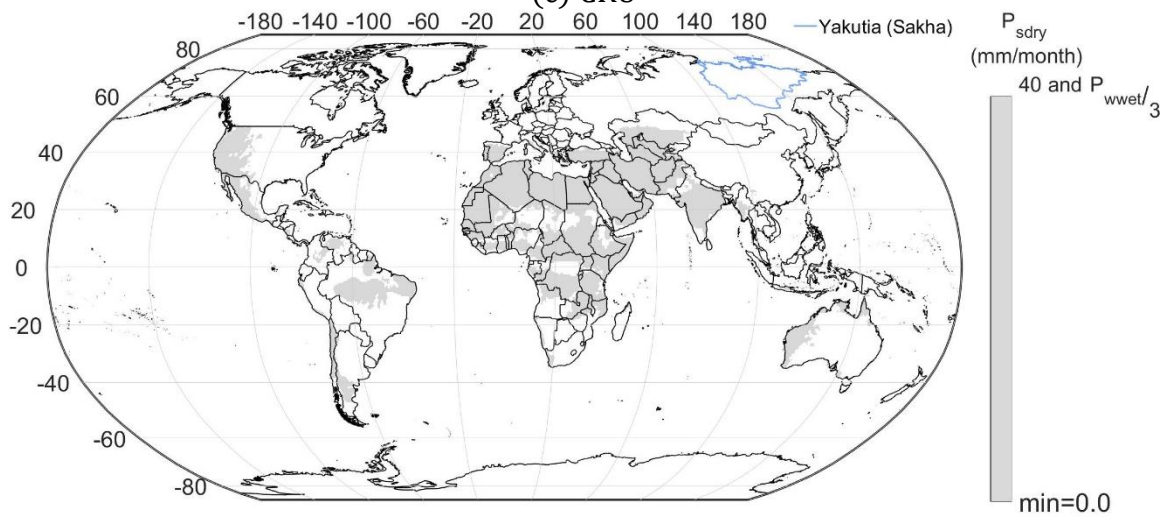

(d) NCEP/CFSR

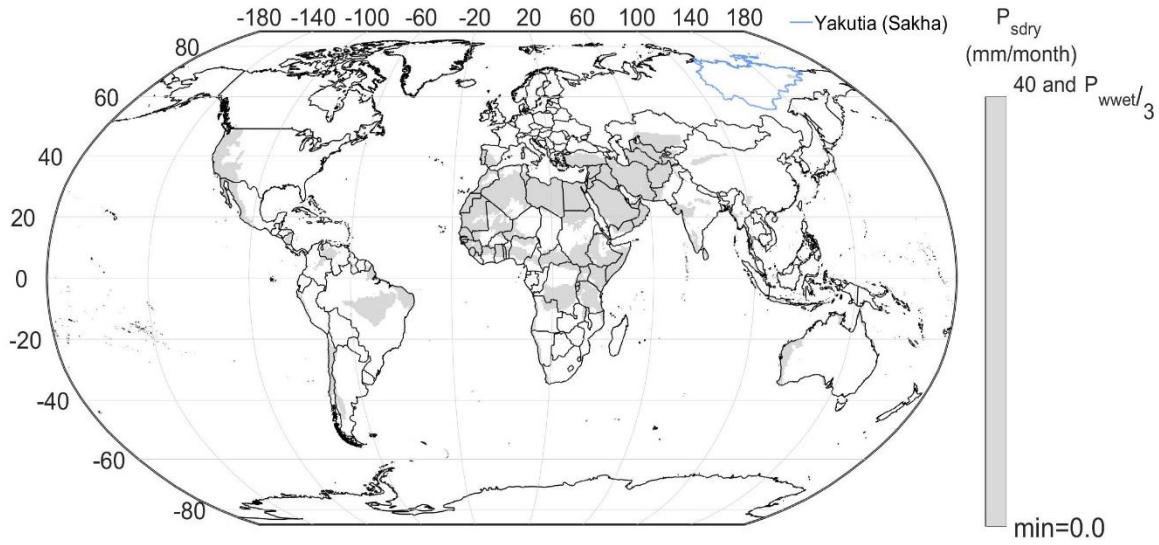

(c) JRA-55

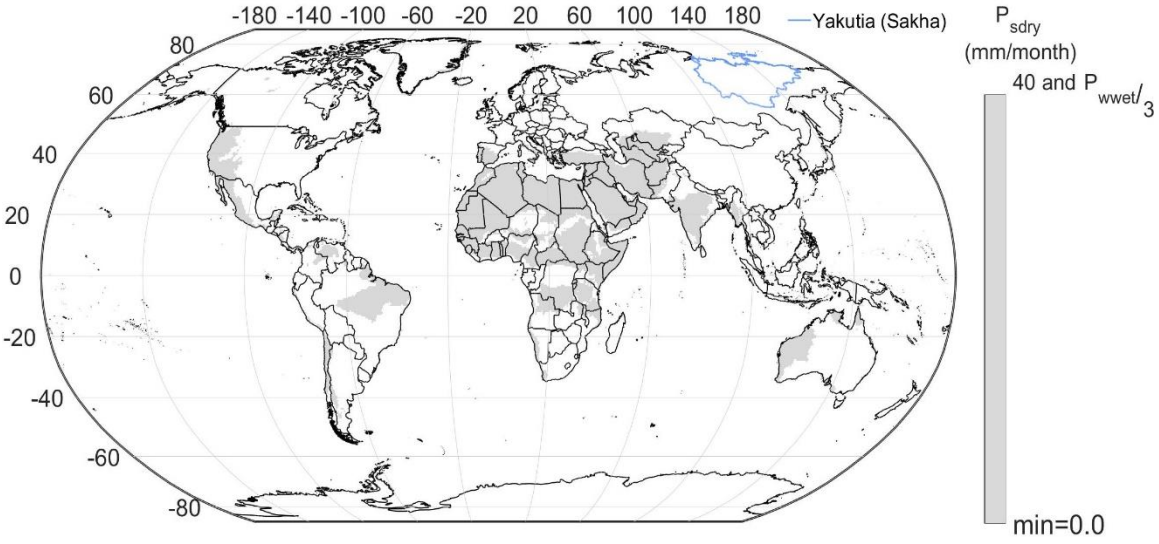

(d) ERA5

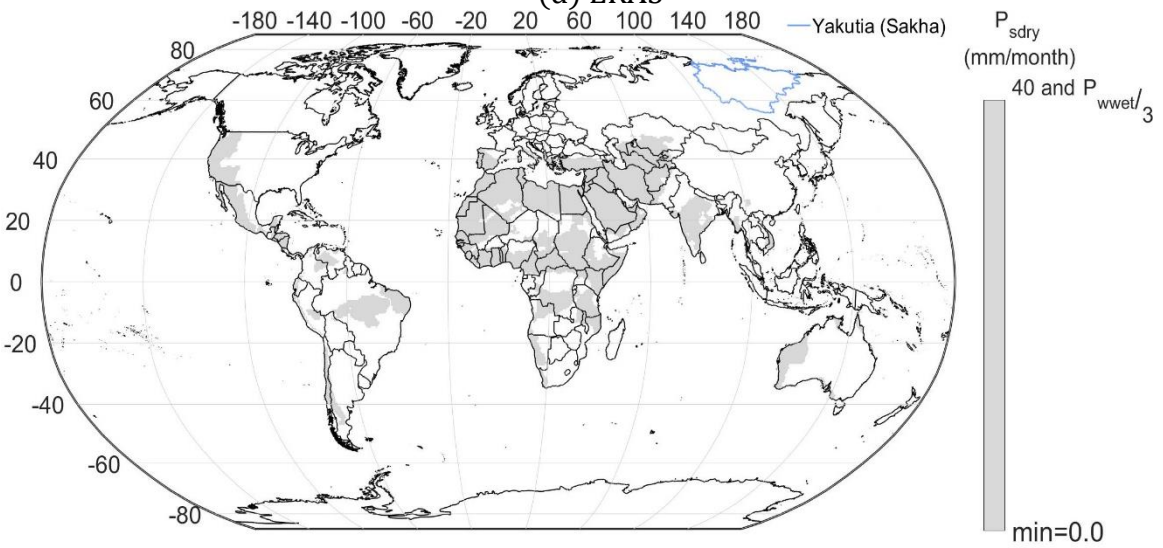

(e) MERRA2

Figure 2.13. P_{sdry} maps derived from following datasets: (a) CRU, (b) NCEP/CFSR, (c) JRA-55, (d) ERA5, (e) MERRA2. Each map show regions covering $P_{\mathrm{sdry}} < 40$ & $P_{\mathrm{sdry}} < P_{\mathrm{wwet}}/3$, meeting the precipitation criteria for presenting the Ds climate type. $P_{\mathrm{sdry}}/P_{\mathrm{wwet}}$denotes the precipitation of the driest/wettest month in summer/winter (mm/month), respectively. The borders of Yakutia (Sakha) are depicted in north-eastern Russia. The study period is from 1980 to 2017.

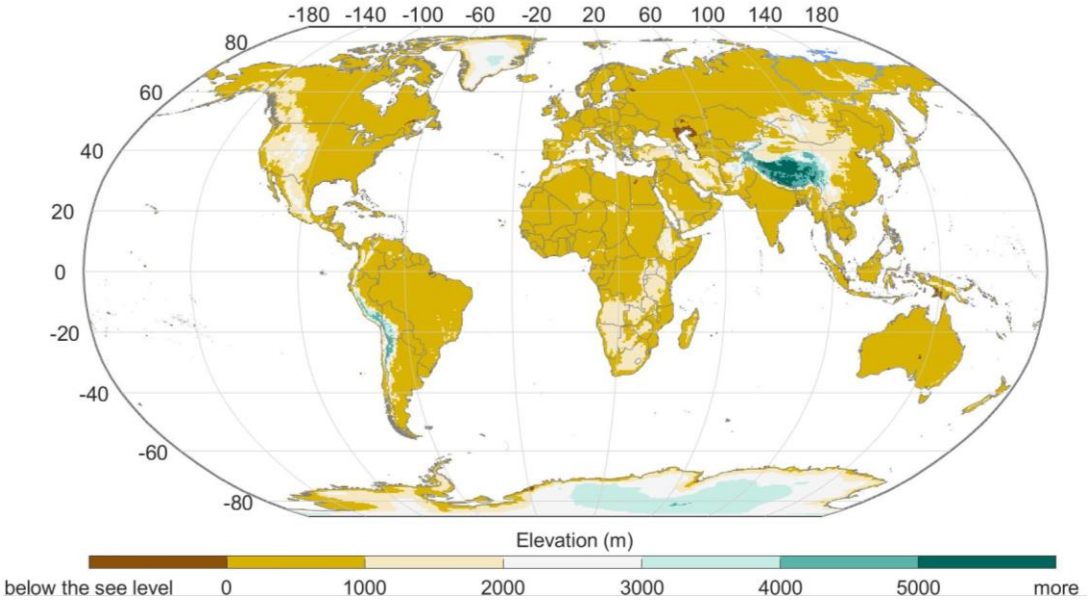

Figure 2.14. Topographic map of terrestrial regions at 0.5° resolution.

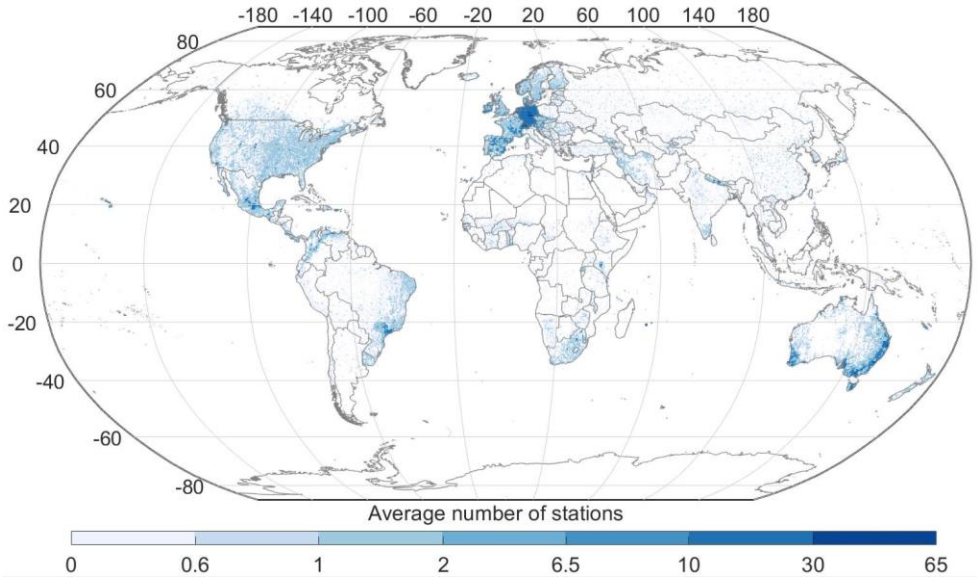

Figure 2.15. Average number of precipitation stations per month from GPCC dataset for 1980–2017.

3. Chapter 3: Extreme precipitation changes in the Köppen-Geiger climate classification

Chapter 3 explores variations among changes in extreme precipitation for different climate types using station rainfall records. In doing so, this chapter analyzes the trends and behaviour of extreme precipitation both for similar and distinct climate types, for the period 1964 to 2013. The Master KG map described in Section 2.4.3 was used as a reference to assign a climate to with each station record. Our analysis indicated the climate types associated with the least frequent and lowest magnitude of extreme precipitation, as well as those associated with the most frequent and highest magnitude. This chapter has not yet been submitted to a journal. Salma Hobbi contributions to this paper are reviewing the relevant literature, gathering and analysing the data, analysing the test results, and writing the manuscript under the supervision of Dr. Simon Michael Papalexiou.

Abstract

Changes in the frequency and intensity of extreme precipitation, the two most critical aspects of climate change, trigger natural disasters such as severe floods. Changes in extreme precipitation have been investigated using different sources of precipitation and applying different methods to examine trends of annual maxima precipitation at global and regional scales. However, little is known about how extreme precipitation trends change among different climate types. This chapter offers global analysis of extreme precipitation changes in terms of climate type over 8582 daily station records, focusing on 1964 to 2013 when global warming was accelerating. A climate type is assigned to each station based on a robust KG climate classification map; then, annual maxima time series of precipitation at each station were classified into 30 KG climate subtypes. By applying non-parametric tests of Mann-Kendall and Sen's slope estimator at each time series, the magnitude and significance of trends were measured. Also, extreme value analysis was used to measure the heaviness of the tail for each time series. Our results showed a decreasing trend over the majority of stations associated with BSh, Csa, Csb and Dsb, while an increasing trend was shown for the stations associated with the remaining KG subtypes (especially in all stations associated with Dsc and Dwd). Results indicate significant increasing trend in 9.7% of stations in the eastern USA, Asia, and northern Europe. However,

only 2% of stations in eastern Australia and central USA had a significant decreasing trend. Largest to smallest heavy-tailed extremes in major climate types E, A, B, D, and C. For climate subtypes, large heavy-tailed extremes were observed in Dfd, ET, and Am, while only light-tailed extremes were observed in Cfc. Stations associated with the Dfd climate subtype had the most frequent and largest magnitudes of extreme precipitation, whereas Cfc had the least frequent and smallest magnitudes.

3.1 Introduction

Climate extremes such as extreme precipitation and temperature impacts human life and society in many critical ways. Most critical impacts of extreme temperature are represented by heatwaves and droughts, imposing detrimental effects on human health and agriculture (Barrett et al., 2015; Mohammat et al., 2013; Wreford & Adger, 2010). Storms and heavy rain can affect traffic conditions and damage infrastructure, such as bridges and overpasses (Behrisch & Weber, 2019; Liu et al., 2021; Pregnolato et al., 2017; Sohn, 2006). During extreme rainfall, microbes can contaminate runoff and interfere with sewage and water treatment plants, leading to waterborne illnesses (Parker et al., 2010). Heavy rain and hail can also damage terrestrial ecosystems, harm crops, and cause landslides. The most critical impact of extreme precipitation is flooding, both in coastal communities, where sea levels are rising, and in urban areas, where surfaces are impervious (e.g., Wdowinski et al., 2016). Several studies have found that the frequency and intensity of precipitation extremes are affected by climate change and have studied global patterns of extreme precipitation changes (Donat et al., 2016a; Karl, 2003; Trenberth et al., 2007; Richter, Wentz, Fowler and Hennesy). Extreme precipitation could be related to climate type, with certain climate types more susceptible to it than others. However, little research has investigated how extreme precipitation differs according to climate type at the global scale.

Changes in precipitation extremes depend on the source of precipitation data (e.g., observation datasets, gridded products, and climate models) and methods to measure extreme precipitation. Several global studies have used observation data sets. For example, Groisman et al. (2005) reported that, in the past 50 to 100 years, the number of extreme precipitation events has increased substantially in the mid-latitudes, particularly over North America. By applying non-stationary generalized extreme value analysis, Westra et al.

(2013) determined the annual maximum daily precipitation and near-surface temperature. Papalexiou and Montanari (2019) observed a coherent spatial pattern of considerable frequency changes in Eurasia, the mid-western United States, and North Australia, finding that from 2003 to 2013 there were 7% more extreme precipitation events than events under the stationarity assumption. Although different methods, records, and study periods were used by Papalexiou and Montanari (2019) and Westra et al. (2013), they indicated a higher number of extreme global precipitation events compared to the expected number of these events under stationarity.

Other global studies have used gridded products or climate models. Using extreme climate data from the Hadley Centre global land-based gridded climate extremes dataset (HadEX), Alexander et al. (2006) revealed increasing changes of extreme precipitation over the United States and Eurasia. In similar research using climate models, Fowler and Hennessy (1995) demonstrated that the frequency and magnitude of extreme daily precipitation increased significantly from 1909 to 1986, with an augmented effect in longer return periods. Min et al. (2011) demonstrated that the annual maximum daily precipitation in 65% of global land coverage increased from 1951 to 1999. In a study of the periods 1980 to 1999 and 2080 to 2099, Martel et al. (2020) indicated an increase in the frequency of future extreme events. They also found a corresponding reduction in the return period of extreme events for all tested spatial resolutions and temporal scales. No matter the method or data used, most studies have shown that both the intensity and frequency of extreme precipitation have increased over the past 50 years. However, it is important to know the variation of global extreme precipitation trends in areas of similar and different climate types.

In addition to global studies, regional studies have shown increases in extreme precipitation over time and into the future. In eastern Asia, for example, an increase in intense precipitation has been observed in China, Inner Mongolia, and South Korea(Kim et al., 2009). In a study of central China from 1961 to 2001, using observations, Wang (2005) found that the annual mean precipitation increased substantially in the east (mainly in the summer), northwest (in all seasons), and southwest, but fell in the north and northeast (in the spring and fall). Another study of China (Ying et al., 2020) used climate models to investigate the impact of extreme climatic indices on end-of-season

(EOS) values in Inner Mongolia. Interestingly, the authors indicated that EOS changes were less affected by extreme precipitation than by temperature indices. They also observed a significant decreasing trend for minimum one-day precipitation (Rx1day) and minimum five-day precipitation (Rx5day) from 1982 to 2015. Kim et al. (2009) applied a Bayesian technique to show that the intensity and frequency of extreme precipitation in South Korea increased sharply in 1997. Over central India, Goswami et al. (2006) showed an increasing trend in both the magnitude and frequency of extreme precipitation, likely to result in severe property damage in the future. In a study of the Aguascalientes State in Mexico, Ruiz-Alvarez et al. (2020) showed a notable increasing trend in (1) the number of days with extreme precipitation and extremely wet days, and (2) the maximum one-day and five-day precipitation amounts and the number of days with extreme precipitation.

Similar research results have been found in the Middle East. Evans (2009) used simulations of future projections of 18 global climate models proposed by Alley et al. (2007) to show changes of maximum precipitation in the Middle East in the 21st century. Evans showed that the total precipitation in Northeastern Iran, the Eastern Mediterranean, Turkey, Syria, and Northern Iraq will experience a downward trend. They indicated that late in the century, the cropping strategy or crop types in Northeastern Iran will have to change because the dry season will be extended, resulting in significant changes in the timing of maximum precipitation.

Similar increasing trends have been observed in regional studies of Europe. Pujol et al. (2007) observed substantial increases of maximum precipitation from 1955 to 2004 in April in the Mediterranean region of France and depicted a descending trend in March over the rest of France. Fowler and Kilsby (2003) found substantial changes in extreme precipitation every decade from 1961 to 2000 in parts of the UK. Studies of Italy have revealed that extreme precipitation events there have risen, especially for short durations over the past 20 years (Forestieri et al., 2018; Saidi et al., 2015). Achberger and Chen (2006) indicated a strong association between precipitation amounts and extremes in Norway. The highest average precipitation and greatest number both of days with extreme precipitation and of rainy days occurred in the southern part of Norway's west coast. In a study of Germany, Hundecha and Bárdossy

(2005) showed an increasing trend in both the intensity and magnitude of daily extreme precipitation in all seasons except the summer since 1958.

Studies of precipitation trends in North America have had interesting, sometimes conflicting, results. Kunkel (2003) found an increasing trend in the magnitude and intensity of extreme precipitation since the 1920s over the United States but no long-term increasing trend detected in Canada. However, in a similar study over Canada, from 1950 to 2010, Tan et al. (2017) observed an increasing trend in annual maximum precipitation in most regions, including the central Boreal region and Pacific maritime and a decreasing trend in the remaining Boreal regions and the Canadian Prairies. Likewise over Canada, using the Canadian Global Climate Model (CGCM3), Mailhot et al. (2010) evaluated the simulation results for one- to five-day AMP events from 1850 to 2100. They detected a stationary trend for extreme precipitation in daily and multi-day intensity between 1850 and 1980. However, more intense and frequent daily and multi-daily precipitation events were discovered in the 1980 to 2005 period and noted across Canada (excluding the Canadian Prairies). Despite the plethora of regional studies on extreme precipitation, few have investigated how extreme regional precipitation changes when the climate type changes.

Studies using Köppen-Geiger's climate classification offer analysis on extreme precipitation changes based on the specific climate types in different regions. Major climate groups are classified as tropical (A), dry (B), mild temperate (C), snow (D), and polar (E). Using this system, researchers have investigated changes at a longer timescale to determine differences in climate variables (temperature, precipitation, etc.) according to climate type (Chen & Chen, 2013; de Sá Júnior et al., 2012; H.-J. Kim et al., 2008; Sarfaraz et al., 2014; Yun et al., 2012). They showed an increase in precipitation over the subtropical climate in Korea (Yun et al., 2012), expansion in the desert-arid (BWh) climate type along with decreases in the arctic climate (EF) across the globe (Chen and Chen, 2013). In Pakistan, the highest and lowest total levels of precipitation were seen across the northern and southern regions (climate types B and D: 1500-2000 mm for the north and 100-200 mm for the south)(Sarfaraz et al., 2014). Studies have shown that countries such as France, Norway, Germany, Sweden, and the United Kingdom with the temperate oceanic climate (Cfb) climate

type have experienced an increasing trend in both intensity and magnitude of daily extreme precipitation. Other countries with the climate type of warm desert (BWh), such as in the Middle East, have experienced a decreasing trend in total precipitation (Evans, 2009).

Most of the studies using Köppen-Geiger's climate classification to study extreme precipitation have been regional in scope, e.g., Brazil (de Sá Júnior et al., 2012), Pakistan (Sarfaraz et al., 2014), and North Korea (Kim et al., 2008). Little global analysis of extreme precipitation has been conducted based on climate type. This chapter offers the first global analysis and comparisons of degrees of difference in extreme precipitation in terms of different climate types. This study provides new insights into differences in precipitation trends in areas with the same and distinct climate types across the globe. This analysis will help scientists to understand the relationship between climate type and changes in extreme precipitation.

3.2 Data

This study used global records on daily rainfall from the Global Historical Climatology Network-Daily (GHCN-D) database (version 2.60, https://www.ncdc.noaa.gov/ghcn-daily-description, for more detail about how data was acquired data, see Appendix). With more than 100000 records, the database had many records that either contained unreliable data or were too short. To address these issues, the following selection criteria are used: (1) records must be at least 50 years in length, (2) they must be missing no more than 20% of their values, and (3) their data must have less than 1% quality flags assigned to them (for these flags, see the above-mentioned website). Once the records were selected, those marked with flags of "X" (failed bounds check) and "G" (failed gap check) were eliminated as they signified that precipitation values were unusually large. To guarantee that information coverage from 1964 to 2013 was adequate, records with at least five complete years in each decade were chosen (Papalexiou & Koutsoyiannis, 2013). Here, this period is selected for two reasons: (1) this period has more station records than any other, and (2) it shows a clear acceleration of global warming. Years from 2014 to 2020 were excluded because starting in 2014 there were far fewer stations in operation. Lastly, for a year to be "complete" (completeness≥ 91.8%) and used in the analysis, no more than 30 missing daily values were required. Approved for analysis is a set of records from 8582 stations around the globe. Over

the records' history, observation times might have changed in some stations, creating frequent discretization errors. These errors could theoretically alter the magnitude and frequency of daily extremes but are unlikely to significantly affect our results.

3.3 Köppen-Geiger climate classification

The Köppen-Geiger (KG) climate classification divides the climate into different categories based on monthly near-surface temperature and precipitation. The categories appear as groups of letters. The five major categories of climate type are represented by the upper-case letters A, B, C, D, and E. They are further divided into 30 subtypes based on differences in patterns of precipitation, represented in a second letter, and patterns of temperature, represented in a third letter (except for major climate group E). The major climate types and subtypes and their main characteristics are presented in Table 3.1. The most frequent KG climate subtypes derived from merging the precipitation and temperature from ten different sources are shown in Figure 3.1a (for more information see Section 2.4.3)

By using the spatial pattern of KG climate subtypes presented in Figure 3.1a, a climate subtype is assigned to each station (see Figure 3.1b); however, five climate subtypes—Csc, Cwc, Dsa, Dsd, Ef—were not assigned because of the absence of stations in the regions where they are found. Of the major climate groups, a large proportion (40%) of stations were assigned to major climate type C, 80% of which were assigned to the subtypes Cfa (45%) and Cfb (34%). The second highest proportion of stations were assigned to major climate D, with the most common climate subtype Dfb (40%). Nearly 22% of stations were assigned to major climate type B, and more than 55% of these stations to climate subtype BSk. However, less than 5% of total stations were assigned each of the major climate types A (Af, Am, Aw) and E (ET). More than 60% of stations were located in the northern hemisphere and are mostly distributed in the United States of America (USA), Russia, Europe; however, Australia had the vast majority of total stations (90%) in the southern hemisphere. Among available stations, no stations were observed in the Middle East, Central and northern Africa, South America, or Antarctica.

Table 3.1. Main characteristics of the Köppen-Geiger climate classification

Major climate type		Climate subtypes	
Name	Characteristics	Name	Characteristics
A	Tropical	Af	Tropical rain forest
		Am	Tropical monsoon
		Aw	Tropical savannah with dry winter
B	Dry climate	BWh, BWk	Desert (arid)
		BSh, BSk	Steppe (semi-arid)
C	Mild temperate	Csa,Csb,Csc	Mediterranean
		Cfa, Cwa	Humid subtropical
		Cfb, Cfc, Cwb, Cwc	Oceanic
D	Snow	Dfa, Dfb, Dsa, Dsb, Dwa,Dwb	Humid
		Dfc, Dfd, Dsc, Dsd, Dwc. Dwd	Subarctic
E	Polar	ET	Tundra
		EF	Ice cap

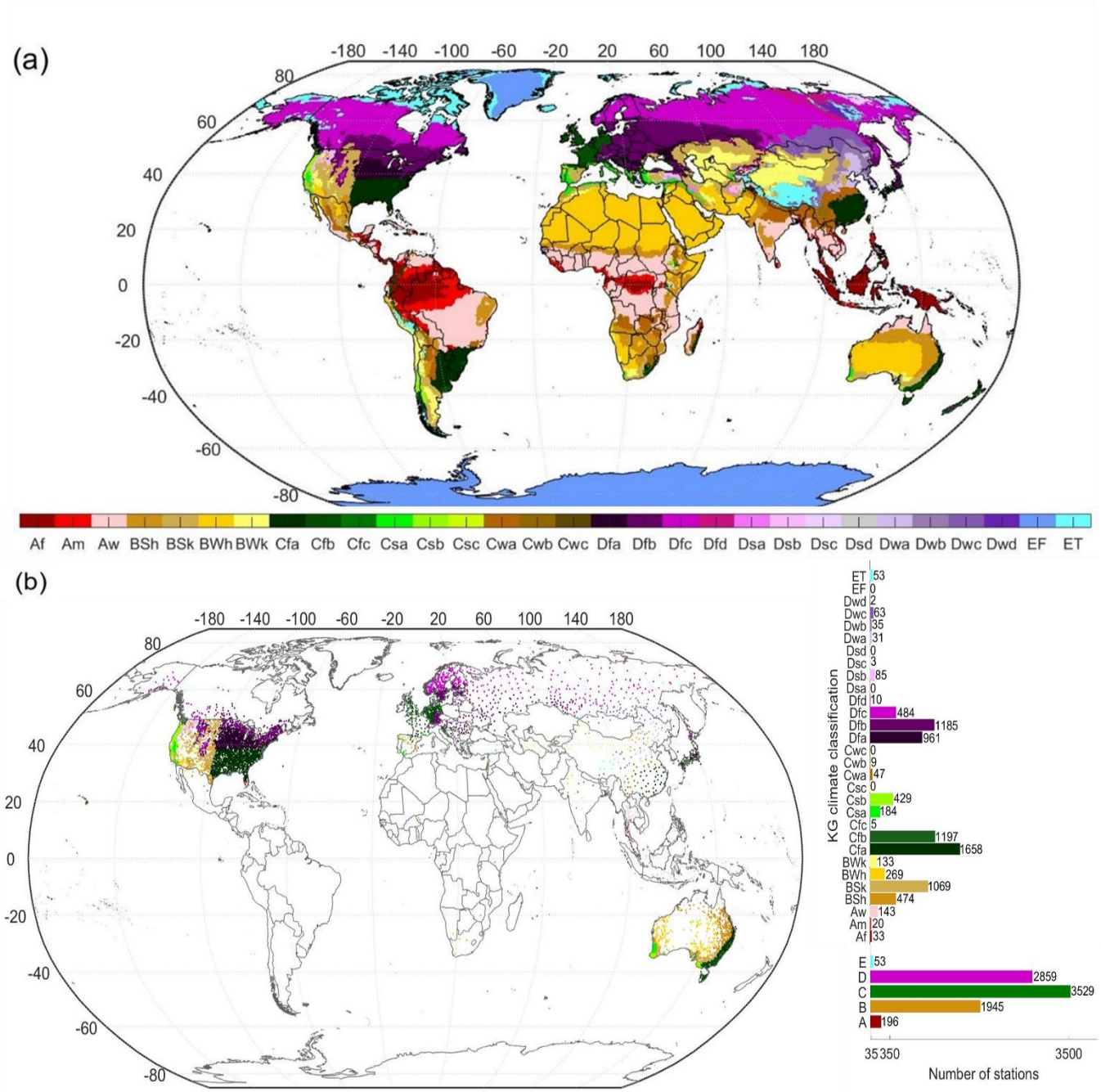

Figure 3.1. KG climate classification: (a) Robust KG classification map presented in Section 2.4.3, (b) the available stations and their climate type from 1964 to 2013.

3.4 Methodology

In this study, annual maxima time series of precipitation (AMP) were formed at each station for the study period by extracting each year's maximum, regardless of the year's missing value percentage, which has been set at less than 20%. Then, the behaviour of the

AMP time series were analysed by measuring their trend, as well as the heaviness of their tail.

3.4.1 Trend analysis methods

There are two categories of tests—non-parametric and parametric— to evaluate the trends in meteorological variables' time series (e.g., precipitation). Both tests evaluate independent data trends, but parametric tests also need data that are normally distributed. Here, the Sen's slope estimator was used to assess the trend's slope and the non-parametric Mann-Kendall test to assess its significance. Annual maxima values are typically independent and not normally distributed.

3.4.2 Sen's slope estimator

Sen (1968) developed a non-parametric trend test based on Kendall's rank correlation coefficient. Sen's slope estimator has been widely used to measure the trends in climatological time series (Gocic & Trajkovic, 2013; Lettenmaier et al., 1994; Tabari & Marofi, 2011; Yunling & Yiping, 2005). This test calculates the slope of T pair of data as follows:

$$Q_i = \frac{x_i - x_j}{j - k} \text{ for } i = 1,2,3, \ldots, T \qquad \text{(Eq 3.1)}$$

where $x_i$and x_j are data values at times j and k, where $(j > k)$. Then, Sen's slope is the median of the slope when T values of Q_i are sorted from the smallest to largest.

$$Q_{median} = \begin{cases} Q_{[(T+1)/2]} & N \text{ is odd} \\ \dfrac{Q_{[T/2]} + Q_{[(T+2)/2]}}{2} & N \text{ is even} \end{cases} \qquad \text{(Eq 3.2)}$$

The value of Q_{median} reveals the steepness of the trend, while its sign (positive or negative) reveals the reflection of the trend.

3.4.3 Mann-Kendall test

The Mann-Kendall (Kendall and Gibbons, 1975; Mann, 1945).test has been applied to time series of hydrological data to measure the significance of trends in extreme precipitation and temperature events (Alexander & Arblaster, 2009; Gocic & Trajkovic, 2013; Westra et al., 2013). Here, the Mann-Kendall test was applied to measure the

significance of trends in AMP time series at each station. The variables $p_i$and p_j are the precipitation values in each time series at time i and j ($j > i$), n being the number of years in each time series (50 years, study period: 1964–2013). Then, S, the Mann-Kendall test statistics (Kendall & Gibbons, 1975; Mann, 1945), is calculated as follows:

$$S = \sum_{i=1}^{t-1} \sum_{j=i+1}^{t} sgn(p_j - p_i), \quad \text{(Eq 3.3)}$$

Where $sgn(p_j - p_i)$ shows the sign as:

$$sgn(p_j - p_i) = \begin{cases} +1, \text{if } p_j - p_i > 0 \\ 0, \text{if } p_j - p_i = 0 \\ -1, \text{if } p_j - p_i < 0 \end{cases} \quad \text{(Eq 3.4)}$$

And variance of the statistic test is computed as:

$$\sigma^2(S) = \frac{n(n-1)(2n+5) - \sum_{i=1}^{m} p_i(p_i-1)(2p_i+5)}{18} \quad \text{(Eq 3.5)}$$

Where n is the number of data in each time series, m is the number of tied groups, and t_i is the number of p_i in the ith tied group. Note that the tied group is the set of sample data that contains the identical values. When the following Z-transformation is applied, the statistic S is approximately normally distributed:

$$Z = \begin{cases} \frac{S-1}{\sigma} \; if \; S > 0 \\ 0 \quad if \; S = 0 \\ \frac{S+1}{\sigma}, if \; S < 0 \end{cases} \quad \text{(Eq 3.6)}$$

Positive/negative values of Z indicate an increasing/decreasing trend in the time series. At a 5% level of significance (α =0.05), the null hypothesis H_0 is rejected when $Z > Z_{1-\frac{\alpha}{2}}$, which indicates a significant trend in the time series.

3.4.4 Extreme value theory

Extreme value theory (EVT) describes the behavior of very large and small values of a distribution (Gumbel, 1958; Leadbetter et al. 1984). In this theory, random variable X follows the distribution of $F_X(x)$ and the cumulative distribution function (cdf) of maximum values of the random sample $Y_n = \{X_1, X_2, \dots, X_n\}$ follows the distribution of:

$$G(x) = (F_X(x))^n \quad \text{(Eq 3.7)}$$

If $n \to \infty$ then $G(x)$ emerges in any of the following distributions: (1) the Fréchet, (2) the Gumbel, or (3) the reversed Weibull distributions (more detailed information in Papalexiou & Koutsoyiannis, 2013). These three can be unified in one single distribution (Jenkinson, 1955; Von Mises, 1954) known as the Generalized Extreme Value Distribution ($\mathcal{GEV}$):

$$F_{\mathcal{GEV}}(x) = \exp\left(-\left(1 + \gamma\frac{x - \alpha}{\beta}\right)^{-1/\gamma}\right), 1 + \gamma\frac{(x - \alpha)}{\beta} \geq 0 \quad \text{(Eq 3.8)}$$

where the location parameter is $\alpha \in \mathbb{R}$, the scale parameter is $\beta > 0$, and the shape parameter is $\gamma \in \mathbb{R}$. If $\gamma > 0$, a heavy-tailed Fréchet distribution is bounded from below $x \geq \alpha - \beta/\gamma$. If < 0, a short-tailed reverse (or negative) Weibull distribution is bounded from above $x \leq \alpha - \beta/\gamma$. If $\gamma \to 0$, a light-tailed Gumbel distribution emerges.

Several studies have analysed the behaviour of annual maxima precipitation using the $\mathcal{GEV}$ distributions (Papalexiou & Koutsoyiannis, 2013; Ragulina & Reitan, 2017; Westra et al., 2013). Likewise, $\mathcal{GEV}$ distribution is fitted to each AMP time series using the L-moments based on the following statistics: (1) the measure of central tendency (μ_1: coinciding with the mean), (2) the measure of dispersion (μ_2: variation of L-moment), and (3) shape characteristics (τ_3: skewness and kurtosis of L-moment) (Greenwood et al., 1979; Hosking, 1990; Sillitto, 1951):

$$\mu_1 = \alpha - \beta(\gamma^{-1} - \Gamma(-\gamma) \quad \text{(Eq 3.9)}$$

$$\mu_2 = \beta(1 - 2^{\gamma})\Gamma(-\gamma) \quad \text{(Eq 3.10)}$$

$$\tau_3 = \frac{2(1 - 3^{\gamma})}{1 - 2^{\gamma}} - 3 \quad \text{(Eq 3.11)}$$

where $\Gamma(\cdot)$ denotes the gamma function. By finding the root of the equation (11), the shape parameter (γ) can be numerally calculated. Then, by substituting the τ_3 with the sample counterpart, scale (β) and location (α) parameters were calculated by estimating equations (11) and (10).

3.5 Results and discussion

Regional climate types may affect extreme precipitation; therefore, it is important to investigate the behaviour of extreme values in terms of climate subtype. Therefore, in this study, the AMP time series within each climate types were analysed based on (1) trend slope and (2) heaviness of tail.

3.5.1 Extreme precipitation trends

The slope and significance of the trends in each AMP time series in KG climate classification were investigated by Sen's slope estimator and Mann-Kendall test (5% level of significance), respectively (see section 3.4.1 and 3.4.2). Trend variations in AMP are shown in Figure 3.2a. Climate subtypes Af, Am, Aw, and Cwa show a higher inter quantile range (IQR: $Q_3 - Q_1$) of trends compared to other climate subtypes, indicating more variation in terms of the magnitude of trends in extremes. In other words, based on the location of the station, some station time series within these climate subtypes showed high magnitude of trends, while others showed low magnitude. In contrast, other station time series for other climate subtypes showed low trend variation, indicating that most time series showed a similar magnitude of trends no matter where the station for each time series was located. According to the percentage of positive trends within each climate type shown in Figure 3.2b, increasing trends are observed in 70% of climate subtypes (e.g., Af, Am, BWh, BWk, Dfc, Dfd, and ET), while only in Dwd and Dsc did all stations show positive trends.

In contrast, decreasing trends were observed in extremes in a higher number of stations associated with BSh, Csa, Csb, and Dsb, with the largest in Csa (58.7%). Based on the Mann-Kendall test statistic described in Section 3.4.3, trends for stations were classified as "significant increasing," "significant decreasing," or "not significant." According to Figure 3.3, 9.7% of stations had trends classified as significant increasing (e.g., the eastern USA, Asia and northern Europe), while only 2% of stations had trends classified as significant decreasing (e.g., Eastern Australia, Central USA), consistent with the findings of Westra et. (2013). This result corresponds well with the low percentage of significant increasing (positive) trends, as shown in Figure 3.2b. For example, more than 67% of stations associated with subtypes of major climate type A (Af, Am, Aw) showed increasing trends; however, less than 25% of these trends were statistically significant. In addition, the lowest and highest average

percentage of statistically increasing trends was observed in stations associated with major climate types B (11%) and E (48%), respectively. Notably, 88% of the increasing trends were observed in stations associated with climate type E, the highest significant increasing trend among all climate subtypes. Although all stations in Dwd showed increasing trends, none of them was significant.

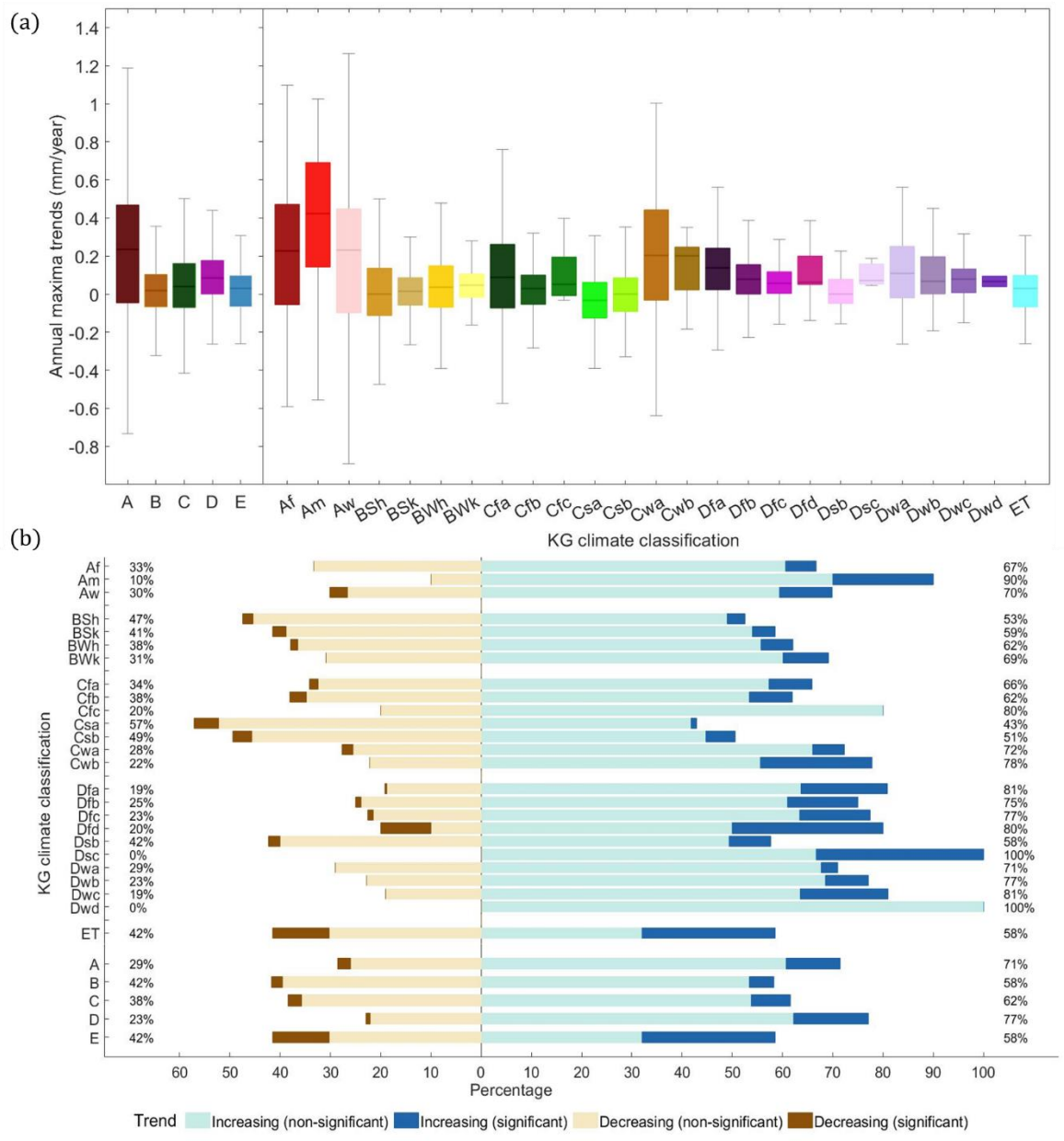

Figure 3.2. Trends of AMP time series for station time series associated with each climate sub-type from 1964 to 2013: (a) variation of trends, (b) percentage of time series showing positive/negative trends and significant positive/negative trends.

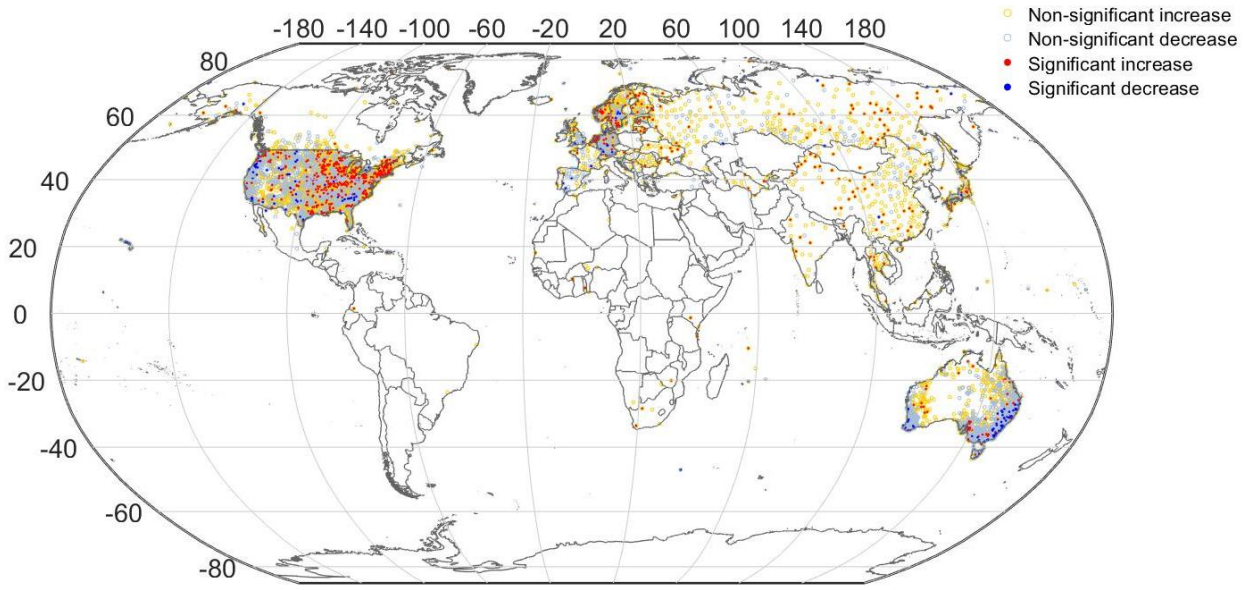

Figure 3.3. Location of Sen's slope estimator trend analyses for 8582 station AMP time series from 1964 to 2013. Light blue open dots indicate non-significant increasing trends, and light red open dots mark non-significant decreasing trends. Dark blue and red-filled dots indicate statistically significant trends, as determined by Mann-Kendall test at 5% level of significance.

3.5.2 Heaviness of tail

In this study, the heaviness of the tail is measured within each AMP time series based on the values of the shape parameter of the fitted $\mathcal{GEV}$ distribution. As discussed earlier in Section 3.4.4, $\gamma > 0$ indicates heavy tailed extremes, while $\gamma < 0$ indicates light-tailed extremes. Variations of γ among all stations associated with each major KG climate type and subtype are presented in Figure 3.4. Heavy-tailed extremes ($\gamma > 0$) and inter quantile range <0.2 (IQR: $Q_3 - Q_1$) were observed for all major climate types except for climate type E with IQR>0.35. In other words, because more heavy tailed extremes were observed in stations associated with climate type E (or climate subtype ET), more frequent and larger magnitude of extreme precipitation was observed for these stations compared to those associated with other major climate types. Likewise, heavy-tailed extremes were observed in the vast majority of climate subtypes, except for Cfc, showing $\gamma < 0$ and negative skewness. The reason for these findings is large magnitude of $\gamma < 0$ (light-tailed extremes) compared to $\gamma > 0$ (heavy-tailed extremes) in stations associated with Cfc. These light-tailed extreme indicate that these stations have less frequent and a smaller magnitude of extreme precipitation compared to stations associated with other subtypes. Although only 10 stations

were associated with climate subtype Dfd (see Figure 3.1), large IQR and positive skewness indicate higher variation in terms of behaviour of heavy-tailed extremes. This finding suggests that more frequent and larger magnitudes of extremes were observed in some stations associated with this climate subtype compared to others. On average, for major climate types, the largest to smallest heavy-tailed extremes (more frequent and larger magnitudes of extremes) were observed in E (0.15), A (0.11), B (0.11), D (0.09), and C (0.09); however, for climate subtypes, large heavy-tailed extremes were observed in Dfd (0.21), ET (0.16), and Am (0.14), while only light-tailed extremes were observed in Cfc (-0.03).

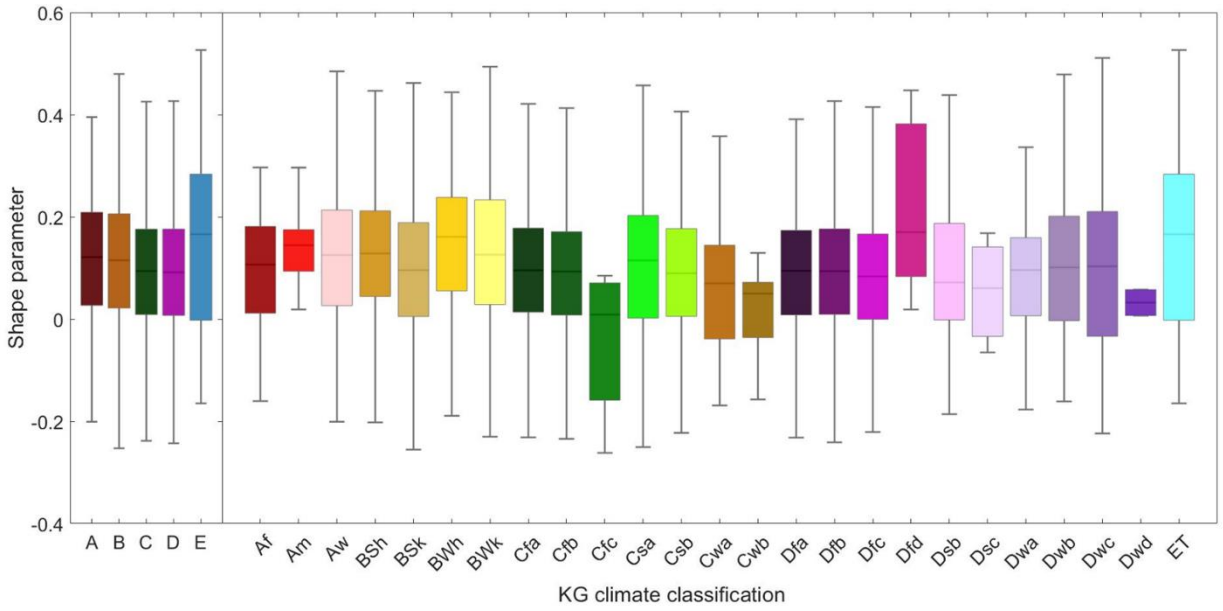

Figure 3.4. Variation of shape parameter (γ) of the fitted $\mathcal{GEV}$ distribution of AMP time series for stations associated with each major climate type (left panel) and climate subtype (right panel) from 1964 to 2013. $\gamma > 0$ indicates heavy-tailed extremes and $\gamma < 0$ light-tailed extremes.

3.6 Summary and Conclusions

In this study, changes in extreme precipitation in terms of climate types were analysed. First, annual maxima precipitation time series of GHCN daily precipitation data from 1964 to 2013 were extracted based on criteria described in Section 3.2. Second, a KG climate type is assigned to each station based on its location corresponding with the Master KG map described in Chapter 2. Results show that Australia and the US had the greatest number of stations (>75%) associated with major climate types C and

D. To analyse extreme precipitation trends for each KG climate subtype, the two non-parametric tests of Mann-Kendall and Sen's slope estimator were applied to each of the AMP time series for each station. Our results indicated a larger variation in the magnitude of trends for stations associated with subtypes Af, Am, Aw, and Cwa, while similar magnitudes of trends were observed for stations associated with other climate subtypes. Decreasing trend is observed in extremes over the majority of stations associated with climate subtypes BSh, Csa, Csb and Dsb but increasing trends in extremes in the remaining climate subtypes (especially in 100% of stations associated with Dsc and Dwd).

However, a small number of stations showing trends of extremes increasing (9.7%) and decreasing (2%) was statistically significant. Overall, on average, the highest and lowest number of stations showing statistically significant increasing trends were associated with climate types B (11%) and E (48%), respectively. By applying the extreme value theory, the heaviness of the tail of each AMP time series were measured based on fitting the $\mathcal{GEV}$ distribution. On average, for major climate types, the largest to smallest heavy-tailed extremes were observed in E (0.15), A (0.11), B (0.11), D (0.09), and C (0.09); however, for climate subtypes, large heavy-tailed extremes were observed in Dfd (0.21), ET (0.16), and Am (0.14), while only light-tailed extremes were observed in Cfc (-0.03). It can be concluded that whenever heavy-tailed extremes were observed, more frequent and larger magnitudes of extreme precipitation occurred. Furthermore, stations associated with the Dfd climate subtype had the most frequent and largest magnitudes of extreme precipitation, whereas Cfc had the least frequent and smallest magnitudes.

One limitation of this study was the lack of accessible data from any stations in the Middle East, Central and northern Africa. Although this data was not available, maybe one could speculate that the behaviour of extremes in these regions is similar to that in other regions with similar climate types. For example, from 1964 to 2013, regions in Africa and the Middle East with BWh climate type may have experienced an increasing trend as well as heavy tailed extreme precipitation, as did other regions with this climate type. Yet, this is a hypothesis that needs to be tested.

As for future research directions, it is important to explore changes in extreme precipitation using different gridded products and climate models as they not only contain

station data but also use other sources to gain access to precipitation data in all land regions with no station record data (e.g., the Middle east, southern America, etc). Also, more investigation is required to measure the most likely changes in extreme precipitation over regions with a specific climate type. This analysis could help researchers to understand which climate types are more susceptible to extreme precipitation. Also, the Monte Carlo Simulation could be a better option than the Mann-Kendall test to analyse trends of extreme precipitation, as the latter is not suitable for datasets with large number of ties (Hodgkins et al., 2017). Although, this study could undoubtedly be improved, it offers discrepancies in extreme precipitation trends in regions in terms of distinct climate types, helping scientists to better understand the relationship between climate type and changes in extreme precipitation.

4. Chapter 4: Summary and conclusion

In Chapter 2 of this manuscript-style MSc thesis, a thorough investigation was conducted to explore discrepancies in KG climate classification maps when different precipitation and temperature data are used. KG maps (from 1980 to 2017) were derived using mean monthly precipitation and temperature adopted from ten global gridded datasets, including four gauge-based (UDEL, CRU, GPCC, CPC), four reanalysis (JRA-55, NCEP/CFSR, MERRA2), and two multi-source (WFDEI, and MSWEP). The extent of similarity (at regional and zonal scale) between pairs of maps is quantified based on the percentage of grid points having the same climate type. Uncertainty in the climate type is measured by counting the distinct number of climate types observed in each grid among the ten KG maps. To reduce the uncertainty in all maps, two robust KG maps (0.5° resolution) were developed by (1) taking the most frequent climate types observed in all KG maps (first Master KG map), and (2) combining temperature and precipitation data from all gridded datasets (second Master KG map). In Chapter 3, an investigation was conducted of changes in extreme precipitation in terms of climate type. Annual maxima precipitation time series were extracted from GHCN daily rainfall station records over the period 1964 to 2013. A climate type was associated to each station based on its location corresponding with the first Master KG map; then, time series of precipitation at each station were classified into 30 different KG climate subtypes. The non-parametric test of Mann-Kendall and Sen's slope estimator were applied to each time series to determine the magnitude and significance of trends. The heaviness of the tail of each time series was measured based on the shape parameter of the fitted $\mathcal{GEV}$ distribution to each time series. Then, stations and their associated climate type with the most frequent and largest magnitude of extreme precipitation were explored.

The following significant results have been achieved and submitted to international scientific journals:

- Notable differences in similarity between KG maps were observed, especially between gauge-based and reanalysis KG maps, which are both less similar than other pairs (e.g., between gauge-based and multi-source maps).

- Focusing on geographical zones (South Temperate, Tropics, North Temperate, and Polar), our results indicate that, in general, the highest and lowest similarity among the maps is observed in the North and South Temperate zones, respectively.
- In each KG map, the largest number of climate subtypes was observed in the North temperate zone
- More than 80% of grid points for the ten maps depict the same major climate type; however, 17.9% of grid points are described by more than one major climate type.
- Similar climate subtypes are observed in 62.8% of grid points for the ten maps in Antarctica, Central Russia, Greenland, the northern part of Africa, and some regions in the eastern USA and Brazil.
- More than 37% of grid points for the ten maps are described by more than one climate subtype (up to seven subtypes in some cases), and very large regions all over the globe (e.g., in south Asia, central and south Africa, west North and South America, etc.) are marked as ambiguous in term of their climate subtype.
- The first and second Master KG maps show more robust spatial patterns than the individual maps and the similarity between the first and second maps is 95%. They cover the specific climate subtypes Dsd, Dwd, Dfb, and Csc that were not depicted in some individual maps (e.g., in some reanalysis maps).
- GPCC-CRU and WFDEI KG maps are the most reliable products to develop KG maps, yet since there are climate subtypes only in GPCC-CRU KG map WFDEI is a better choice.
- The largest portion of available GHCN station daily precipitation station records from 1964 to 2013 were in Australia and USA were associated with major climate types C and D. However, no data from any stations in the Middle East, central and northern Africa, and southern America were accessible.
- Large variations in the magnitude of extreme precipitation trends were indicated over stations associated with Af, Am, Aw, and Cwa, while a similar magnitude of trends was observed over stations associated with other climate subtypes.
- Most stations associated with climate subtype BSh, Csa, Csb, Dsb experienced decreases in extreme precipitation, stations associated with the remaining climate

subtypes experienced increases (especially in 100% of stations associated with Dsc and Dwd).

- A significant increasing trend was shown in 9.7% of stations in the eastern USA, Asia, and northern Europe; however, only 2% of stations in Eastern Australia, and Central USA showed significant decreasing trends. On average, a statistically significant increasing trend associated with the climate types B (11%) and E (48%) was shown at the lowest and highest number of stations, respectively.
- A similar variation was observed in heavy-tailed extremes over stations associated with the major climate types A, B, C, and D, while a large variation was seen in some stations associated with major climate type E.
- Largest and smallest heavy-tailed extremes were observed in (1) major climate types E, and C, and (2) climate subtypes Dfd and Dwd. Light-tailed extremes were observed in Cfc.
- The most frequent and largest magnitudes of extreme precipitation were in stations associated with the Dfd climate subtype, whereas the least frequent and smallest magnitudes were in those associated with Cfc.

5. Chapter 5: Recommendations for future work

- This research work investigated variation in determining climate classification using datasets at 0.5° resolution; however, it would be worth exploring different climate classifications and their variations in different products and the potential effects of downscaling methods on finer spatial resolution maps.
- The true variability of the climate subtypes in each grid cannot be revealed by the datasets used here or from any other set. Instead, large ensemble datasets based on stochastic methods could more robustly quantify the true uncertainty.
- This research work offers the first global analysis of variations in extreme precipitation changes in terms of climate type using daily station records of precipitation; however, it is important to study these variations using gridded precipitation products because they provide more widespread data than station records, which cover data in regions that are missing station records (e.g., the Middle East, Southern Africa, etc.). As well, the Monte Carlo Simulation could be a better option to analyse extreme precipitation trends, as the Mann-Kendall test is not suitable for datasets with a large number of ties (Hodgkins et al., 2017). If Monte Carlo Simulation is used, CoSMoS package (more details in Appendix) can simplify the assessment of the significance of extreme precipitation trends.
- A more detailed investigation is required to measure the most likely changes in extreme precipitation based on the climate types of a region at the global scale. This analysis could help researchers to understand which climate type is more susceptible to extreme precipitation.

6. Appendix

Package development

CoSMoS-MATLAB package (v0.9) is a user-friendly toolbox that helps scientists and researchers generate univariate time series mimicking hydro-climatic processes (such as precipitation, wind, temperature, relative humidity, river discharge, etc). The stochastic framework behind CoSMoS unifies, extends, and improves a modelling strategy that generates time series by transforming "parent" Gaussian time series with specific statistical characteristics (more detailed in Papalexiou, 2018). The simulation scheme (1) introduces parametric correlation transformation functions, (2) enables a straightforward estimation of the parent-Gaussian process that yields the target process after the marginal back transformation, and (3) offers a simple, fast and efficient simulation procedure for every stationary process at any spatiotemporal scale. The user provides the target time series characteristics, that is, the marginal distribution and autocorrelation structure, and the package does the rest. The Graphical User Interface (GUI) makes it easy to select specific distributions and autocorrelation structures, and generate time series of any length. The generated time series are visualized in a panel of figures that depict and compare the target distribution and autocorrelation with the corresponding empirical ones (Figure 6.1). The package was published on 17th of October 2019 on MathWorks and GitHub. This package can be used to assess significance of extreme precipitation trends based on the Monte Carlo Simulations.

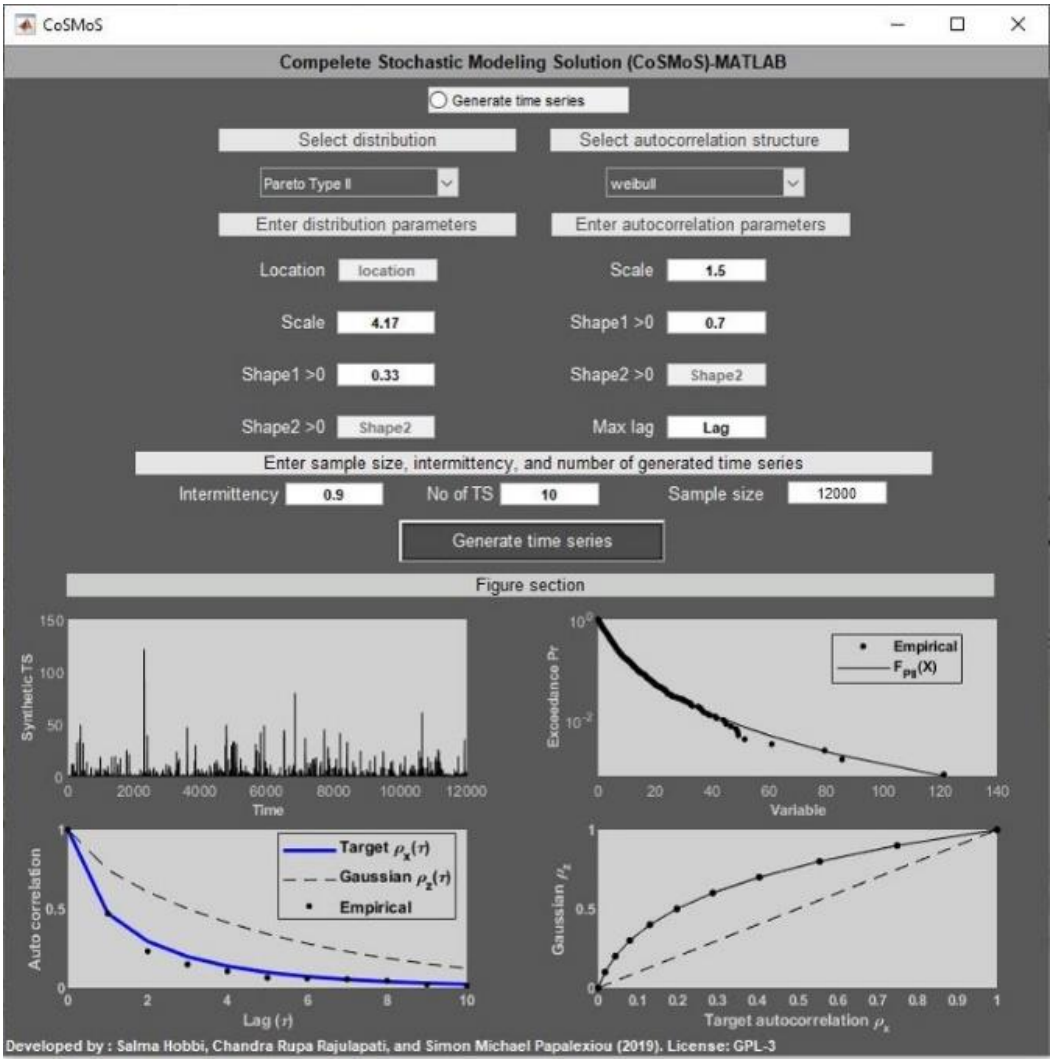

Figure 6.1. Graphical User Interface of CoSMoS-MATLAB package.

This package is available at:

- MathWorks: https://www.mathworks.com/matlabcentral/fileexchange/73051-cosmos-matlab
- GitHub: https://github.com/SMPLab/CoSMoS-MATLAB

Acquire data: Global Historical Climate Network Daily (GHCN-D)

This database provides more than 100000 station precipitation records at the global scale. Data can be downloaded through the following approach:

Start by downloading "ghcnd-stations.txt," which has metadata for all stations by using the following link: https://www1.ncdc.noaa.gov/pub/data/ghcn/daily/ghcnd-stations.txt

Then download one of the following TAR files:

−"ghcnd-all.tar.gz" if you want all of GHCN-Daily, OR

−"ghcnd-gsn.tar.gz" if you only want the GCOS Surface Network (GSN), OR

−"ghcnd-hcn.tar.gz" if you only want the U.S. Historical Climatology Network (U.S. HCN).

Then uncompress and untar the contents of the tar file,

e.g., by using the following Linux command:

tar xzvf ghcnd_xxx.tar.gz

Where "xxx" stands for "all", "hcn", or "gsn" as applicable. The files will be

extracted into a subdirectory under the directory where the command is issued.

ALTERNATIVELY, if you only need data for one station:

−Find the station's name in "ghcnd-stations.txt" and note its station

−identification code (e.g., PHOENIX AP (Airport) is "USW00023183"); and

−Download the data file (i.e., ".dly" file) that corresponds to this code

− (e.g., "USW00023183.dly" has the data for PHOENIX AP).

−Note that the ".dly" file is located in the "all" subdirectory.

COPYRIGHT PERMISSION

Chapter 2 is under review by the Journal of Climate so there would be no copyright permission.

7. Chapter 7: List of References

Achberger, C., & Chen, D. (2006). Trend of extreme precipitation in Sweden and Norway during 1961-2004. *Earth*, *31*, 7731986.

Adler, R. F., Huffman, G. J., Chang, A., Ferraro, R., Xie, P.-P., Janowiak, J., Rudolf, B., Schneider, U., Curtis, S., Bolvin, D., Gruber, A., Susskind, J., Arkin, P., & Nelkin, E. (2003). The Version-2 Global Precipitation Climatology Project (GPCP) Monthly Precipitation Analysis (1979–Present). *JOURNAL OF HYDROMETEOROLOGY*, *4*, 21.

Alexander, L. V., & Arblaster, J. M. (2009). Assessing trends in observed and modelled climate extremes over Australia in relation to future projections. *International Journal of Climatology*, *29*(3), 417–435. https://doi.org/10.1002/joc.1730

Alexander, L. V., Zhang, X., Peterson, T. C., Caesar, J., Gleason, B., Klein Tank, A. M. G., Haylock, M., Collins, D., Trewin, B., Rahimzadeh, F., Tagipour, A., Rupa Kumar, K., Revadekar, J., Griffiths, G., Vincent, L., Stephenson, D. B., Burn, J., Aguilar, E., Brunet, M., … Vazquez-Aguirre, J. L. (2006). Global observed changes in daily climate extremes of temperature and precipitation. *Journal of Geophysical Research*, *111*(D5), D05109. https://doi.org/10.1029/2005JD006290

Alley, B., Berntsen, L., & Chen, B. (2007). *Intergovernmental Panel on Climate Change Fourth Assessment Report*.

Araya, A., Keesstra, S. D., & Stroosnijder, L. (2010). A new agro-climatic classification for crop suitability zoning in northern semi-arid Ethiopia. *Agricultural and Forest Meteorology*, *150*(7–8), 1057–1064. https://doi.org/10.1016/j.agrformet.2010.04.003

Bailey, R. G. (2009). *Ecosystem geography: From ecoregions to sites*. Springer Science & Business Media.

Barrett, B., Charles, J. W., & Temte, J. L. (2015). Climate change, human health, and epidemiological transition. *Preventive Medicine*, *70*, 69–75. https://doi.org/10.1016/j.ypmed.2014.11.013

Beck, H. E., Wood, E. F., Pan, M., Fisher, C. K., Miralles, D. G., van Dijk, A. I. J. M., McVicar, T. R., & Adler, R. F. (2019). MSWEP V2 Global 3-Hourly 0.1° Precipitation: Methodology and Quantitative Assessment. *Bulletin of the American Meteorological Society*, *100*(3), 473–500. https://doi.org/10.1175/BAMS-D-17-0138.1

Beck, H. E., Zimmermann, N. E., McVicar, T. R., Vergopolan, N., Berg, A., & Wood, E. F. (2018). Present and future Köppen-Geiger climate classification maps at 1-km resolution. *Scientific Data*, *5*(1), 180214. https://doi.org/10.1038/sdata.2018.214

Behrisch, M., & Weber, M. (Eds.). (2019). *Simulating Urban Traffic Scenarios: 3rd SUMO Conference 2015 Berlin, Germany*. Springer International Publishing. https://doi.org/10.1007/978-3-319-33616-9

Bosilovich, M. G., Kennedy, J., Dee, D., Allan, R., & O'Neill, A. (2013). On the Reprocessing and Reanalysis of Observations for Climate. In G. R. Asrar & J. W. Hurrell (Eds.), *Climate Science for Serving Society* (pp. 51–71). Springer Netherlands. https://doi.org/10.1007/978-94-007-6692-1_3

Bouma, E. (2005). Development of comparable agro-climatic zones for the international exchange of data on the efficacy and crop safety of plant protection products1. *EPPO Bulletin*, *35*(2), 233–238. https://doi.org/10.1111/j.1365-2338.2005.00830.x

Chen, D., & Chen, H. W. (2013). Using the Köppen classification to quantify climate variation and change: An example for 1901–2010. *Environmental Development*, *6*, 69–79. https://doi.org/10.1016/j.envdev.2013.03.007

Chen, M., Shi, W., Xie, P., Silva, V. B. S., Kousky, V. E., Wayne Higgins, R., & Janowiak, J. E. (2008). Assessing objective techniques for gauge-based analyses of global daily precipitation. *Journal of Geophysical Research*, *113*(D4), D04110. https://doi.org/10.1029/2007JD009132

Costa, M. H., & Foley, J. A. (1998). A comparison of precipitation datasets for the Amazon Basin. *Geophysical Research Letters*, *25*(2), 155–158. https://doi.org/10.1029/97GL03502

Cramer, W. P., & Leemans, R. (1993). Assessing Impacts of Climate Change on Vegetation Using Climate Classification Systems. In A. M. Solomon & H. H. Shugart (Eds.), *Vegetation Dynamics & Global Change* (pp. 190–217). Springer US. https://doi.org/10.1007/978-1-4615-2816-6_10

de Oliveira Aparecido, L. E., da Silva Cabral de Moraes, J. R., de Meneses, K. C., Torsoni, G. B., de Lima, R. F., & Costa, C. T. S. (2020). Köppen-Geiger and Camargo climate classifications for the Midwest of Brasil. *Theoretical and Applied Climatology*, *142*(3–4), 1133–1145. https://doi.org/10.1007/s00704-020-03358-2

de Sá Júnior, A., de Carvalho, L. G., da Silva, F. F., & de Carvalho Alves, M. (2012). Application of the Köppen classification for climatic zoning in the state of Minas Gerais, Brazil. *Theoretical and Applied Climatology*, *108*(1–2), 1–7. https://doi.org/10.1007/s00704-011-0507-8

Diaz, H. F., & Eischeid, J. K. (2007). Disappearing “alpine tundra” Köppen climatic type in the western United States. *Geophysical Research Letters*, *34*(18).

Domroes, M. (2003). Climatological characteristics of the tropics in China: Climate classification schemes between German scientists and Huang Bingwei. *Journal of Geographical Sciences*, *13*(3), 271–285.

Donat, M. G., Lowry, A. L., Alexander, L. V., O’Gorman, P. A., & Maher, N. (2016a). More extreme precipitation in the world’s dry and wet regions. *Nature Climate Change*, *6*(5), 508–513. https://doi.org/10.1038/nclimate2941

Donat, M. G., Lowry, A. L., Alexander, L. V., O’Gorman, P. A., & Maher, N. (2016b). More extreme precipitation in the world’s dry and wet regions. *Nature Climate Change*, *6*(5), 508–513. https://doi.org/10.1038/nclimate2941

Dore, M. H. I. (2005). Climate change and changes in global precipitation patterns: What do we know? *Environment International*, *31*(8), 1167–1181. https://doi.org/10.1016/j.envint.2005.03.004

Elmendorf, S. C., Henry, G. H., Hollister, R. D., Björk, R. G., Boulanger-Lapointe, N., Cooper, E. J., Cornelissen, J. H., Day, T. A., Dorrepaal, E., Elumeeva, T. G., & others. (2012). Plot-scale evidence of tundra vegetation change and links to recent summer warming. *Nature Climate Change*, *2*(6), 453–457.

Evans, J. P. (2009). 21st century climate change in the Middle East. *Climatic Change*, *92*(3–4), 417–432. https://doi.org/10.1007/s10584-008-9438-5

Folland, C. K., Rayner, N. A., Brown, S. J., Smith, T. M., Shen, S. S. P., Parker, D. E., Macadam, I., Jones, P. D., Jones, R. N., Nicholls, N., & Sexton, D. M. H. (2001). Global temperature

change and its uncertainties since 1861. *Geophysical Research Letters*, *28*(13), 2621–2624. https://doi.org/10.1029/2001GL012877

Forestieri, A., Arnone, E., Blenkinsop, S., Candela, A., Fowler, H., & Noto, L. V. (2018). The impact of climate change on extreme precipitation in Sicily, Italy. *Hydrological Processes*, *32*(3), 332–348. https://doi.org/10.1002/hyp.11421

Fowler, A., & Hennessy, K. (1995). Potential impacts of global warming on the frequency and magnitude of heavy precipitation. *Natural Hazards*, *11*(3), 283–303.

Fowler, H. J., & Kilsby, C. G. (2003). A regional frequency analysis of United Kingdom extreme rainfall from 1961 to 2000. *International Journal of Climatology*, *23*(11), 1313–1334. https://doi.org/10.1002/joc.943

Fraedrich, K., Gerstengarbe, F.-W., & Werner, P. (2001). Climate shifts during the last century. *Climatic Change*, *50*(4), 405–417.

Gao, X., & Giorgi, F. (2008). Increased aridity in the Mediterranean region under greenhouse gas forcing estimated from high resolution simulations with a regional climate model. *Global and Planetary Change*, *62*(3–4), 195–209. https://doi.org/10.1016/j.gloplacha.2008.02.002

Geiger, R. (1954). Klassifikation der klimate nach W. Köppen. *Landolt-Börnstein–Zahlenwerte Und Funktionen Aus Physik, Chemie, Astronomie, Geophysik Und Technik*, *3*, 603–607.

Gelaro, R., McCarty, W., Suárez, M. J., Todling, R., Molod, A., Takacs, L., Randles, C. A., Darmenov, A., Bosilovich, M. G., Reichle, R., Wargan, K., Coy, L., Cullather, R., Draper, C., Akella, S., Buchard, V., Conaty, A., da Silva, A. M., Gu, W., … Zhao, B. (2017). The Modern-Era Retrospective Analysis for Research and Applications, Version 2

(MERRA-2). *Journal of Climate*, *30*(14), 5419–5454. https://doi.org/10.1175/JCLI-D-16-0758.1

Gleckler, P. J., Taylor, K. E., & Doutriaux, C. (2008). Performance metrics for climate models. *Journal of Geophysical Research*, *113*(D6), D06104. https://doi.org/10.1029/2007JD008972

Gnanadesikan, A., & Stouffer, R. J. (2006). Diagnosing atmosphere-ocean general circulation model errors relevant to the terrestrial biosphere using the Köppen climate classification. *Geophysical Research Letters*, *33*(22), L22701. https://doi.org/10.1029/2006GL028098

Gocic, M., & Trajkovic, S. (2013). Analysis of changes in meteorological variables using Mann-Kendall and Sen's slope estimator statistical tests in Serbia. *Global and Planetary Change*, *100*, 172–182. https://doi.org/10.1016/j.gloplacha.2012.10.014

Goswami, B. N., Venugopal, V., Sengupta, D., Madhusoodanan, M. S., & Xavier, P. K. (2006). Increasing Trend of Extreme Rain Events Over India in a Warming Environment. *Science*, *314*(5804), 1442–1445. https://doi.org/10.1126/science.1132027

Greenwood, J. A., Landwehr, J. M., Matalas, N. C., & Wallis, J. R. (1979). Probability weighted moments: Definition and relation to parameters of several distributions expressable in inverse form. *Water Resources Research*, *15*(5), 1049–1054. https://doi.org/10.1029/WR015i005p01049

Groisman, P. Y., Knight, R. W., Easterling, D. R., Karl, T. R., Hegerl, G. C., & Razuvaev, V. N. (2005). Trends in intense precipitation in the climate record. *Journal of Climate*, *18*(9), 1326–1350.

Guetter, J., & Kutzbach, J. E. (1990). *A MODIFIED KOPPEN CLASSIFICATION APPLIED TO MODEL SIMULATIONS OF GLACIAL AND INTERGLACIAL CLIMATES*. 23.

Gumbel, E. J. (1958). *Statistics of extremes*. Columbia university press.

Harris, I., Jones, P. D., Osborn, T. J., & Lister, D. H. (2014). Updated high-resolution grids of monthly climatic observations - the CRU TS3.10 Dataset: UPDATED HIGH-RESOLUTION GRIDS OF MONTHLY CLIMATIC OBSERVATIONS. *International Journal of Climatology*, *34*(3), 623–642. https://doi.org/10.1002/joc.3711

Hawkins, E., Ortega, P., Suckling, E., Schurer, A., Hegerl, G., Jones, P., Joshi, M., Osborn, T. J., Masson-Delmotte, V., Mignot, J., Thorne, P., & van Oldenborgh, G. J. (2017). Estimating Changes in Global Temperature since the Preindustrial Period. *Bulletin of the American Meteorological Society*, *98*(9), 1841–1856. https://doi.org/10.1175/BAMS-D-16-0007.1

Hersbach, H., Bell, B., Berrisford, P., Hirahara, S., Horányi, A., Muñoz-Sabater, J., Nicolas, J., Peubey, C., Radu, R., Schepers, D., Simmons, A., Soci, C., Abdalla, S., Abellan, X., Balsamo, G., Bechtold, P., Biavati, G., Bidlot, J., Bonavita, M., … Thépaut, J. (2020). The ERA5 global reanalysis. *Quarterly Journal of the Royal Meteorological Society*, *146*(730), 1999–2049. https://doi.org/10.1002/qj.3803

Holdridge, L. R. (1947). Determination of world plant formations from simple climatic data. *Science*, *105*(2727), 367–368.

Hosking, J. R. M. (1990). L-Moments: Analysis and Estimation of Distributions Using Linear Combinations of Order Statistics. *Journal of the Royal Statistical Society: Series B (Methodological)*, *52*(1), 105–124. https://doi.org/10.1111/j.2517-6161.1990.tb01775.x

Hossain, F., Degu, A. M., Yigzaw, W., Burian, S., Niyogi, D., Shepherd, J. M., & Pielke, R. (2012). Climate Feedback–Based Provisions for Dam Design, Operations, and Water Management in the 21st Century. *Journal of Hydrologic Engineering*, *17*(8), 837–850. https://doi.org/10.1061/(ASCE)HE.1943-5584.0000541

Hundecha, Y., & Bárdossy, A. (2005). Trends in daily precipitation and temperature extremes across western Germany in the second half of the 20th century. *International Journal of Climatology*, *25*(9), 1189–1202. https://doi.org/10.1002/joc.1182

Jenkinson, A. F. (1955). The frequency distribution of the annual maximum (or minimum) values of meteorological elements. *Quarterly Journal of the Royal Meteorological Society*, *81*(348), 158–171.

Kalvová, J., Halenka, T., Bezpalcová, K., & Nemešová, I. (2003). Köppen climate types in observed and simulated climates. *Studia Geophysica et Geodaetica*, *47*(1), 185–202.

Karl, T. R. (2003). Modern Global Climate Change. *Science*, *302*(5651), 1719–1723. https://doi.org/10.1126/science.1090228

Kendall, M. G., & Gibbons, J. (1975). Rank correlation methods, 1970. *Griffin, London*.

Kharyutkina, E. V., Ippolitov, I. I., & Loginov, S. V. (2012). The variability of radiative balance elements and air temperature over the Asian region of Russia. *Biogeosciences*, *9*(3), 1113–1123. https://doi.org/10.5194/bg-9-1113-2012

Kidston, J., Frierson, D. M. W., Renwick, J. A., & Vallis, G. K. (2010). Observations, Simulations, and Dynamics of Jet Stream Variability and Annular Modes. *Journal of Climate*, *23*(23), 6186–6199. https://doi.org/10.1175/2010JCLI3235.1

Kim, C., Suh, M.-S., & Hong, K.-O. (2009). Bayesian Changepoint Analysis of the Annual Maximum of Daily and Subdaily Precipitation over South Korea. *Journal of Climate*, *22*(24), 6741–6757. https://doi.org/10.1175/2009JCLI2800.1

Kim, H.-J., Wang, B., Ding, Q., & Chung, I.-U. (2008). Changes in Arid Climate over North China Detected by the Koppen Climate Classification. *Journal of the Meteorological Society of Japan*, *86*(6), 981–990. https://doi.org/10.2151/jmsj.86.981

Kleidon, A., Fraedrich, K., & Heimann, M. (2000). *A Green Planet Versus a Desert World: Estimating the Maximum Effect of Vegetation on the Land Surface Climate*. 23.

Kobayashi, S., Ota, Y., Harada, Y., Ebita, A., Moriya, M., Onoda, H., Onogi, K., Kamahori, H., Kobayashi, C., Endo, H., Miyaoka, K., & Takahashi, K. (2015). The JRA-55 Reanalysis: General Specifications and Basic Characteristics. *Journal of the Meteorological Society of Japan. Ser. II*, *93*(1), 5–48. https://doi.org/10.2151/jmsj.2015-001

Koppen, W. das. (1936). Das geographische system der klimat. *Handbuch Der Klimatologie*, 46.

Köppen, & Geiger. (1928). *Klimakarte der erde*. Justus Perthes.

Köppen, W. (1918). Klassifikation der Klima nach Temperatur, Niederschlag und Jahreslauf. *Pet. Mitt.*, *64*, 243–248.

Köppen, W. (1923). *Die klimate der erde: Grundriss der klimakunde*. Walter de Gruyter GmbH & Co KG.

Kottek, M., Grieser, J., Beck, C., Rudolf, B., & Rubel, F. (2006). World map of the Köppen-Geiger climate classification updated. *Meteorologische Zeitschrift*, *15*(3), 259–263.

Kravtsov, S., Wyatt, M. G., Curry, J. A., & Tsonis, A. A. (2014). Two contrasting views of multidecadal climate variability in the twentieth century: Two views of climate

variability. *Geophysical Research Letters*, *41*(19), 6881–6888. https://doi.org/10.1002/2014GL061416

Kriticos, D. J., Webber, B. L., Leriche, A., Ota, N., Macadam, I., Bathols, J., & Scott, J. K. (2012). CliMond: Global high-resolution historical and future scenario climate surfaces for bioclimatic modelling: CliMond: climate surfaces for bioclimatic modelling. *Methods in Ecology and Evolution*, *3*(1), 53–64. https://doi.org/10.1111/j.2041-210X.2011.00134.x

Kunkel, K. E. (2003). North American trends in extreme precipitation. *Natural Hazards*, *29*(2), 291–305.

Leadbetter, M. R. (1984). Extremes and related properties of random sequences and processes. *Metrika*, *31*(1), 98–98.

Lettenmaier, D. P., Wood, E. F., & Wallis, J. R. (1994). Hydro-climatological trends in the continental United States, 1948-88. *Journal of Climate*, *7*(4), 586–607.

Liu, J., Shi, Z., & Tan, X. (2021). Measuring the dynamic evolution of road network vulnerability to floods: A case study of Wuhan, China. *Travel Behaviour and Society*, *23*, 13–24. https://doi.org/10.1016/j.tbs.2020.10.009

Lohmann, U., Sausen, R., Bengtsson, L., Cubasch, U., Perlwitz, J., & Roeckner, E. (1993). The Köppen climate classification as a diagnostic tool for general circulation models. *Climate Research*, *3*, 177–193. https://doi.org/10.3354/cr003177

MacKellar, N. C., Hewitson, B. C., & Tadross, M. A. (2007). Namaqualand's climate: Recent historical changes and future scenarios. *Journal of Arid Environments*, *70*(4), 604–614. https://doi.org/10.1016/j.jaridenv.2006.03.024

Mailhot, A., Kingumbi, A., Talbot, G., & Poulin, A. (2010). Future changes in intensity and seasonal pattern of occurrence of daily and multi-day annual maximum precipitation over Canada. *Journal of Hydrology*, *388*(3–4), 173–185. https://doi.org/10.1016/j.jhydrol.2010.04.038

Mann, H. B. (1945). Nonparametric Tests Against Trend. *Econometrica*, *13*(3), 245. https://doi.org/10.2307/1907187

Maracchi, G., Sirotenko, O., & Bindi, M. (2005). *IMPACTS OF PRESENT AND FUTURE CLIMATE VARIABILITY ON AGRICULTURE AND FORESTRY IN THE TEMPERATE REGIONS: EUROPE*. 19.

Martel, J.-L., Mailhot, A., & Brissette, F. (2020). Global and Regional Projected Changes in 100-yr Subdaily, Daily, and Multiday Precipitation Extremes Estimated from Three Large Ensembles of Climate Simulations. *Journal of Climate*, *33*(3), 1089–1103. https://doi.org/10.1175/JCLI-D-18-0764.1

Meybeck, A., Food and Agriculture Organization of the United Nations, & Organisation for Economic Co-operation and Development (Eds.). (2012). *Building resilience for adaptation to climate change in the agriculture sector: Proceedings of a Joint FAO/OECD Workshop 23-24 April 2012*. Food And Agriculture Organization Of The United Nations, Organisation for Economic Co-operation and Development.

Min, S.-K., Zhang, X., Zwiers, F. W., & Hegerl, G. C. (2011). Human contribution to more-intense precipitation extremes. *Nature*, *470*(7334), 378–381.

Mitchell, T. D., Carter, T. R., Jones, P. D., Hulme, M., New, M., & others. (2004). A comprehensive set of high-resolution grids of monthly climate for Europe and the

globe: The observed record (1901–2000) and 16 scenarios (2001–2100). *Tyndall Centre for Climate Change Research Working Paper*, *55*(0), 25.

Mohammat, A., Wang, X., Xu, X., Peng, L., Yang, Y., Zhang, X., Myneni, R. B., & Piao, S. (2013). Drought and spring cooling induced recent decrease in vegetation growth in Inner Asia. *Agricultural and Forest Meteorology*, *178–179*, 21–30. https://doi.org/10.1016/j.agrformet.2012.09.014

Nazarova, L., Herzschuh, U., Wetterich, S., Kumke, T., & Pestryakova, L. (2011). Chironomid-based inference models for estimating mean July air temperature and water depth from lakes in Yakutia, northeastern Russia. *Journal of Paleolimnology*, *45*(1), 57–71. https://doi.org/10.1007/s10933-010-9479-4

New, M., Hulme, M., & Jones, P. (2000). Representing Twentieth-Century Space–Time Climate Variability. Part II: Development of 1901–96 Monthly Grids of Terrestrial Surface Climate. *JOURNAL OF CLIMATE*, *13*, 22.

Olson, D. M., Dinerstein, E., Wikramanayake, E. D., Burgess, N. D., Powell, G. V. N., Underwood, E. C., D'amico, J. A., Itoua, I., Strand, H. E., Morrison, J. C., Loucks, C. J., Allnutt, T. F., Ricketts, T. H., Kura, Y., Lamoreux, J. F., Wettengel, W. W., Hedao, P., & Kassem, K. R. (2001). Terrestrial Ecoregions of the World: A New Map of Life on Earth. *BioScience*, *51*(11), 933. https://doi.org/10.1641/0006-3568(2001)051[0933:TEOTWA]2.0.CO;2

Papalexiou, S. M. (2018). Unified theory for stochastic modelling of hydroclimatic processes: Preserving marginal distributions, correlation structures, and intermittency. *Advances in Water Resources*, *115*, 234–252.

Papalexiou, S. M., & Koutsoyiannis, D. (2013). Battle of extreme value distributions: A global survey on extreme daily rainfall: SURVEY ON EXTREME DAILY RAINFALL. *Water Resources Research*, *49*(1), 187–201. https://doi.org/10.1029/2012WR012557

Papalexiou, S. M., & Montanari, A. (2019). Global and Regional Increase of Precipitation Extremes under Global Warming. *Water Resources Research*. https://doi.org/10.1029/2018WR024067

Parker, J., McIntyre, D., & Noble, R. (2010). Characterizing fecal contamination in stormwater runoff in coastal North Carolina, USA. *Water Research*, *44*(14), 4186–4194.

Peel, M. C., Finlayson, B. L., & Mcmahon, T. A. (2007). *Updated world map of the Köppen-Geiger climate classification*. 36.

Petrov, K. A., Sofronova, V. E., Bubyakina, V. V., Perk, A. A., Tatarinova, T. D., Ponomarev, A. G., Chepalov, V. A., Okhlopkova, Zh. M., Vasilieva, I. V., & Maximov, T. Ch. (2011). Woody plants of Yakutia and low-temperature stress. *Russian Journal of Plant Physiology*, *58*(6), 1011–1019. https://doi.org/10.1134/S1021443711060148

Pitman, A. J., & Perkins, S. E. (2009). Global and Regional Comparison of Daily 2-m and 1000-hPa Maximum and Minimum Temperatures in Three Global Reanalyses. *Journal of Climate*, *22*(17), 4667–4681. https://doi.org/10.1175/2009JCLI2799.1

Pregnolato, M., Ford, A., Wilkinson, S. M., & Dawson, R. J. (2017). The impact of flooding on road transport: A depth-disruption function. *Transportation Research Part D: Transport and Environment*, *55*, 67–81. https://doi.org/10.1016/j.trd.2017.06.020

Pujol, N., Neppel, L., & Sabatier, R. (2007). Regional tests for trend detection in maximum precipitation series in the French Mediterranean region. *Hydrological Sciences Journal*, *52*(5), 956–973. https://doi.org/10.1623/hysj.52.5.956

Ragulina, G., & Reitan, T. (2017). Generalized extreme value shape parameter and its nature for extreme precipitation using long time series and the Bayesian approach. *Hydrological Sciences Journal*, *62*(6), 863–879. https://doi.org/10.1080/02626667.2016.1260134

Rajulapati, C. R., Papalexiou, S. M., Clark, M. P., Razavi, S., Tang, G., & Pomeroy, J. W. (2020). Assessment of Extremes in Global Precipitation Products: How Reliable Are They? *Journal of Hydrometeorology*, *21*(12), 2855–2873. https://doi.org/10.1175/JHM-D-20-0040.1

Rohli, R. V., Andrew Joyner, T., Reynolds, S. J., Shaw, C., & Vázquez, J. R. (2015). Globally Extended Köppen–Geiger climate classification and temporal shifts in terrestrial climatic types. *Physical Geography*, *36*(2), 142–157. https://doi.org/10.1080/02723646.2015.1016382

Rubel, F., & Kottek, M. (2010). Observed and projected climate shifts 1901–2100 depicted by world maps of the Köppen-Geiger climate classification. *Meteorologische Zeitschrift*, *19*(2), 135–141.

Rudolf, B., Becker, A., Schneider, U., Meyer-Christoffer, A., & Ziese, M. (2010). The new "GPCC Full Data Reanalysis Version 5" providing high-quality gridded monthly precipitation data for the global land-surface is public available since December 2010. *GPCC Status Rep*.

Ruiz-Alvarez, O., Singh, V. P., Enciso-Medina, J., Ontiveros-Capurata, R. E., & Santos, C. A. C. (2020). Observed trends in daily extreme precipitation indices in Aguascalientes, Mexico. *Meteorological Applications*, *27*(1). https://doi.org/10.1002/met.1838

Russell, R. J. (1931). *Dry Climates of the United States. Part I, The Climatic Map. Univ. Of California, Publ*. Geog.

Saha, S., Moorthi, S., Wu, X., Wang, J., Nadiga, S., Tripp, P., Behringer, D., Hou, Y.-T., Chuang, H., Iredell, M., Ek, M., Meng, J., Yang, R., Mendez, M. P., van den Dool, H., Zhang, Q., Wang, W., Chen, M., & Becker, E. (2014). The NCEP Climate Forecast System Version 2. *Journal of Climate*, *27*(6), 2185–2208. https://doi.org/10.1175/JCLI-D-12-00823.1

Saidi, H., Ciampittiello, M., Dresti, C., & Ghiglieri, G. (2015). Assessment of Trends in Extreme Precipitation Events: A Case Study in Piedmont (North-West Italy). *Water Resources Management*, *29*(1), 63–80. https://doi.org/10.1007/s11269-014-0826-5

Sarfaraz, S., Arsalan, M. H., & Fatima, H. (2014). Regionalizing the climate of Pakistan using Köppen classification system. *Pakistan Geogr Rev*, *69*, 111–132.

Sen, P. K. (1968). Estimates of the regression coefficient based on Kendall's tau. *Journal of the American Statistical Association*, *63*(324), 1379–1389.

Sillitto, G. P. (1951). Interrelations between certain linear systematic statistics of samples from any continuous population. *Biometrika*, *38*(3/4), 377–382.

Sohn, J. (2006). Evaluating the significance of highway network links under the flood damage: An accessibility approach. *Transportation Research Part A: Policy and Practice*, *40*(6), 491–506. https://doi.org/10.1016/j.tra.2005.08.006

Stoffelen, A. (1998). Toward the true near-surface wind speed: Error modeling and calibration using triple collocation. *Journal of Geophysical Research: Oceans*, *103*(C4), 7755–7766. https://doi.org/10.1029/97JC03180

Sun, Q., Miao, C., Duan, Q., Ashouri, H., Sorooshian, S., & Hsu, K. (2018). A Review of Global Precipitation Data Sets: Data Sources, Estimation, and Intercomparisons. *Reviews of Geophysics*, *56*(1), 79–107. https://doi.org/10.1002/2017RG000574

Tabari, H., & Marofi, S. (2011). Changes of pan evaporation in the west of Iran. *Water Resources Management*, *25*(1), 97–111.

Tan, X., Gan, T. Y., & Shao, D. (2017). Effects of persistence and large-scale climate anomalies on trends and change points in extreme precipitation of Canada. *Journal of Hydrology*, *550*, 453–465. https://doi.org/10.1016/j.jhydrol.2017.05.028

Taylor, K. E., Stouffer, R. J., & Meehl, G. A. (2012). An Overview of CMIP5 and the Experiment Design. *Bulletin of the American Meteorological Society*, *93*(4), 485–498. https://doi.org/10.1175/BAMS-D-11-00094.1

Taylor, M. A. P., & Philp, M. L. (2015). Investigating the impact of maintenance regimes on the design life of road pavements in a changing climate and the implications for transport policy. *Transport Policy*, *41*, 117–135. https://doi.org/10.1016/j.tranpol.2015.01.005

Taylor, M. A., & Philp, M. L. (2016). Beyond agriculture: A review of the Thornthwaite Moisture Index with respect to road pavements and other infrastructure applications. *International Journal of Sustainable Transportation*, *10*(6), 528–540.

Thornthwaite, C. W. (1948). *An Approach toward a Rational Classification of Climate*. 49.

Trenberth, K., Jones, P., Ambenje, P., Bojariu, R., Easterling, D., Tank, A. K., Parker, D., Rahimzadeh, F., Renwick, J., Rusticucci, M., & others. (2007). Observations: Surface and atmospheric climate change. Chapter 3. *Climate Change*, 235–336.

Trewartha, G., & Horn, L. (1980). Köppen's classification of climates. *An Introduction to Climate. McGraw-Hill, New York*, 397–403.

Trewartha, G. T. (1968). *An introduction to climate.*

Triantafyllopoulos, K., & Nason, G. P. (2007). A Bayesian analysis of moving average processes with time-varying parameters. *Computational Statistics & Data Analysis*, *52*(2), 1025–1046. https://doi.org/10.1016/j.csda.2007.04.001

Triantafyllou, G. N., & Tsonis, A. A. (1994). Assessing the ability of the Köppen System to delineate the general world pattern of climates. *Geophysical Research Letters*, *21*(25), 2809–2812. https://doi.org/10.1029/94GL01992

Von Mises, R. (1954). La distribution de la plus grande de n valeurs. In (Ed.), Selected Papers (Vol. II, pp. 271-294). Providence, RI. *American Mathematical Society*.

Wang, A., & Zeng, X. (2013). Development of Global Hourly 0.5° Land Surface Air Temperature Datasets. *Journal of Climate*, *26*(19), 7676–7691. https://doi.org/10.1175/JCLI-D-12-00682.1

Wang, M., & Overland, J. E. (2004). Detecting Arctic climate change using Köppen climate classification. *Climatic Change*, *67*(1), 43–62.

Wang, Y. (2005). Observed trends in extreme precipitation events in China during 1961–2001 and the associated changes in large-scale circulation. *Geophysical Research Letters*, *32*(9), L09707. https://doi.org/10.1029/2005GL022574

Wdowinski, S., Bray, R., Kirtman, B. P., & Wu, Z. (2016). Increasing flooding hazard in coastal communities due to rising sea level: Case study of Miami Beach, Florida. *Ocean & Coastal Management*, *126*, 1–8.

Weedon, G. P., Balsamo, G., Bellouin, N., Gomes, S., Best, M. J., & Viterbo, P. (2014). The WFDEI meteorological forcing data set: WATCH Forcing Data methodology applied to ERA-Interim reanalysis data. *Water Resources Research*, *50*(9), 7505–7514. https://doi.org/10.1002/2014WR015638

Westra, S., Alexander, L. V., & Zwiers, F. W. (2013). Global Increasing Trends in Annual Maximum Daily Precipitation. *Journal of Climate*, *26*(11), 3904–3918. https://doi.org/10.1175/JCLI-D-12-00502.1

Wilcock, A. A. (1968). Köppen after fifty years. *Annals of the Association of American Geographers*, *58*(1), 12–28.

Willmott, C. J., & Matsuura, K. (1995). Smart interpolation of annually averaged air temperature in the United States. *Journal of Applied Meteorology*, *34*(12), 2577–2586.

Woldemichael, A. T., Hossain, F., & Pielke, R. (2014). Impacts of Postdam Land Use/Land Cover Changes on Modification of Extreme Precipitation in Contrasting Hydroclimate and Terrain Features. *Journal of Hydrometeorology*, *15*(2), 777–800. https://doi.org/10.1175/JHM-D-13-085.1

Wong, J. S., Razavi, S., Bonsal, B. R., Wheater, H. S., & Asong, Z. E. (2017). Inter-comparison of daily precipitation products for large-scale hydro-climatic applications over Canada. *Hydrology and Earth System Sciences*, *21*(4), 2163–2185. https://doi.org/10.5194/hess-21-2163-2017

Wreford, A., & Adger, W. N. (2010). Adaptation in agriculture: Historic effects of heat waves and droughts on UK agriculture. *International Journal of Agricultural Sustainability*, *8*(4), 278–289. https://doi.org/10.3763/ijas.2010.0482

Xie, P., Chen, M., & Shi, W. (2010). CPC unified gauge-based analysis of global daily precipitation. *Preprints, 24th Conf. on Hydrology, Atlanta, GA, Amer. Meteor. Soc*, *2*.

Xie, P., Chen, M., Yang, S., Yatagai, A., Hayasaka, T., Fukushima, Y., & Liu, C. (2007). A Gauge-Based Analysis of Daily Precipitation over East Asia. *Journal of Hydrometeorology*, *8*(3), 607–626. https://doi.org/10.1175/JHM583.1

Yoshino, M. M., & Kazuko, U. (1981). Regionality of climatic change in East Asia. *Geojournal*, *5*(2), 123–132. https://doi.org/10.1007/BF02582045

Yun, K.-S., Heo, K.-Y., Chu, J.-E., Ha, K.-J., Lee, E.-J., Choi, Y., & Kitoh, A. (2012). Changes in climate classification and extreme climate indices from a high-resolution future projection in Korea. *Asia-Pacific Journal of Atmospheric Sciences*, *48*(3), 213–226. https://doi.org/10.1007/s13143-012-0022-6

Yunling, H., & Yiping, Z. (2005). Climate change from 1960 to 2000 in the Lancang River Valley, China. *Mountain Research and Development*, *25*(4), 341–348.